

NORTHWESTERN UNIVERSITY

Transport Phenomena Near The  
Normal-Metal/Superconducting Interface In Mesoscopic  
Devices

A DISSERTATION

SUBMITTED TO THE GRADUATE SCHOOL  
IN PARTIAL FULFILLMENT OF THE REQUIREMENTS

for the degree

DOCTOR OF PHILOSOPHY

Field of Physics and Astronomy

By

**Chen-Jung Chien**

EVANSTON, ILLINOIS

December 1998

© Copyright by Chen-Jung Chien 1998  
All Rights Reserved

## Abstract

Nonequilibrium superconductivity has been studied in thin film hybrid nano devices containing a superconductor (S) and a normal metal (N) through electrical charge transport measurements at temperatures below the superconducting transition temperature  $T_c$ . These samples were fabricated by two-step electron beam lithography onto silicon substrates. Measurements were performed at low temperatures using a dilution refrigerator, a  $\text{He}^3$  refrigerator, and a  $\text{He}^4$  cryostat.

It was found that a resistance higher than the normal state, the so-called resistance anomaly (RA), can be generated by applying radio-frequency (rf) radiation to a pure superconductor, creating a dynamic NS interface in the sample. The rf radiation induced resistive phase-slip centers (PSCs) at locations with weak superconductivity in the sample. The results are consistent with the charge imbalance model for electrical transport when electrons are transported across a PSC. The charge imbalance is revealed by measuring the resistance and the current-voltage characteristic of a one dimensional superconducting wire or loop near the transition temperature  $T_c$ .

In the devices containing NS interfaces, measurements at temperatures far below the transition showed an anomalous proximity effect which manifests itself in the resistance of a normal metal as a function of temperature, applied bias voltage, and external magnetic field. A detailed analysis based on recent developments in quasiclassical Green functions theory shows some discrepancies between different measurements. Comparison between the theory and the experimental results suggests further theoretical development needs to be done to understand the nature of superconducting correlations induced in the normal metal.

## Acknowledgements

I would like to thank:

My thesis advisor, Prof. Venkat Chandrasekhar, for opening the door of experimental physics for me and being so patient to finally help me through all the challenges on the way toward finish this thesis.

My colleague, Jonghwa Eom, for being so helpful in providing all invaluable experimental techniques. We have been sharing all the joy and sorrow in the Lab since 1993 and I still remember those Sunday afternoons when we were brazing all kinds of tubings to build the Lab.

Prof. C. van Haesendonck of Katholieke Universiteit Leuven in Leuven, Belgium, for all important instructions in the experiments of resistance anomaly and enjoyable basketball games.

Dr. C. Strunk of Katholieke Universiteit Leuven in Leuven, Belgium, for primarily moving the experiment on rf induced resistance anomaly. Dr. Strunk's ingenious interpretations on the experimental results have helped me understand nonequilibrium superconductivity and motivated further investigations.

Dr. B. Burk, the former post doctor of the Lab., for primarily moving the noise induced resistance anomaly experiment and sharing his knowledge in clarifying the puzzles from other experiments.

Dr. Sungkit Yip, for invaluable discussions on the theory of quasiclassical Green functions. Dr. Yip's deep insight to the physical meanings behind the theory has helped me understand the experiment on anomalous proximity effect.

Prof. J. B. Ketterson, for very useful and enjoyable discussions on superconductivity. Prof. Ketterson has enhanced my understanding of experimental physics through

theoretical analysis.

Prof. A. Garg, for instructing my thesis and all enjoyable discussions on superconductivity and quantum mechanics.

Dr. A. DiVenere, for invaluable information on lithography.

J. Aumentado, graduate student in the Lab., for all knowledge in modern computer technologies and making the Lab. alive and cheerful at 3:00 AM.

Dr. M. Black, the new post doctor in the Lab. for bringing new ideas in the experiment of proximity effect as well as information on Scottish beer.

M. Z. Lin, for invaluable knowledge of all kinds of electrical circuits.

Staff of instrument shop, for all the help in machining skills.

Staff in business and academic office, for all business and academic matters.

And finally, my family for the support in everything.

# Table of Contents

	Page
Abstract	iii
Acknowledgements	iv
List of Figures	x
List of Tables	xiv
<b>1. Introduction</b>	<b>1</b>
1.1 Resistance anomaly	2
1.2 Anomalous proximity effect	5
1.3 Overview of the thesis	8
<b>2. Theory</b>	<b>10</b>
2.1 BCS theory	10
2.1.1 Attractive interaction between two electrons	10
2.1.2 BCS ground state	12
2.1.3 Finite temperature	15
2.1.4 Bogoliubov equations	16
2.2 Nonequilibrium superconductivity	18
2.2.1 Charge imbalance	20
2.2.2 Relaxation of charge imbalance	22
2.2.3 Phase-slip center	25
2.2.4 SBT model	26
2.2.5 Resistance anomaly and excess voltage	29

2.2.6	Previous experiments in charge imbalance	32
2.3	Proximity effect	39
2.4	Quasiclassical Green functions theory	42
2.4.1	Green functions in a dirty superconductor	43
2.4.2	Boundary conditions	48
2.4.3	Parametrization of the Green functions	50
2.4.4	Some remarks on the theory	52
2.4.5	Previous experiments on the reentrance effect	56
<b>3.</b>	<b>Sample fabrication and measurement</b>	<b>61</b>
3.1	Sample fabrication	61
3.1.1	E-beam lithography	61
3.1.1.1	Substrates and cleaning	68
3.1.1.2	Oxidation of wafers	68
3.1.1.3	Resist	69
3.1.1.4	Exposure and development	71
3.1.1.5	Metallization	75
3.1.1.6	Etching	77
3.1.1.7	Lift-off	79
3.2	Measurement	81
3.2.1	Sample handling and testing	83
3.2.2	Low temperature cooling facilities	83
3.2.3	Measuring electronics	86

<b>4.</b>	<b>Resistance anomaly in mesoscopic superconducting wires</b>	<b>93</b>
4.1	Resistance anomaly in pure Al structures induced by rf signals	93
4.1.1	Sample properties and measurement setup	94
4.1.2	Resistance anomaly in $R(T)$	98
4.1.3	Resistance anomaly in $V(I)$	103
4.1.4	Resistance anomaly induced by a magnetic field	105
4.2	Noise-induced resistance anomaly in an Al line structure	111
4.2.1	Sample properties and measurements	112
4.2.2	Resistance anomaly in $R(T)$ induced by applying a noise current	112
4.2.3	Model of mixing	114
4.2.4	Resistance anomaly in $dV/dI$ induced by applying a noise current	116
4.3	Comparison of the “rf” and “noise” induced resistance anomalies	118
4.4	Resistance anomaly observed in a 1D NS wire	121
4.4.1	Resistance anomaly in $R(T)$	123
4.4.2	Negative $dV/dI$	126
4.4.3	Resistance anomaly in $R(T)$ at finite magnetic fields	129
4.5	Charge imbalance in a 1D NS hybrid loop	133
4.5.1	Negative $dV/dI$ in the NS hybrid loop	133
4.5.2	Coherence effect in the NS hybrid loop	137
4.5.3	Metastability of the differential resistance	139
<b>5.</b>	<b>Anomalous proximity effect</b>	<b>142</b>
5.1	Reentrance effect	143



5.1.1	Sample properties and measurement setup	144
5.1.2	Reentrance effect in $R(T)$	146
5.1.3	Reentrance effect in $dV/dI(V)$	158
5.1.4	Reentrance effect in $R(H)$	165
5.2	Conclusion	168
<b>6.</b>	<b>Conclusion</b>	<b>173</b>
6.1	Resistance anomaly	174
6.2	Reentrance effect	175
6.3	Further work	176
	<b>References</b>	<b>178</b>

## LIST OF FIGURES

	Page
2.2.1 Illustration of pair condensate and quasiparticle excitations in a superconductor.	19
2.2.2 Probability of pair condensate and quasiparticle excitation energy as a function of kinetic energy of the quasiparticle for equilibrium and nonequilibrium cases.	23
2.2.3 SBT model of a phase-slip center.	27
2.2.4 Two chemical potential model in the charge imbalance region.	30
2.2.5 Detection of two chemical potentials in the charge imbalance near a phase-slip center.	34
2.2.6 Negative differential resistance detected near a NS interface showing the existence of two chemical potentials due to charge imbalance.	35
2.2.7 Resistance anomalies in narrow Al wires.	37
2.3.1 Description of the proximity effect based on Ginzburg-Landau theory.	41
2.4.1 Illustration of the proximity effect in a normal metal connected to a superconducting reservoir expressed by an unit real sphere at zero electron energy.	53
2.4.2 Normalized effective diffusion coefficient $D(\epsilon, x)/D$ as a function of reduced energy $\epsilon/E_c$ for a diffusive wire connected to a normal reservoir at one end and a superconducting reservoir at the other end.	55
2.4.3 Theoretical calculation showing reentrance effect in the normalized resistance of a normal metal connected to two superconductors as a function of temperature.	57
2.4.4 Josephson effect and reentrance effect in a Cu ring connected to two superconductors.	59
3.1.1 Schematic of electron beam writer facility setup.	62
3.1.2 Illustration of the basic principle of e-beam lithography.	65
3.1.3 Thermal oxidation thickness grown on a <100> Si wafer as a function of time at different temperatures.	70
3.1.4 Example of spin curves of PMMA resist of two different molecule weights (150K/500K).	72

3.1.5	Examples of e-beam lithography patterns generated on a computer.	73
3.1.6	An example of NS device patterned by two-step e-beam lithography using the multi-level alignments and dc plasma etching techniques.	76
3.1.7	Schematic of the dc plasma etching setup. Also shown is a circuit of high power rectifier to generate dc power for the plasma.	78
3.1.8	A SEM picture showing the example of the damage caused from strong dc plasma etching.	80
3.2.1	Schematic of the measurement setup including the cooling facility and the electronics.	82
3.2.2	A PID (Proportional-Integral-Differential) circuit controller circuit.	85
3.2.3	Schematic of the circuit of a temperature controller for He <sup>3</sup> cryostat.	87
3.2.4	Electrical circuits for transport measurements.	89
4.1.1	AFM and SEM pictures of the Al samples measured in the resistance anomaly experiments.	96
4.1.2	Detail of surface structure and the height profile of sample Line#1.	97
4.1.3	Schematics of the lead configurations for applying rf or noise signals to Al samples in the resistance anomaly experiments.	99
4.1.4	R(T) curves showing resistance anomaly induced by applied rf signals of different amplitudes and frequencies.	100
4.1.5	Spatial dependence of the resistance anomaly demonstrated in R(T) measured with two voltage probes separated at various distances.	102
4.1.6	Observation of rf induced excess voltage in V(I) characteristic in an Al loop structure.	104
4.1.7	Magnetic phase boundaries $T_c(B)$ for the Al loop structure measured by the voltage leads $V_1/V_2$ and $V_1/V_3$ as shown in Fig. 4.1.3(a).	107
4.1.8	R(T) curves measured with voltage leads $V_1/V_2$ of Fig. 4.1.3(a) (across the loop) on the Al loop structure at different magnetic fields.	108
4.1.9	R(T) curves measured with voltage leads $V_1/V_3$ of Fig. 4.1.3(a) (on one side of the loop) on the Al loop structure at different magnetic fields.	109

4.1.10	Comparison of normalized height of the resistance anomaly in Fig. 4.1.8 with the difference in the critical temperatures for the segment $V_1/V_2$ and $V_1/V_3$ .	110
4.2.1	Phenomenological picture of signal mixing effects.	113
4.2.2	Resistance anomaly induced by a noise current of different amplitudes and same frequency ( $\sim 1$ KHz) in Al Line#2 sample.	115
4.2.3	Intrinsic differential resistance curves measured on Al Line#2 sample without intentionally applied noise currents.	117
4.2.4	Comparison of measured and calculated differential resistance curves in the presence of a 1 kHz noise current of rms $1 \mu\text{A}$ at various temperatures.	119
4.2.5	Comparison of measured and calculated resistance as a function of temperature in the presence of a 1 kHz noise current of rms amplitude $1 \mu\text{A}$ , with the calculated curve obtained from the zero bias differential resistance calculated in Fig. 4.2.4.	120
4.4.1	SEM picture of the 1D NS cross sample.	124
4.4.2	Normalized resistance as a function of temperature for four different measurement configurations in the 1D NS cross sample.	125
4.4.3	Differential resistance as a function of dc current at $T = 0.28$ K for the four measurement configurations in Fig. 4.4.2.	127
4.4.4	Charge imbalance relaxation length $\Lambda_{Q^*}$ and charge imbalance relaxation time $\tau_{Q^*}$ as function of magnetic field $B$ at various temperatures below $T_c$ .	131
4.4.5	Resistance as a function of temperature measured at various magnetic fields for one of the measurement configurations in Fig. 4.4.2.	132
4.5.1	Negative differential resistance as a function of dc current observed in the 1D NS loop structure at $T = 30$ mK.	134
4.5.2	Two properties of the negative differential resistance in Fig. 4.5.1. (a) metastability and (b) temperature dependence.	136
4.5.3	Amplitude and position of the $dV/dI$ dip (a) and peak (b) as a function of magnetic field for two samples.	138
4.5.4	Amplitude of the second differential resistance dip in the top curve of Fig. 4.5.1(a) as a function time.	140

5.1.1	SEM picture of sample A in the reentrance experiment and the sample schematics for sample A and B.	145
5.1.2	Normalized resistance as a function of temperature for sample A and B.	147
5.1.3	Schematic of the simulated model for sample B based on quasiclassical Green functions theory.	154
5.1.4	Simulation of the resistance as a function of temperature for sample B based on quasiclassical Green functions theory. Also shown is the simulated total resistance $R$ as a function of $T$ for different energy gaps.	156
5.1.5	Theoretical fit to the experimental data, $R(T)$ , based on the combination for quasiclassical Green functions theory and Langer-Ambegaokar (LA) theory.	159
5.1.6	Normalized differential resistance $dV/dI$ as a function of dc voltage $V$ at $T = 30$ mK for sample A and B. Also shown is the enhancement of zero bias $dV/dI$ at 225 gauss for sample A.	160
5.1.7	$R(T)$ for sample A at different magnetic flux applied perpendicular to the loop.	162
5.1.8	Comparison of the theoretical calculation of the differential resistance $dV/dI$ based on quasiclassical Green functions with the experimental data.	164
5.1.9	Magnetoresistance for sample A and B measured at various temperatures. The normalized amplitude of the Fourier transform of magnetoresistance for A and B are fit to an exponential formula, $a \exp[-b T^{1/2}]$ (solid line). Also shown is fit to the power law formula $a/T$ (dashed line).	166
5.2.1	Resistance as a function of temperature for a simple 1D NS wire.	171

## **LIST OF TABLES**

	page
3.1 Detailed procedure of the two-step e-beam lithography.	67
4.1 Material parameters for the Al loop, Line#1 and Line#2 samples.	97

# Chapter 1

## Introduction

What happens when a normal metal is connected to a superconductor ? A superconductor (S) in equilibrium contains a condensate formed by pairs of electrons of opposite momenta and spin. This Cooper pair condensate is separated from quasiparticle excitations by an energy gap. Quasiparticles injected from the normal metal (N) into the superconductor are converted to Cooper pairs over a finite distance near the NS interface, leading to a nonequilibrium region near the NS interface.

Inside the normal metal, near the NS interface, the interactions between electrons are changed due to the proximity of the superconductor. At zero temperature and energy, conductance of the normal metal is expected to double compared to its value in the absence of the superconductor. Consequently, one expects that the resistance of the normal metal decreases when it is connected to a superconductor, the so-called proximity effect.

New phenomena are expected when the dimensions of the normal metal and superconductor become comparable to the corresponding coherence lengths,  $\xi_N$  and  $\xi$ . The resistance of a superconductor connected to a normal metal can “exceed” its normal state resistance by as much as 30% at the superconducting transition, the so-called *resistance anomaly* [1-9]. The resistance of a normal wire connected to a superconductor does not always decrease as the temperature is reduced below the transition temperature  $T_c$  of the superconductor, but is predicted to regain its normal state value at  $T \rightarrow 0$ , the so-called

*reentrance effect* [10-17]. These unique phenomena have been observed in sub-micron devices thanks to modern lithography and cryogenic techniques. These results deepen our knowledge of the interaction of electrons in a metal or superconductor.

## 1.1 Resistance anomaly

The term “mesoscopic” describes systems whose dimensions are on the sub-micron scale and comparable to the characteristic lengths responsible for the physics of interest in the system. Recently, transport properties of superconductors have been studied intensively in systems where the dimensions of the samples are comparable to the coherence length of the superconductor. For a thin-film superconductor with thickness and width comparable to  $\xi$ , one of the unusual phenomena observed near the superconducting transition temperature  $T_c$  is called the resistance anomaly (RA), in which the resistance of a superconductor in the transition from its normal state to the superconducting state can exceed its normal state resistance near  $T_c$ . This RA was first observed in a pure 1D aluminum (Al) wire by Santhanam *et al.* [1]. The physics behind this unique phenomenon was attributed to the charge imbalance [18-20] resulting from the formation of a phase-slip center (PSC) in the 1D wire by the authors of Ref. 1. In this model, the formation of PSCs near  $T_c$  results in a dynamic SNS interface in the sample. Due to the presence of charge imbalance, there exist two chemical potentials inside the nonequilibrium region near the NS interfaces -- the quasiparticle chemical potential  $\mu_q$  and the pair chemical potential  $\mu_p$ . The superconducting voltage probes of the sample measure the potential difference  $\mu_p$ . Since  $\mu_q$  relaxes over a



longer length than  $\mu_p$ , the voltage probes, being placed near the intrinsic NS interface, measure a larger gradient of the potential, resulting in a measured resistance larger than the normal state resistance.

Historically, charge imbalance was first introduced by Pippard *et al.* [21] to explain the excess resistance observed in a NS interface. Later, J. Clarke [22] carried out an important experiment which explicitly revealed the concept of the model by injecting quasiparticles into a superconductor to generate a charge imbalance. The quantitative understanding of the charge imbalance model was done by M. Tinkham and J. Clarke [23] to explain the experiment in Ref. 22. Theoretically, Tinkham [24] first studied the detailed theory of the charge imbalance. Schmid and Schön [25] then used a Green function method to distinguish two different nonequilibrium modes: a transverse mode which causes charge imbalance and a longitudinal mode which causes a change of the energy gap. A two-fluid model was subsequently introduced by Pethick and Smith [26] to explain the relaxation of the charge imbalance.

Experimental interest in charge imbalance phenomena switched to pure superconducting wires when lithography techniques became more sophisticated. In the classic experiment of Dolan and Jackel [27], a nonequilibrium region was created in a narrow superconducting stripe by inducing a resistive PSC by means of a notch in the stripe. The spatial dependence of the difference between two chemical potentials was directly detected near the phase-slip center by placing several equally spaced normal and superconducting voltage probes next to the PSC. This confirmed beautifully the length scales involved in charge imbalance.

As the dimensions of the pure superconducting wire are further decreased, the role of a PSC seems to be more important in explaining the resistance anomaly phenomena. Soon after the experiment of Santhanam *et al.* [1], Vloeberghs *et al.* [2] carried out an experiment on a 1D superconducting wire containing a loop. In addition to the phenomena observed in Ref. 1, they also observed anomalous behaviors in the resistance as a function of magnetic field  $B$ , applied perpendicular to the loop. The phenomenon was referred as “anomalous Little-Parks oscillations” in contrast to the classical Little-Parks oscillations [28]. Since there was no apparent PSC in the samples of these experiments, the confirmation of a PSC in these systems is important in forming a solid theoretical basis for the resistance anomaly observed.

In a recent experiment by Park *et al.* [5], dynamic PSCs were clearly created in a 2D superconducting stripe, part of which was chemically etched and possessed a  $T_c$  and critical current  $I_c$  slightly lower than those of the unetched superconductor. The resistance anomaly was not only observed in the temperature dependence but also linked to the “excess voltage” in current-voltage ( $I$ - $V$ ) characteristics through the charge imbalance model near the PSCs. The interaction between the formations of different PSCs was also discussed. At about the same time, we [6] demonstrated that the resistance anomaly and excess voltage can be induced in a 1D pure superconducting wire by applying radio-frequency (rf) radiation. In a later experiment [9], the same group demonstrated the correlation between the resistance anomaly and PSCs by locally suppressing the order parameter in the sample, and therefore facilitating the formation of a PSC. Another discovery by B. Burk *et al.* [7, 8] was that the resistance anomaly can be induced by applying an a.c. “noise current  $I_n$ ” to the measuring current  $I_p$ . This effect is based on

mixing of  $I_n$  and  $I_p$  by the nonlinear portion of the I-V characteristic of a superconductor, resulting in an excess voltage and resistance anomaly. This mixing effect raises some concerns about the measurement techniques used in recent resistance anomaly experiments.

In Chapter 4 of this thesis, our investigation of these resistance anomalies is presented. We will first discuss our previous studies on resistance anomalies in pure mesoscopic superconductors induced by rf radiation, magnetic field, and a.c. noise current. Then we discuss recent investigations of resistance anomalies in mesoscopic devices containing NS interfaces.

## 1.2 Anomalous Proximity effect

Historically, the proximity effect was first reported by Holm and Meissner [29] who observed zero resistance in a normal-metal layer sandwiched between two superconductors. Meissner [30] and Smith *et al.* [31] then extended the thickness of the normal metal layer to micrometers. The observation of proximity effect was made even more convincingly by Clarke [32] who showed the clear existence of a critical current in a S-N-S structure with a N layer 0.55  $\mu\text{m}$  thick.

The proximity effect can be understood most simply in terms of Ginzburg-Landau theory [18, 33-35]. In this picture, the penetration of order parameter into the normal metal is responsible for the proximity effect. The order parameter, which is a spatially dependent quantity, decays from the NS boundary over a characteristic length equal to the coherence length in the normal metal. The microscopic theory of proximity effect is described in

terms of Andreev reflection [36] at the NS interface, a consequence of Bogoliubov equations [37-38], applied to the case of a spatially varying energy gap  $\Delta(x)$ , with a discontinuity at the NS boundary. Due to this discontinuity an electron-like quasiparticle having an energy  $E < \Delta$  in the normal metal cannot propagate into the superconductor as a free quasiparticle state, but is reflected as a hole, with the concurrent production of a Cooper pair in the superconductor. Andreev reflection leads to an enhancement of the normal metal conductivity which was observed as an excess current in some experiments on superconducting microbridges [18, 34].

As systems are extended from thin-film junctions to one dimensional wires, quantum interference effects stemming from the proximity effect become explicit. An anomalous proximity effect has been observed in 1D diffusive metals connected to superconductors by one or two NS interfaces [39]. The general properties of these anomalous proximity effects include: (i) A supercurrent can be sustained in a 1D diffusive wire a few microns long connected to two superconductors [40]; (ii) The transport properties of the normal metal are sensitive to the phase of a superconductor and show periodic oscillations as a function of the phase difference between two NS interfaces [41-44]. The amplitudes of these oscillations are larger by several orders of magnitude than the usual normal metal quantum interference effects observed in diffusive metals [45] when the superconductor is absent. (iii) At temperatures well below  $T_c$ , a normal metal connected to N and S reservoirs shows a reentrant behavior distinguished by an *increase* of the normal-metal resistance [10-14]. In order to explain these anomalous proximity effects, an alternative theoretical approach based on quasiclassical Green functions theory has been studied intensively in NS systems [46-53]. Instead of solving Schrödinger-like equations

and then calculating the expectation values of the physical quantities of interest, this theory used a set of equations of impurity-averaged quasiclassical Green functions obtained by Usadel [54] to calculate various physical quantities. This approach has been successful in explaining quantitatively most recently observed experimental results on proximity effect in diffusive metals where the energy involved is much smaller than the superconducting energy gap.

Recent experimental interest on proximity effect in 1D diffusive metals started with a number of experiments by Petrashov *et al.* [55]. The strange phenomena observed include: an *increase* in the resistance of a diffusive metal adjacent to one or two superconductors at the onset of superconductivity, and an enhanced Aharonov-Bohm (AB) effect in normal-metal rings connected to superconducting stripes as addressed in (ii) and (iii) of the properties of the anomalous proximity effect. Early experiments [42-44] after Petrashov *et al.* in the diffusive proximity regime concentrated on phase sensitive properties, a result of Andreev reflection. The system of interest is usually referred to as an “Andreev interferometer.” These experiments used different methods to modulate the phase difference between two NS interfaces in the interferometer including: a dc current passing through a series of Josephson junctions [42], a magnetic field threading a normal-metal/superconducting loop [43], and a dc current passing through a long superconducting loop connected to the normal metal at two NS interfaces [44]. The energy-dependence of Andreev reflection in the proximity affected diffusive metals was shown in two later experiments by Courtois *et al.* [12] and Guéron *et al.* [86] respectively. The former group distinguished the long-range coherence property of the proximity effect from other quantum coherence effects, and the latter group observed a reduced density of states in the proximity affected normal-metal wire.

The success of the Usadel equation [54] in explaining the experimental results of Ref.[86] motivated further investigation of the proximity effect in 1D diffusive wires based on quasiclassical Green functions theory. The long-range coherence of the proximity effect was also realized in the experiment of Antonov *et al.* [56], where it was differentiated from other quantum coherence effects through several different geometries of NS hybrid loops. Supercurrent sustained in a diffusive metal between two superconductors was further investigated by Antonov *et al.* [57]. The reentrance effect was demonstrated by Charlat *et al.* [13] and Petrashov *et al.* [14]. While all these experimental results are qualitatively well explained by the theory of quasiclassical Green functions, detailed quantitative comparisons between the theory and experiments is not easy, probably due to an intrinsic difficulty in studying the energy dependence of this effect in the diffusive system. In Chapter 5, we will carry out a detailed comparison of the theoretical predictions with the reentrance effect observed in three different transport measurements in a diffusive system. The comparison shows quantitative discrepancies between the theory and the experimental results. By introducing the nonequilibrium superconductivity effect into our device, we show that the theoretical calculation can explain some of the data, while it cannot explain the rest of the data, implying an intrinsic difference between different transport properties.

### 1.3 Overview of the thesis

The rest of this thesis is organized as follows. Chapter two gives a brief overview of the Bardeen, Cooper, Schrieffer theory of superconductivity, followed by detailed discussions of charge imbalance and quasiclassical Green functions theories, emphasizing the theory relevant to our experiments. Chapter three is comprised of two parts: details of sample

fabrication and techniques of transport measurement on mesoscopic devices. The results of our experiments in the resistance anomaly induced by radio-frequency signals close to  $T_c$ , along with nonequilibrium superconductivity effects observed in 1D NS systems, are presented in Chapter four. Chapter five deals with the anomalous proximity effect (reentrance effect) at temperatures far below  $T_c$ . A detailed simulation of the experimental results based on quasiclassical Green functions theory is compared with the data. Chapter 6 concludes this thesis with a summary of our results and some comments on some possible future directions in this field.

## Chapter 2

### Theory

In this chapter I will briefly describe the theory involving nonequilibrium superconductivity and the proximity effect. The chapter starts with a review of the Bardeen-Cooper-Schrieffer (BCS) theory of superconductivity [58] and Bogoliubov equations [37] with a spatially varying order parameter. Two kinds of nonequilibrium modes in superconductivity are then explained at temperatures near the superconducting transition temperature  $T_c$ , i.e., the charge mode and the energy mode, followed by a more detailed explanation of the charge imbalance model and phase-slip centers. Finally, the quasiclassical Green functions theory is introduced in order to explain the anomalous proximity effect in a normal metal connected to a superconductor at temperatures far below  $T_c$ , with the emphasis on some important concepts and their applications to the transport problem in diffusive metals.

#### 2.1 BCS theory

##### 2.1.1 Attractive interaction between two electrons

The basic idea of the microscopic theory of superconductivity developed by BCS [58] is that a weak attraction can bind pairs of electrons into a bound state no matter how weak the interaction [59]. The system then consists of a bound pair and a Fermi sea of electrons obeying the Pauli exclusion principle occupying all states with wavevector  $k < k_F$ , where  $k_F$



is the wave vector at the Fermi level. The existence of this bound state implies a gap in the energy spectrum, which is required to explain many phenomena.

The microscopic origin of the attractive interaction was first introduced by Fröhlich [60] and Bardeen *et al* [61]. They pointed out that the electron-phonon interaction is able to couple two electrons together in such a way that they behave as if there is a direct interaction between them. In this picture, one electron emits a phonon which is immediately absorbed by another. Fröhlich showed that in certain circumstances this process could result in a weak attraction between the electrons which might produce an energy gap of the right order of magnitude responsible for superconductivity.

Consider the bare Coulomb interaction  $V(r) = e^2/r$ , where  $r$  is the distance between the two electrons. Taking into account the dielectric function  $\epsilon$  of the medium, the matrix elements of the interaction potential can be written [18]:

$$V(\mathbf{q}) = 4\pi e^2 / (\mathbf{q}^2 + k_s^2), \quad (2.1.1)$$

where  $\mathbf{q} = \mathbf{k} - \mathbf{k}'$  and  $\hbar\omega$  are the wave vector and energy of the phonon respectively.  $1/k_s \sim 1\text{\AA}$  is the Thomas-Fermi screening length of the conduction electrons. The electronic screening eliminates the divergence at  $\mathbf{q}=0$ . This  $V(\mathbf{q})$  characterizes the strength of the potential for scattering a pair of electrons with momenta  $(\mathbf{k}', -\mathbf{k}')$  to momenta  $(\mathbf{k}, -\mathbf{k})$ . However,  $V(\mathbf{q})$  thus obtained is positive and consequently, no superconductivity would result.

To introduce the negative terms, Pines [62] created a “jellium” model, in which the solid is approximated by a fluid of electrons and point ions. The essence of this model is that the first electron polarizes the medium by attracting positive ions; these positive ions in turn attract the second electron, giving an effective attractive interaction between the electrons. If this attraction is stronger than the repulsive Coulomb interaction, superconductivity then results due to a net attractive interaction. As shown by de Gennes [35], this model leads to the following formula:

$$V(\mathbf{q}) = [ 4\pi e^2 / (q^2 + k_s^2) ] [ 1 + \omega_q^2 / (\omega^2 - \omega_q^2) ] \quad (2.1.2)$$

The first term describes the Coulomb repulsion and the second term describes the interaction between the electron and the phonon. As we can see in Eq. (2.1.2),  $V(\mathbf{q})$  is always negative for  $\omega < \omega_q$  regardless of the material parameters. Although the formula does not take into account the complexity of the interactions, it gives a reasonable order of magnitude for the attractive interaction and provides a right direction for the exploration of the origin of superconductivity.

### 2.1.2 BCS ground state

The concept of a pair interaction strongly suggests the ground state of a superconductor is entirely composed of electron pairs, each pair containing electrons of opposite momentum and spin in order to minimize the total free energy. This is called the superconducting condensate and it is described by the ground state introduced by BCS:

$$\Psi_{\text{BCS}} = \prod_{\mathbf{k}} (\mu_{\mathbf{k}} + v_{\mathbf{k}} \hat{c}_{\mathbf{k}\uparrow}^{\dagger} \hat{c}_{-\mathbf{k}\downarrow}^{\dagger}) |\phi_0\rangle \quad (2.1.3)$$

where  $\mu_{\mathbf{k}}$  and  $v_{\mathbf{k}}$  are coherence factors and  $|\phi_0\rangle$  is the vacuum state with no particle.  $\mu_{\mathbf{k}}$  and  $v_{\mathbf{k}}$  obey the normalization condition:

$$|\mu_{\mathbf{k}}|^2 + |v_{\mathbf{k}}|^2 = 1. \quad (2.1.4)$$

Eq. 2.1.3 indicates that the probability of the pair of state  $(\mathbf{k}\uparrow, -\mathbf{k}\downarrow)$  being occupied and unoccupied is  $|v_{\mathbf{k}}|^2$  and  $|\mu_{\mathbf{k}}|^2$  respectively. The procedure used to obtain the ground state energy is the variational method. The goal is to minimize the expectation value of the so-called *reduced Hamiltonian* subject to the constraint of the normalization condition. The *reduced Hamiltonian* has the following form [18, 35, 63]:

$$\hat{H}_R = \sum_{\mathbf{k}, \sigma} \epsilon_{\mathbf{k}} \hat{c}_{\mathbf{k}\sigma}^{\dagger} \hat{c}_{\mathbf{k}\sigma} + \sum_{\mathbf{k}, \mathbf{k}'} V_{\mathbf{k}, \mathbf{k}'} \hat{c}_{\mathbf{k}\uparrow}^{\dagger} \hat{c}_{-\mathbf{k}'\downarrow}^{\dagger} \hat{c}_{-\mathbf{k}\downarrow} \hat{c}_{\mathbf{k}'\uparrow} \quad (2.1.5)$$

Note here  $\epsilon_{\mathbf{k}}$  denotes the excitation energy relative to the Fermi level, i.e.,  $\epsilon_{\mathbf{k}} = \hbar^2 \mathbf{k}^2 / 2 - E_F$ .

The expectation value  $\langle \hat{H}_R \rangle$  is then a function of  $\mu_{\mathbf{k}}$  and  $v_{\mathbf{k}}$ . Using Eq.(2.1.4) and introducing an energy gap  $\Delta_{\mathbf{k}}$  for each state  $\mathbf{k}$ , one obtains an equation for the superconducting energy gap which has to be solved self-consistently:

$$\Delta_{\mathbf{k}} = - \sum_{\mathbf{k}'} V_{\mathbf{k}\mathbf{k}'} \frac{\Delta_{\mathbf{k}'}}{2\sqrt{\epsilon_{\mathbf{k}'}^2 + \Delta_{\mathbf{k}'}^2}}. \quad (2.1.6)$$

The BCS coherence factors can be expressed in terms of  $\Delta_{\mathbf{k}}$  and  $\epsilon_{\mathbf{k}}$ :

$$v_{\mathbf{k}}^2 = \frac{1}{2} \left( 1 - \frac{\epsilon_{\mathbf{k}}}{E_{\mathbf{k}}} \right) \quad (2.1.7a)$$

$$\mu_{\mathbf{k}}^2 = \frac{1}{2} \left( 1 + \frac{\epsilon_{\mathbf{k}}}{E_{\mathbf{k}}} \right) \quad (2.1.7b)$$

where  $E_{\mathbf{k}} = (\Delta_{\mathbf{k}}^2 + \epsilon_{\mathbf{k}}^2)^{1/2}$  is the quasiparticle excitation energy at state  $\mathbf{k}$  or  $-\mathbf{k}$ . Using the

Cooper model potential:

$$V_{\mathbf{k}\mathbf{k}'} = \begin{cases} -V & |\epsilon_{\mathbf{k}}| \text{ and } |\epsilon_{\mathbf{k}'}| \leq \hbar \omega_D \\ 0 & |\epsilon_{\mathbf{k}}| \geq \hbar \omega_D \text{ or } |\epsilon_{\mathbf{k}'}| \geq \hbar \omega_D \end{cases}. \quad (2.1.8)$$

one can solve the gap equation (2.1.6) in its integral form combined with Eq.(2.1.8) and obtain:

$$\Delta \approx 2 \hbar \omega_D e^{-\frac{1}{N(0)V}}. \quad (2.1.9)$$

Here  $\hbar\omega_D$  is the cut-off energy of the integration,  $\omega_D$  being the Debye frequency and  $N(0)$  the density of states at the Fermi level. We have assumed the energy gap is a constant  $\Delta$  for all states, which has proved to be a reasonable assumption to explain most of the experimental results [18, 35, 63]. Once the energy gap is obtained, the condensation energy can be evaluated using the coherence factors and yields:

$$E_s = \frac{1}{2} N(0) \Delta^2. \quad (2.1.10)$$

### 2.1.3 Finite temperature

At finite temperature the probability of a quasi-particle that is excited out of the condensate is given by the Fermi distribution function [18, 35, 63]:

$$f(E_k) = \frac{1}{e^{\beta E_k} + 1} \quad (2.1.11)$$

where  $\beta = 1/k_B T$ . The gap equation then becomes:

$$\frac{1}{V} = \frac{1}{2} \sum_k \frac{\tanh(\beta E_k / 2)}{E_k} \quad (2.1.12)$$

The temperature dependence of the energy gap  $\Delta(T)$  can be obtained by solving Eq. 2.1.12 self-consistently. (The gap appears in the energy  $E_k$ .) At the critical temperature  $T_c$ , the gap equation possesses no nontrivial solution and the system becomes normal, while at

zero temperature the system is completely superconducting. This implies there exists an equation connecting  $T_c$  with the zero-temperature energy gap  $\Delta(0)$ . To obtain this equation, one can solve Eq. 2.1.12 by replacing  $T$  with  $T_c$ . It was found the gap at zero temperature  $\Delta(0)$  is related to  $T_c$  through a universal constant [18, 35, 63]:

$$\Delta(0) = 1.76 k_B T_c \quad (2.1.13)$$

#### 2.1.4 Bogoliubov Equations

In the case of an inhomogeneous superconductor, the order parameter varies in space. The coherence factors used to obtained the ground state properties must then also be space dependent. The Bogoliubov transformations [18, 35, 63] generalize the BCS factors in the spatially dependent case which is commonly encountered in superconductors when the superconductor is connected to a normal metal or impurity scattering is involved. The Bogoliubov transformations read [35]:

$$\Psi(\mathbf{r}) = \sum_{\mathbf{n}} [\gamma_{\mathbf{n}} \mu_{\mathbf{n}}(\mathbf{r}) - \gamma_{\mathbf{n}}^* v_{\mathbf{n}}^*(\mathbf{r})] \quad (2.1.14a)$$

$$\Psi(\mathbf{r}) = \sum_{\mathbf{n}} [\gamma_{\mathbf{n}} \mu_{\mathbf{n}}(\mathbf{r}) - \gamma_{\mathbf{n}}^* v_{\mathbf{n}}^*(\mathbf{r})] \quad (2.1.14b)$$

where  $\Psi(\mathbf{r})$  is now an annihilation operator for a position eigenfunction instead of the momentum eigenfunction dealt with in the BCS case.  $\gamma$  and  $\gamma^*$  are new operators still obeying the anticommutation rules:

$$\gamma_{n\alpha}^* \gamma_{m\beta} + \gamma_{m\beta}^* \gamma_{n\alpha} = \delta_{mn} \delta_{\alpha\beta} \quad (2.1.15a)$$

$$\gamma_{n\alpha} \gamma_{m\beta} + \gamma_{m\beta} \gamma_{n\alpha} = 0 \quad (2.1.15b)$$

Similar to the treatment in BCS, the position dependent coherence factors here are determined by diagonalizing the effective Hamiltonian  $H_{\text{eff}}$ . Taking the external field and the variation of the order parameter into account [35]:

$$\begin{aligned} H_{\text{eff}} = \int \{ \sum_{\sigma} \Psi^*(\mathbf{r}, \sigma) [ \frac{1}{2m} ( \frac{\hbar}{i} \nabla - \frac{e\mathbf{A}}{c} )^2 + U(\mathbf{r}) - \mu ] \Psi(\mathbf{r}, \sigma) \\ + \Delta(\mathbf{r}) \Psi^*(\mathbf{r} \uparrow) \Psi^*(\mathbf{r} \downarrow) + \Delta^*(\mathbf{r}) \Psi(\mathbf{r} \uparrow) \Psi(\mathbf{r} \downarrow) \} d\mathbf{r} \end{aligned} \quad (2.1.16)$$

where  $\Delta(\mathbf{r}) = V \langle \Psi(\mathbf{r} \uparrow) \Psi(\mathbf{r} \downarrow) \rangle$ . The coherence factors  $\mu_{\mathbf{k}}(\mathbf{r})$  and  $v_{\mathbf{k}}(\mathbf{r})$  are found to obey the coupled Bogoliubov equations [35]:

$$\begin{pmatrix} H_0 & \Delta(\mathbf{r}) \\ \Delta^*(\mathbf{r}) & -H_0^* \end{pmatrix} \begin{pmatrix} \mu(\mathbf{r}) \\ v(\mathbf{r}) \end{pmatrix} = E \begin{pmatrix} \mu(\mathbf{r}) \\ v(\mathbf{r}) \end{pmatrix} \quad (2.1.17)$$

$$\text{with } H_0 = \frac{1}{2m} ( \frac{\hbar}{i} \nabla - \frac{e\mathbf{A}}{c} )^2 + U(\mathbf{r}) - \mu. \quad (2.1.18)$$

## 2.2 Nonequilibrium superconductivity

Before turning to the nonequilibrium case, let us review some important results at equilibrium from BCS theory. In equilibrium, the ground state of a superconductor is formed from Cooper pairs according to BCS theory. The quasiparticle excitations above the ground state have energies equal to  $E_k = (\Delta^2 + \epsilon_k^2)^{1/2}$ , where  $\epsilon_k = \hbar^2 k^2/2 - E_F$ .  $\epsilon_k > 0$  for  $k > k_F$  and  $\epsilon_k < 0$  for  $k < k_F$ . The energy gap  $\Delta$  and total electronic charge  $Q$  can be expressed as [18, 19, 64]:

$$\frac{2}{V} = \sum_k \frac{1 - 2f_k}{E_k} = \sum_k \frac{1 - 2f_k}{(\Delta^2 + \epsilon_k^2)^{1/2}} \quad (2.2.1)$$

$$Q = -\frac{2e}{V} \sum_k [\mu_k^2 f_k + v_k^2 (1 - f_{-k})] \quad (2.2.2)$$

where  $f_k$  is equal to the Fermi function  $f_0 = (1 + e^{\beta E_k})^{-1}$ . As illustrated in Fig. 2.2.1(a) the pair interaction only happens within a very small energy range  $\sim 2\Delta$  near the Fermi energy. The important nature of a quasiparticle excitation is that it continuously changes from “electron-like” to “hole-like” as the excitation goes from outside to inside the Fermi surface. Fig. 2.2.1(b) shows the probability of occupation of the condensate as a function of the quasiparticle energy  $\epsilon_k$ . Deep inside the Fermi surface the metal is filled with pairs of electrons with opposite momenta and spins. Near the Fermi surface the probability quickly



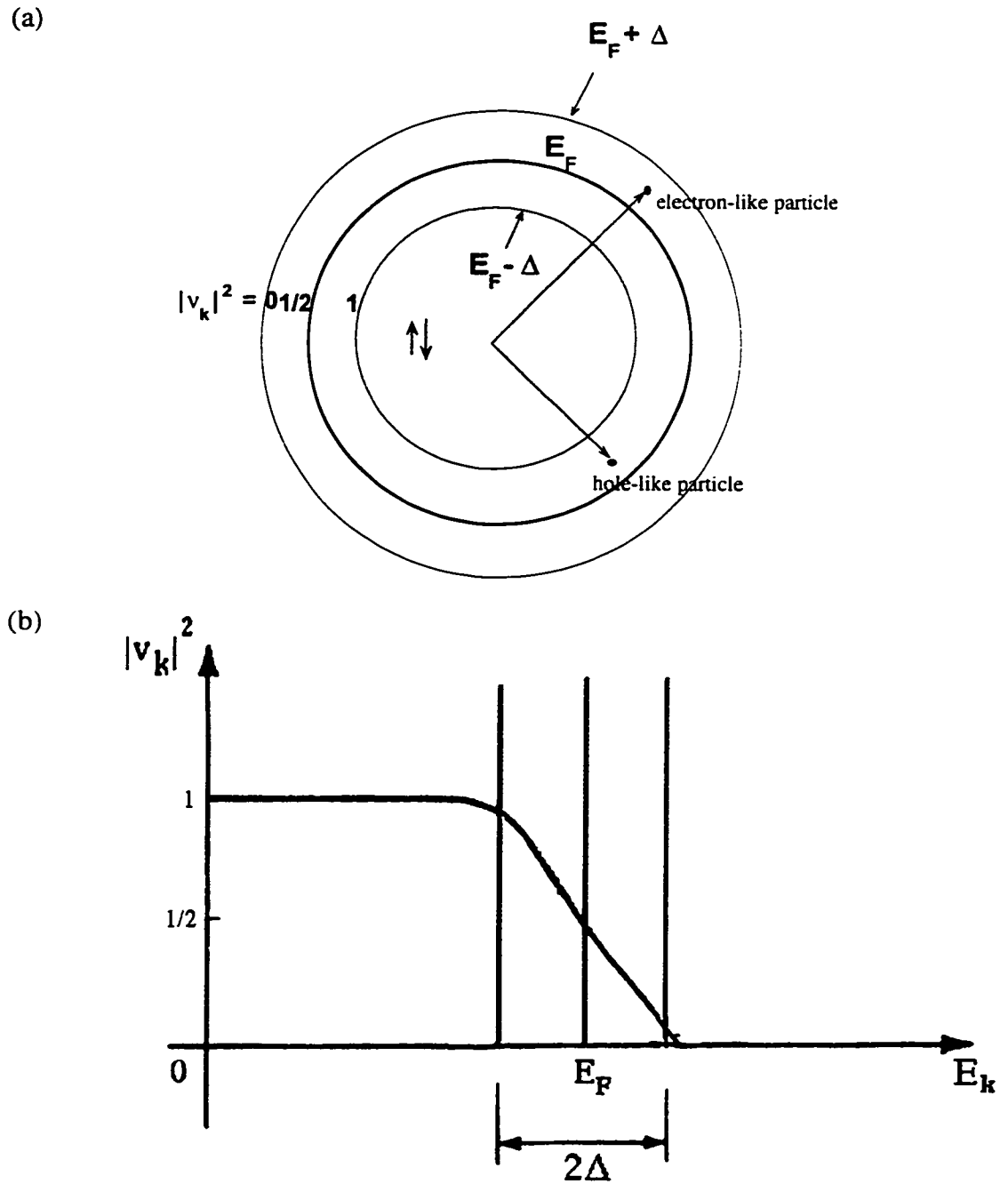


Fig. 2.2.1 Illustration of the pair condensate and quasiparticle excitations in a superconductor. (a) Phenomenological picture. (b) Probability of a state  $\mathbf{k}$  is occupied by a pair of electrons with opposite momentum and spin. (Adapted from R. Tidecks, Ref. [20]).

drops to zero over a small energy range  $\sim 2\Delta$ . At  $\epsilon_{\mathbf{k}} = E_F$ , the probability is  $|v_{\mathbf{k}}|^2 = 1/2$ , where  $v_{\mathbf{k}}$  is the usual BCS coherence factor.

Under nonequilibrium conditions, the probability of occupation of each state  $f_{\mathbf{k}}(E_{\mathbf{k}})$  is no longer equal to  $f_0(E_{\mathbf{k}})$  and causes an imbalance in both charge and energy. The difference between  $f_{\mathbf{k}}$  and  $f_0$  can be split into two components, one which is even in  $E_{\mathbf{k}}$  about the Fermi energy, and one which is odd. The even (or energy) mode can be induced by neutral perturbations such as phonons and photons in which the perturbation produces an equal change of quasiparticles in both electron-like and hole-like branches. In consequence, it causes an effective change in the energy gap. The odd (or charge) mode can be induced by injecting quasiparticles into the superconductor. As a result, an equal amount of charge has to be removed from the condensate to maintain overall charge neutrality, resulting in a difference between the chemical potential  $\mu_p$  of the pairs and the chemical potential  $\mu_q$  of the quasiparticles in the superconductor. One should note that quasiparticle injection into a superconductor also generates an even mode imbalance.

Since the experiments done in this thesis involves only charge imbalance I describe in the following sections some important concepts and results of charge imbalance.

### 2.2.1 Charge Imbalance

Charge imbalance is mostly observed when the dominant electron-like quasiparticles are injected into the superconductor. Eq. 2.2.2 can be rewritten as [19, 20]:

$$Q = Q_s + Q^* \quad (2.2.3)$$

where

$$Q_s = \frac{2}{V} \sum_{\mathbf{k}} v_{\mathbf{k}}^2, \quad (2.2.4)$$

$$Q^* = \frac{2}{V} \sum_{\mathbf{k}} (\mu_{\mathbf{k}}^2 - v_{\mathbf{k}}^2) f_{\mathbf{k}} = \frac{2}{V} \sum_{\mathbf{k}} q_{\mathbf{k}} f_{\mathbf{k}}, \quad (2.2.5)$$

The first term  $Q_s$  is the contribution from pairs while the second term  $Q^*$  is from quasiparticles. We define an *effective charge* in units of  $(-e)$ :

$$q_{\mathbf{k}} = \mu_{\mathbf{k}}^2 - v_{\mathbf{k}}^2 = \xi_{\mathbf{k}} / E_{\mathbf{k}}. \quad (2.2.6)$$

We can see immediately that  $q_{\mathbf{k}} = +1$  (electron-like) for  $\xi_{\mathbf{k}} \gg \Delta$  and  $q_{\mathbf{k}} = -1$  (hole-like) for  $\xi_{\mathbf{k}} \ll \Delta$ . In thermal equilibrium,  $Q^* = 0$  when  $f_{\mathbf{k}} = f_0$  since  $q_{\mathbf{k}}$  and  $f_0$  are odd and even functions of  $\xi_{\mathbf{k}}$  about  $E_F$  respectively. Therefore the chemical potential of the pair condensate  $\mu_p$  is equal to  $E_F$  even at finite temperature (even mode). Let us now turn to the nonequilibrium case. If one adds quasiparticles to the electron-like branch, the condensate has to remove an equal amount of charge to maintain overall charge neutrality.  $\mu_p$  is then lowered by an amount  $\delta\mu$ , so that the bottom of the excitation spectrum is shifted to the left (Fig. 2.2.2). Consequently,  $q_{\mathbf{k}}$  is no longer an odd function about  $E_F$ , and  $Q^* \neq 0$ . The

injection of excitations into the electron branch drives both pair and quasiparticle chemical potentials  $\mu_p$  and  $\mu_q$  away from the equilibrium Fermi surface  $E_F$  as shown in Fig. 2.2.2.

### 2.2.2 Relaxation of charge imbalance

Restoration of equilibrium for a charge or energy imbalance requires a decay or relaxation of the nonequilibrium quasiparticle distributions by microscopic mechanisms taking place in the superconductor. There are three main processes that contribute to the relaxation of the charge imbalance on the electron or hole branch of the quasiparticle spectrum [18-20]. The first is inelastic scattering by phonons. This includes: scattering to lower energy and lower charge on the same branch or to lower energy and lower charge with opposite sign on the other branch. The second is recombination with a quasiparticle of the same or the other branch. The third is elastic scattering from non-magnetic impurities in a superconductor with an anisotropic gap.

Taking these three processes into account, Schmid and Schön [25] derived an appropriate relaxation time for dirty superconductors. They obtained a charge imbalance relaxation time close to  $T_c$  of the form:

$$\tau_Q = \frac{4k_B T_c}{\pi\Delta} \sqrt{(\tau_E/2\Gamma)(1 + \hbar^2 \Gamma / \Delta^2 \tau_E)}, \quad (2.2.7)$$

$$\Gamma = \frac{1}{\tau_s} + \frac{1}{2\tau_E} + \frac{D}{2} \left( \frac{4m^2 v_s^2}{\hbar^2} - \frac{1}{\Delta} \frac{\partial^2 \Delta}{\partial \mathbf{r}^2} \right) \quad (2.2.8)$$

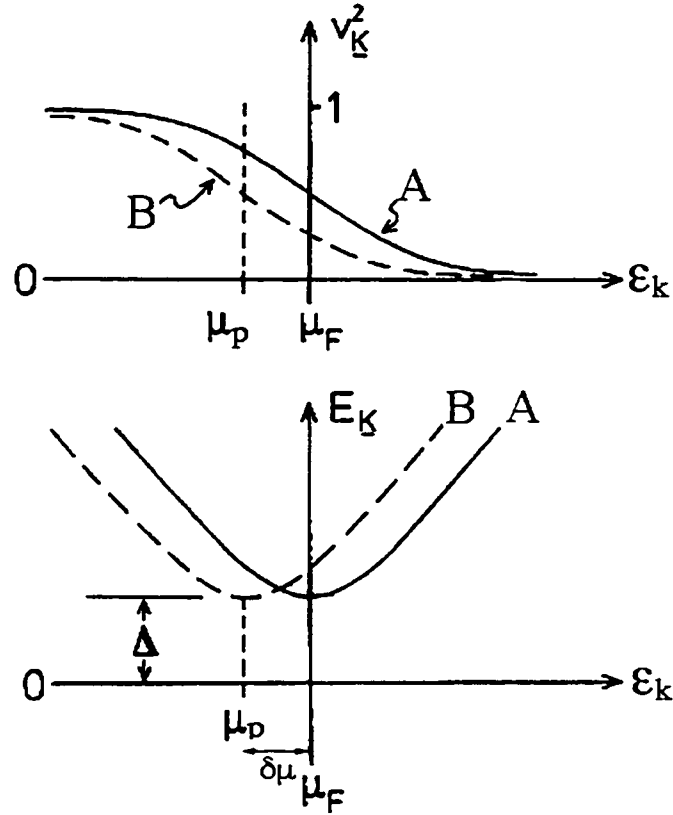


Fig. 2.2.2 Probability of the pair condensate  $v_k^2$  and excitation energy  $E_k$  as a function of  $\epsilon_k = (E_k^2 - \Delta^2)^{1/2}$  for the equilibrium case (curve A) and the nonequilibrium case (curve B).  $\mu_p$  is the pair chemical potential. Curve B corresponds to an injection of electron-like quasiparticles into the condensate. (Adapted from R. Tidecks, Ref. [20]).

Here  $\tau_s$  is the elastic spin-flip scattering time,  $D = \ell v_F / 3$  is the diffusion constant,  $v_s$  is the superfluid velocity and  $\tau_E$  is the inelastic scattering time. The first term in Eq. 2.2.8 describes the effect of spin-flip scattering, the second the effect of inelastic scattering, the third pair-breaking by the supercurrent, and the last term the effect of spatial variations of the gap parameter  $\Delta$ . In the limit  $\hbar^2 \Gamma / \Delta^2 \tau_E \ll 1$ , it follows that:

$$\tau_{Q^*} = \frac{4k_B T_{c0}}{\pi \Delta} \sqrt{\tau_E / 2\Gamma} \quad (2.2.9)$$

In the case of relaxation due only to inelastic scattering with phonons,  $\Gamma = 1/2\tau_E$ , and consequently:

$$\tau_{Q^*} = \frac{4k_B T_{c0}}{\pi \Delta} \tau_E \quad (2.2.10)$$

The charge imbalance will diffuse away from the injection point due to relaxation. In one dimension (1D) this causes a decay of  $Q^*$  in space as  $e^{-x/\Lambda_{Q^*}}$ , where

$$\Lambda_{Q^*} = \sqrt{D\tau_{Q^*}}. \quad (2.2.11)$$

$\Lambda_{Q^*}$  is called the charge imbalance relaxation length, and is typically a few microns to a few tenths of microns in Al [27, 70].

### 2.2.3 Phase-slip centers

As discussed in great detail in many articles [18-20], the time evolution of the phase of the superconducting order parameter is spatially dependent if an electrostatic potential  $V_{12}$  exists between two positions  $\mathbf{r}_1$  and  $\mathbf{r}_2$ . The time dependence of the phase difference  $\phi_{12}$  measured between  $\mathbf{r}_1$  and  $\mathbf{r}_2$  is given by the Josephson relation  $\dot{\phi} = 2eV_{12}(t)/\hbar$ , which leads on integration to:

$$\phi_{12}(t) - \phi_{12}(0) = \frac{2e}{\hbar} \int_0^t V(t') dt' \quad (2.2.12)$$

If the time-averaged voltage is nonzero, the phase difference will increase as a function of time. This leads to an increase of the magnitude of the supercurrent density which is given by  $\mathbf{J}_s = -(2e/m^*)|\psi(\mathbf{r})|^2\hbar\nabla\phi(\mathbf{r})$ . Consequently, the order parameter decreases and the superconductor will eventually enter the normal state. To maintain superconductivity, the phase difference has to be reduced by an equivalent amount. For this reason, a “phase-slip” event is assumed to occur in the superconductor, each phase-slip event reducing the phase difference by  $2\pi$ . In steady state, the average of the phase difference generated by the voltage is compensated by phase-slip processes. The frequency of the phase-slip process is just the Josephson frequency:

$$\omega_J = \frac{2e}{\hbar} \langle V(t) \rangle \quad (2.2.13)$$

There has been much effort devoted to explaining the model of a phase-slip center. The Rieger-Scalapino-Mercereau (RSM) model [65] focuses on the dynamics of the superconducting order parameter. The Skocpol-Beasley-Tinkham (SBT) model [66] adds nonequilibrium quasiparticles and charge imbalance relaxation during diffusion of the quasiparticles. The Kadin-Smith-Skocpol (KSS) model [67] then develops the dynamics of charge imbalance near a phase-slip center. For the purpose of interpreting our experimental data we briefly describe the essence of the SBT model with emphasis on the charge imbalance aspect.

#### 2.2.4 Skocpol-Beasley-Tinkham (SBT) Model

Using the SBT model one can obtain the connection between the voltage across a phase-slip center and the charge imbalance length  $\Lambda_Q$ . The main ingredient of the theory is shown in Fig. 2.2.3 for the 1D case [18-20]. A phase-slip center contains a core of length  $\sim 2\xi$ , in which the oscillation of the order parameter occurs, where  $\xi$  is the Ginzberg-Landau coherence length. On either side of the core a charge imbalance region is created and diffuses over a distance  $\Lambda_Q$  before  $\mu_q$  relaxes to  $\mu_p$ . The current inside a PSC decomposes to a nonzero time-averaged dc supercurrent  $\langle I_s \rangle = I_c/2$  and a normal current  $I_n = I - \langle I_s \rangle$ , where  $I$  is the applied current. The normal current  $I_n$  determines the shape of quasiparticle chemical potential  $\mu_q$  through the connection between the slope of  $\mu_q$  and  $I_n$ ,  $d\mu_q/dx \sim eI_n\rho/A$ , where  $\rho$  is the resistivity of the normal wire and  $A$  is the cross-sectional area. Since the pair chemical potential  $\mu_p$  is almost constant throughout the whole charge



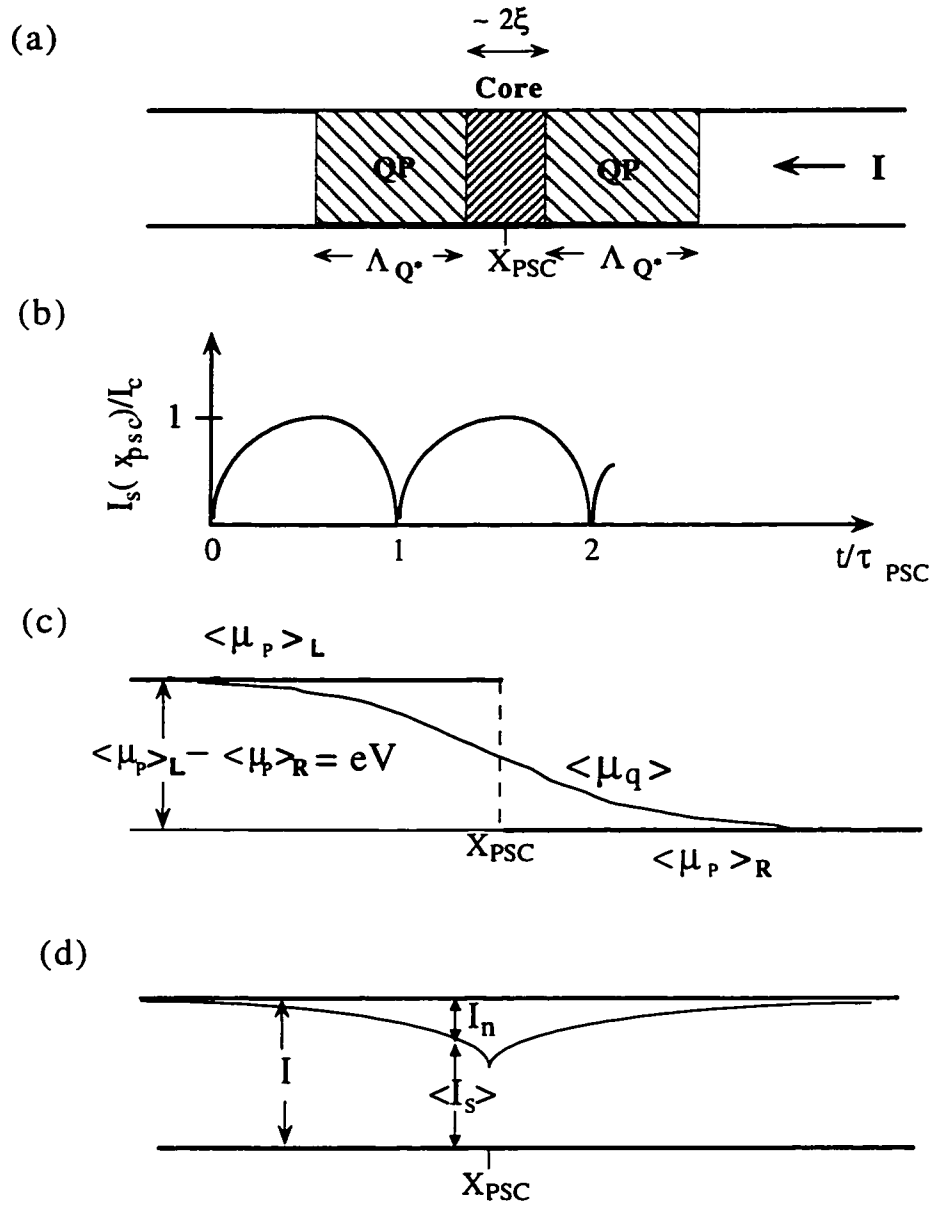


Fig. 2.2.3 SBT model of a phase-slip center. (Adapted from R. Tidecks (Ref.[20]) and M. Tinkham (Ref. [18])).

imbalance region, one can also write  $d(\mu_q - \mu_p)/dx \sim eI_n \rho/A$ . Integrating through the whole charge imbalance region, one obtains the voltage difference across a PSC:

$$V = 2\Lambda_Q \cdot \rho (I - I_c/2)/A. \quad (2.2.14)$$

Using a model based on PSCs induced by thermal fluctuations near  $T_c$ , Langer and Ambegaokar [68] (LA) successfully described the phase transition near  $T_c$ . In their picture, a PSC moves the system from one local minimum of the Ginzburg-Landau (GL) free energy to another which is separated from the first by a change of  $2\pi$  in the phase of the order parameter [18]. They were able to calculate the free energy barrier that the system has to overcome in order to generate a phase-slip event. Later, McCumber and Halperin [69] used time-dependent GL theory to obtain a temperature-dependent “attempt frequency” which describes the mean net phase-slip rate. The model of statistical thermal activation of the phase-slip centers according to Langer-Ambegaokar and McCumber-Halperin (LA-MH) and the model of current enforced and discontinuous nucleation of PSCs according to Skocpol, Beasley and Tinkham (SBT) [66] work in different temperature regimes. The temperature range where the thermal activation of PSCs is important is restricted to a very narrow interval near  $T_c$  with a width of about 1 mK, while the current enforced nucleation of PSCs extends to about 10 mK below  $T_c$ . Consequently, the thermal activation effect is best observed in high purity samples, i.e. whiskers, where the resistive transition is not additionally broadened by sample inhomogeneities which typically occur in thin films. The parameter controlling the width of the relevant temperature interval is the height of the

energy barrier for a phase-slip event, which is proportional to the sample cross section as is implied in Eq. 2.2.14.

### 2.2.5 Resistance anomaly and excess voltage

Charge imbalance, either near a NS interface or a PSC, is usually manifested in charge transport by two phenomena, i.e., a *resistance anomaly* and an *excess voltage*. The resistance anomaly shows up as an enhancement of the resistance value higher than its normal state resistance  $R_N$  near the critical temperature  $T_c$ . This resistance anomaly is related to a voltage in excess of the linear normal state voltage in the dc I-V characteristics. The basic physics behind these two phenomena is the two chemical potential model described in previous sections. Fig. 2.2.4 shows two pictures of how these two phenomena are detected by the usual four-probe transport measurement (Chapter 3). Fig. 2.2.4(a) is the case of charge imbalance near a NS interface. Inside the normal metal (N), only one chemical potential  $\mu_N$  can exist. With a finite potential across the sample,  $\mu_N$  varies linearly with position. In contrast, there exist two chemical potentials,  $\mu_q$  and  $\mu_p$ , near the NS interface inside the superconductor (S).  $\mu_q$  decays over a distance characterized by the charge imbalance length  $\Lambda_Q$ , while  $\mu_p$  varies on the much shorter length scale  $\xi$ . A voltage probe V- placed inside the charge imbalance region measures  $\mu_q$  or  $\mu_p$  depending on whether it is in a normal or superconducting state. A normal voltage probe detects  $\mu_q$  while a superconducting probe detects  $\mu_p$ . The other voltage probe V+

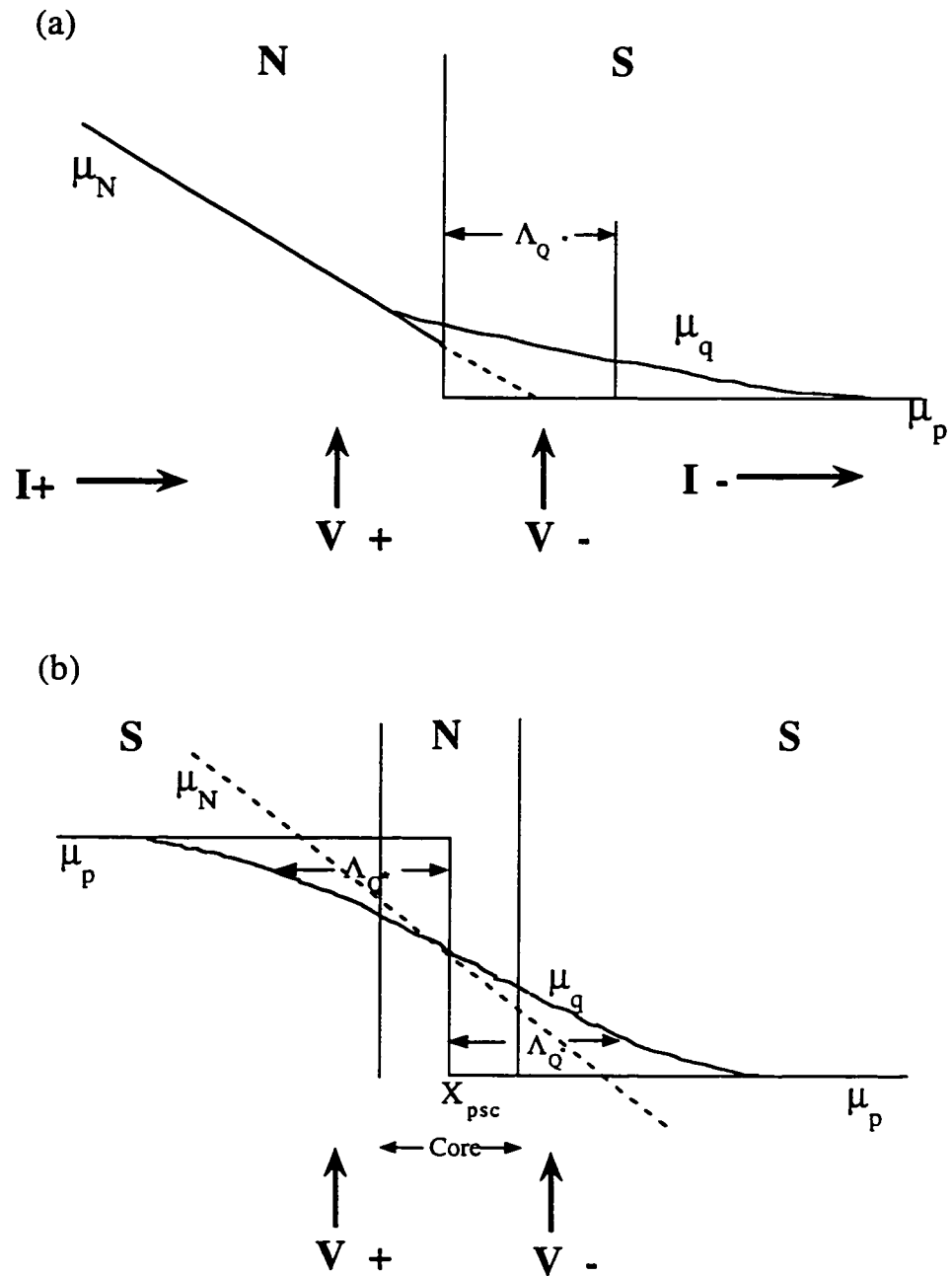


Fig. 2.2.4 Phenomenological picture of two chemical potentials model in the charge imbalance region near (a) a NS interface (b) a phase-slip center when a current is applied. The voltage probes ( $V+$ -) placed inside the charge imbalance region detect  $\mu_p$  and  $\mu_q$  when they are in superconducting and normal states respectively.

(made of the same material as N) directly detects  $\mu_N$ .

In the resistance anomaly experiment, only an ac current is applied. V- switches from a normal state to a superconducting state as the temperature is cooled through  $T_c$ . Therefore the potential difference detected by V+ and V- *increases* since V+ always measures  $\mu_N$ , while V- measures the potential under a transition from  $\mu_N$  to  $\mu_q$  and to  $\mu_p$  eventually, but only if the V- probe is less than a distance  $\Lambda_Q$  away from the interface. As a result, the resistance observed is higher than the normal state resistance. If both V+ and V- are placed inside the charge imbalance region of S, with V+ possessing a critical temperature  $T_{cl}$  a few millikelvin below  $T_c$  of the superconductor (and V-), V+ and V- would measure a potential difference between  $\mu_q$  and  $\mu_p$  at some intermediate temperature between  $T_{cl}$  and  $T_c$ , and the resistance anomaly would also appear.

The explanation of the observation of the excess voltage is similar to that for the explanation of resistance anomaly. Assume V+ and V- are on the normal and superconducting side of the interface respectively. As the dc current approaches the critical current  $I_c$  of the superconductor, a charge imbalance region is induced in S near the NS interface, being more pronounced as I is closer to  $I_c$ . Therefore, V+ and V- would detect a potential difference higher than the linear normal state value as a function of dc current. In mesoscopic systems, the differential resistance  $dV/dI$  is usually measured instead of the I-V characteristic. An additional ac current is then imposed on the dc current (Chapter 3).

$dV/dI$  measures the slope of I-V curve at each current. Since the excess voltage in an I-V curve shows up as a small bump in voltage just above the nonlinear portion of the superconducting I-V characteristic (Fig. 2.2.4(b)), the detected  $dV/dI$  first shows a positive resistive peak at  $I=I_c$ , followed by a *negative dip* at a slightly higher current, and eventually reaches a constant normal state value at higher currents. The negative  $dV/dI$  was demonstrated by Yu and Mercereau [70] in a beautiful experiment on a normal-superconducting wire in 70's. Recently, it was also observed by Park *et al.* [5] and C. Strunk *et al.* [9].

The two chemical potential model can also explain the resistance anomaly or excess voltage in a system where one or more phase-slip centers exist. In this system, charge imbalance is induced on both sides of the PSC (see Fig. 2.2.4(b)) and the model described above is applied to a SNS system. In next section, we briefly describe some important previous experiments that demonstrate the influence of charge imbalance in the transport problems of NS systems.

### 2.2.6 Previous experiments in charge imbalance

In the classic experiment by Clark [22], quasiparticles of high voltage are injected into a tin film (serves as a S) from an aluminum film (serves as a N) through a tunnel junction so that they are the dominant electron-like particles. A charge imbalance region was therefore created in the tin film. The difference between  $\mu_q$  and  $\mu_p$  is detected by measuring the voltage difference between the tin film and a normal-metal film coupled to the tin film. The voltage difference thus detected is related to the charge imbalance relaxation time  $\tau_Q$  of the tin film. Taking the conductance of the tunnel junction into account, Clark was able to fit

the data to a formula connecting the measured voltage and  $\tau_Q^*$ . The formula differs from that obtained from the RSM model mentioned in section 2.2.3 by adding the temperature dependence of the tunnel junction conductance in the voltage difference between  $\mu_q$  and  $\mu_p$ . The result showed a dramatic increase in  $\tau_Q^*$  near  $T_c$  of the tin film, and a saturation at temperatures far below  $T_c$ , in agreement with the theoretical prediction.

An alternative way of detecting charge imbalance was given by Dolan and Jackel [27] who measured the space dependent nature of the charge imbalance relaxation near a PSC. Fig. 2.2.5(a) shows a sample schematic of the experiment as well as the sample picture. A 1  $\mu\text{m}$  wide tin strip with a notch was fabricated with several equally-spaced S and N voltage probes placed along two sides of the tin strip. A PSC is preferably created at the notch. As a result, a charge imbalance region exists near the notch when a dc current is applied and S and N probes measure  $\mu_p$  (denoted by  $V_S$ ) and  $\mu_q$  (denoted by  $V_N$ ) directly along the imbalance region. As shown in Fig. 2.2.5(b),  $V_S$  is constant and  $V_N$  varies over a distance  $\sim 10 \mu\text{m}$ .

The influence of charge imbalance on the differential resistance  $dV/dI$  was demonstrated beautifully in a narrow WS wire by Yu and Mercereau [70], where W denotes a weak superconductor of which  $T_c$  and  $I_c$  are lower than those of S. Fig. 2.2.6 shows the experimental result as well as the sample schematic. An ac current superimposed on a dc current is injected from S to W along the wire. Near the WS

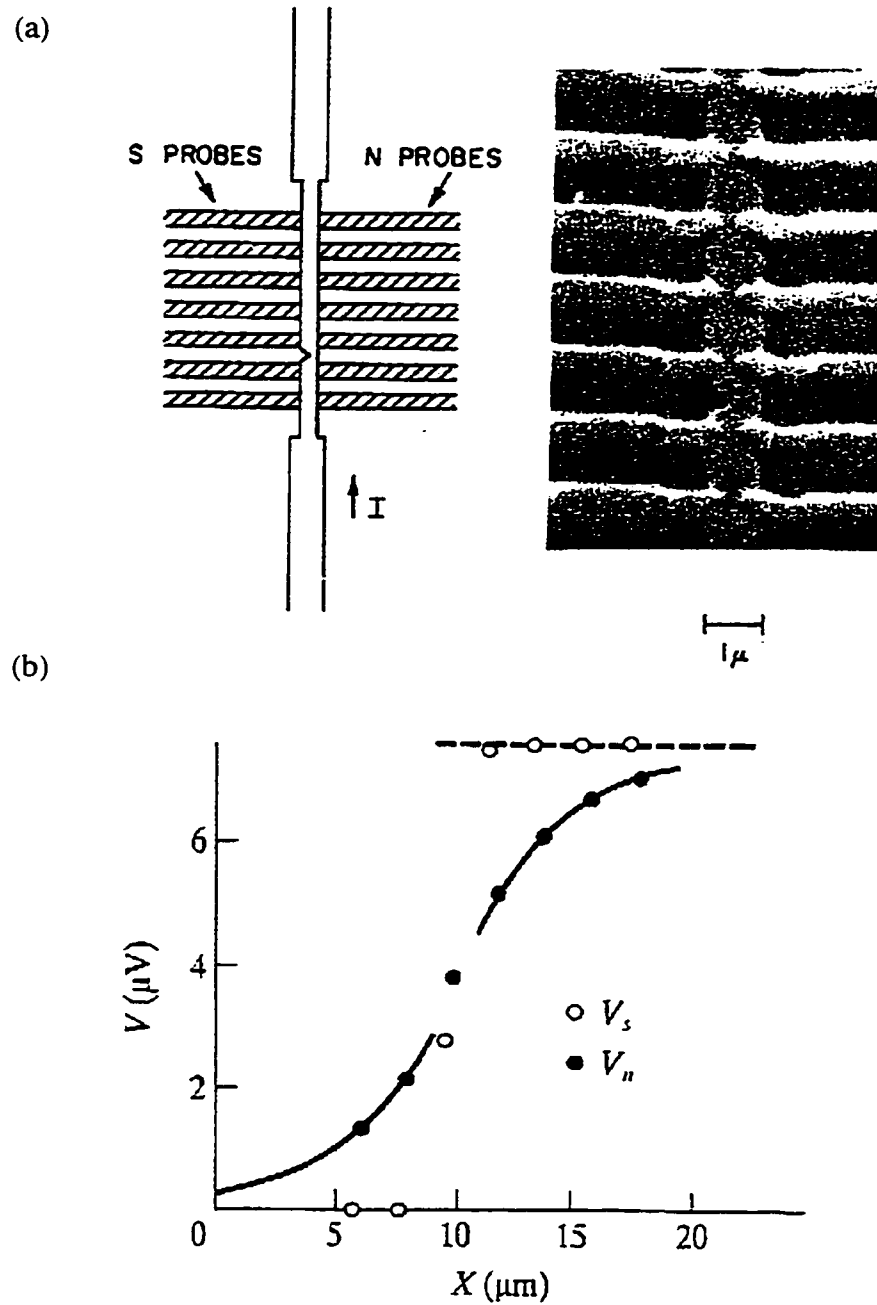


Fig. 2.2.5 Detection of charge imbalance near a phase-slip center (PSC). (a) sample schematic. A notch was to facilitate the formation a PSC. (b) The voltage measured with superconducting ( $V_s$ ) and normal leads ( $V_n$ ) directly show the spatial dependence of  $\mu_p$  and  $\mu_q$ . (From Dolan and Jackel, Ref. [27]).



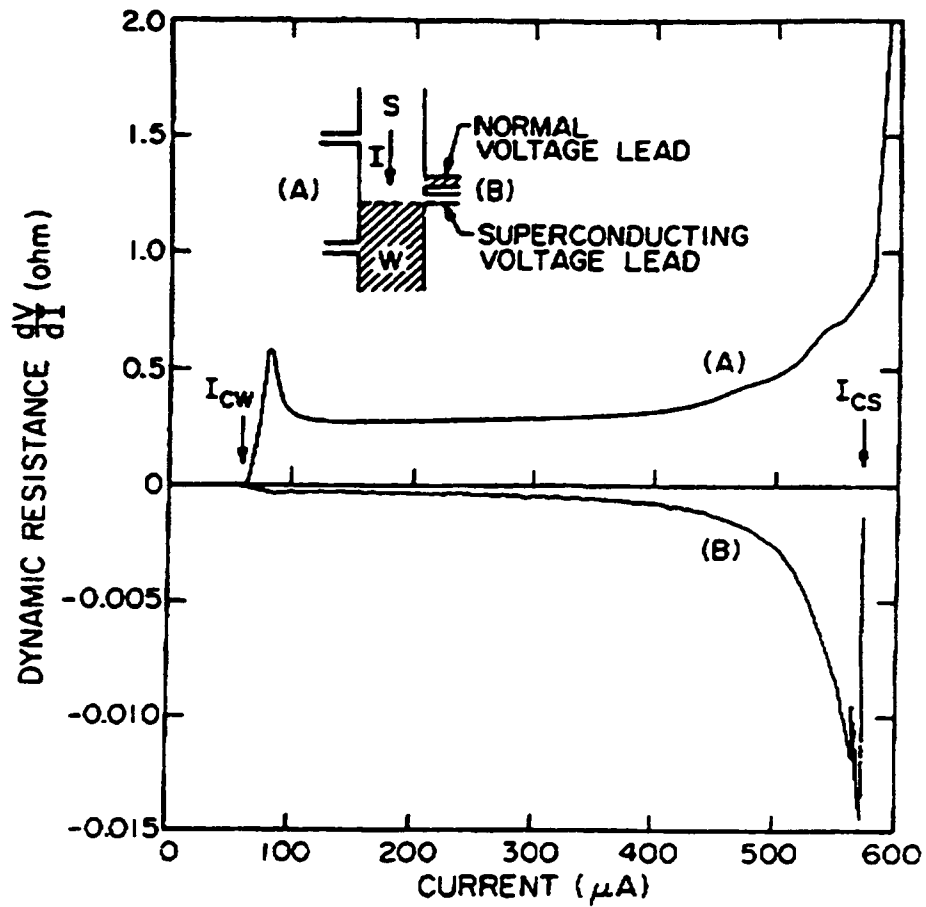


Fig. 2.2.6 Differential resistance as a function of dc current measured near a superconductor-weak superconductor interface. Curve A measured with probes A shows the transition of the region W at critical current  $I_{CW}$  and that of the region S at  $I_{CS}$ . Curve B measured with probes B shows the slope of the potential difference  $(\mu_p - \mu_q)/e$ . (From Yu and Mercereau, Ref.[70])

interface, charge imbalance takes place due to conversion of Cooper pairs into quasiparticles. Two sets of voltage probes are used to measure the differential resistance  $dV/dI$ . Probes A contains a microscopic S and a W lead located in the S and W side of the WS interface respectively. They are placed far away from the WS interface and therefore detect no charge imbalance. The purpose of probes A is to show the resistive transition of the W region at  $I=I_{cw}$  and that of the S region at  $I_{cs}$ , so that the charge imbalance can be clearly identified in the region  $I_{cw} < I < I_{cs}$ . Probes B (also a S and W lead), on the other hand, are placed in the S side region near the WS interface with a W lead located farther away from the interface than the S lead, having the same property as W region. Hence, the voltage measured represents  $\mu_q - \mu_p$ . As the current is increased from  $I_{cw}$ , a clear negative  $dV/dI$  is observed using Probes B, being larger near  $I_{cs}$ , in consistent with the two chemical potential model described in the last section.

As the dimensions of the samples are decreased, charge imbalance was also observed in pure mesoscopic superconductors. In the experiment of Santhanam *et al.* [1], the resistance anomaly was observed in a 1D aluminum wire without any intentionally created PSC or NS interface. This resistance anomaly (Fig. 2.2.7(a)) was explained as the consequence of a charge imbalance region near a dynamic PSC in the sample. This explanation was based on some further tests of the properties of charge imbalance in the sample. First, the resistance anomaly was only observed in some short segments of the Fig. 2.2.6 sample which is in consistent with the charge imbalance relaxation picture. Second, at the temperature  $T_{max}$  corresponding to the maximal resistance peak in  $R(T)$ , the differential resistance shows a small bump at zero-current (Fig. 2.2.7(b)). As  $T$  moves

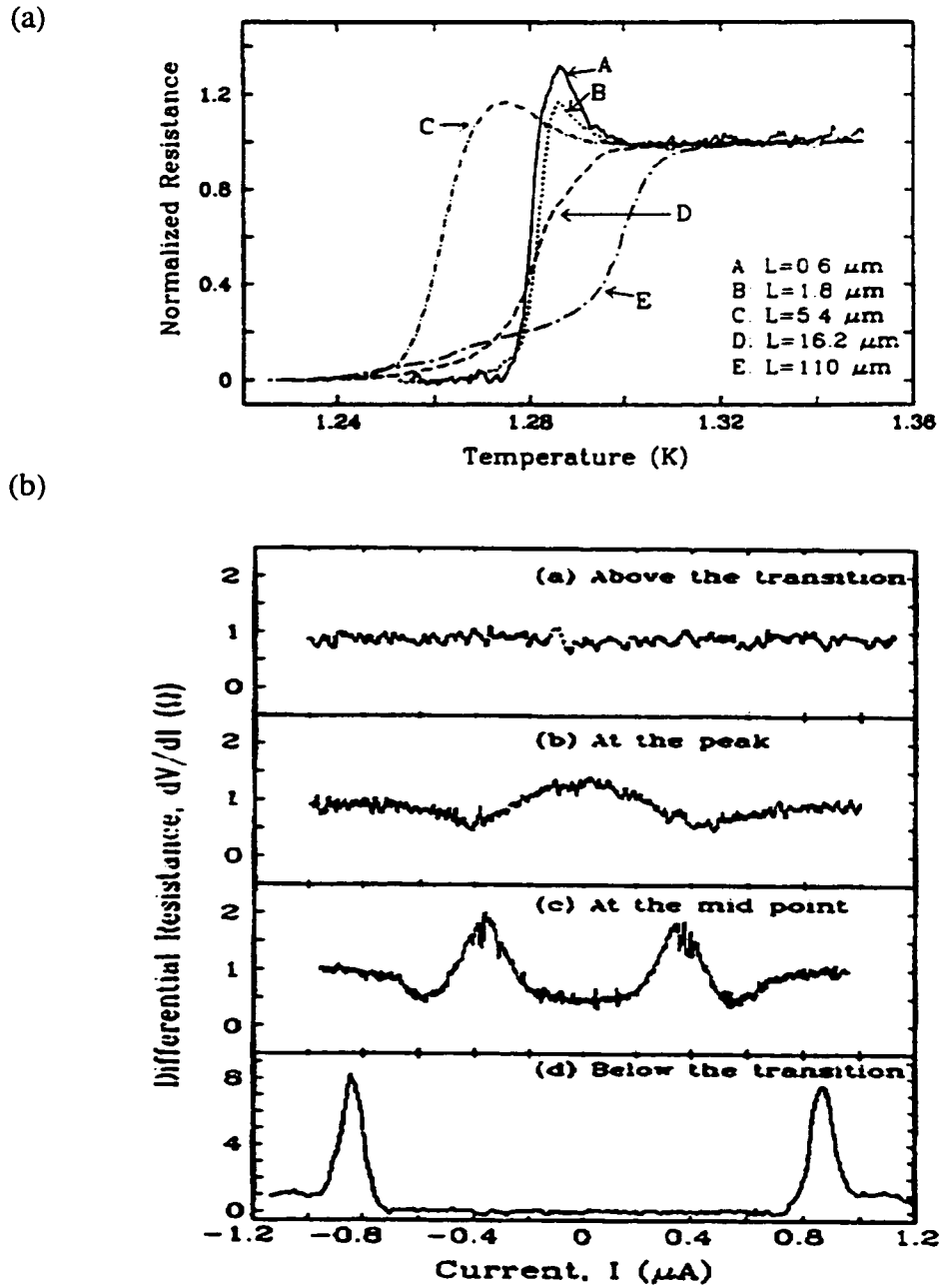


Fig. 2.2.7 (a) Normalized resistance as a function of temperature measured on different segments of a 1D Al wire. Short segments (A, B, C) show clear enhanced resistance above the normal state resistance. (b) Differential resistance of segment A in (a) as a function of dc current measured at different temperatures near the maximal resistive peak of segment A. (From Santhanam *et al.* Ref.[1]).

away from  $T_{\max}$ , the resistance bump is reduced and eventually reaches its normal state resistance at higher temperatures. Third, the resistance anomaly is suppressed when a small magnetic field of a few gauss is applied and completely disappears at a field of magnitude  $\sim 20$  gauss. While these tested properties all show the sign of charge imbalance, the location and origin of the dynamic PSC was not identified. In the experiment of Kim *et al.* [4], similar results were observed.

In the experiment of Park *et al.* [5], a clear dynamic PSC was created in a system similar to that of Yu and Mercereau. This dynamic PSC moves along the W region as the dc current is increased from zero. As a result, a nonlocal charge imbalance was observed through a series of negative  $dV/dI$  dips measured with various W and S voltage probes along the WS wire. Each negative  $dV/dI$  results from the fact that a PSC enters a new region between two voltage probes at a distance of few microns away from the segment where the differential resistance was measured. Although this experiment successfully identified the location of the PSC and showed an interesting nonlocal property, the system was two dimensional. Furthermore, it is not a pure superconductor. Therefore, the questions raised by the experiment of Santhanam *et al.* [1] remain.

In Chapter 4, we will discuss the resistance anomaly in our experiments on mesoscopic superconductors similar to that of Santhanam *et al.* [1]. The resistance anomaly observed in our system differs from Ref. [1] in the fact that it is induced by applying external parameters, i.e., radio-frequency radiation, magnetic field, and noise current.

## 2.3 Proximity effect

The theory discussed in the sections above deals primarily with nonequilibrium superconductivity. In this section we turn to the normal-metal side of a N-S boundary. The related physics is the so-called *proximity effect* in which the superconductivity can penetrate into the normal metal by inducing pair correlations across the N-S boundary. We first briefly describe the proximity effect within the Ginzburg-Landau (G-L) picture in this section. In next section a theory based on quasiclassical Green functions will be introduced in order to explain some recent experimental observation of the proximity effect.

Based on G-L theory, the proximity effect near a N-S boundary in one dimension can be described by the order parameter  $\psi(x)$ . In the superconductor, the G-L equation for  $\psi(x)$  can be linearized since  $\psi(x)$  is small [33]:

$$\frac{\hbar^2}{2m} \frac{d^2\psi(x)}{dx^2} = -\alpha\psi(x). \quad (2.3.1)$$

where  $\alpha$  is a function of temperature. The boundary condition for Eq. 2.3.1 is:

$$\left( \frac{d\psi(x)}{dx} \right)_{x=0} = \frac{\psi(x)}{b} \quad (2.3.2a)$$

$$\psi(x \rightarrow \infty) = 0 \quad (2.3.2b)$$

where  $b$  is a parameter depending on the thickness and the properties of the normal metal and  $x$  measures the distance into the normal metal from the NS interface.  $\psi(x)$  from the N-S boundary can be shown to have the asymptotic form [33] (using Eq. 2.3.1 and 2.3.2):

$$\psi(x) = \phi(x)e^{-x/\xi_N} \quad (2.3.3)$$

where  $\phi(x)$  is a slowly varying function of the distance from the N-S boundary and  $b$  is converted into the penetration length  $\xi_N$ . In the clean limit ,

$$\xi_N = \frac{\hbar v_F}{2\pi k_B T}, \quad (2.3.4)$$

where  $v_F$  is the Fermi velocity in N and  $k_B$  is the Boltzmann constant. In the dirty limit,  $\xi_N$  is replaced by the normal metal coherence length:

$$\xi(T) = \sqrt{\frac{\hbar D}{2\pi k_B T}} \quad (2.3.5)$$

where  $D = v_F \ell / 3$  is the diffusion constant and  $\ell$  is the electron mean free path. Fig. 2.3.1 shows the behavior of the G-L order parameter near a NS interface in the diffusive regime.

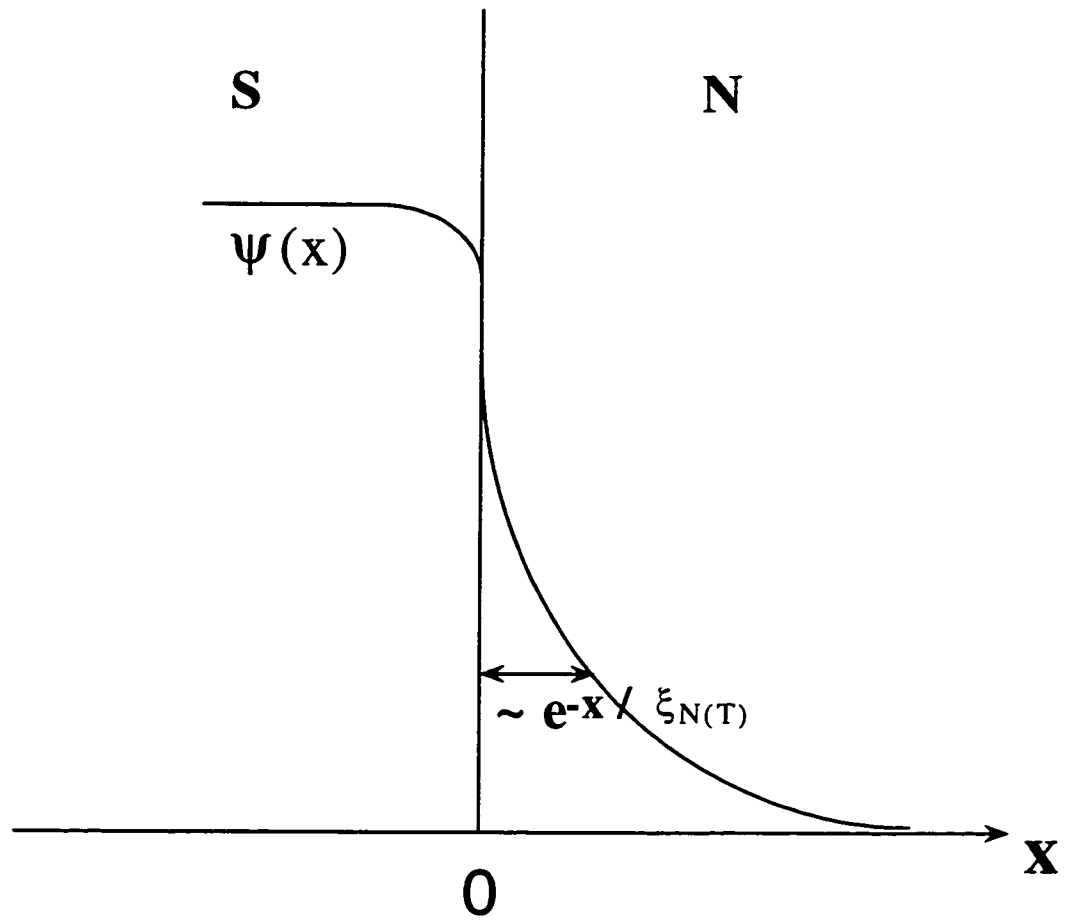


Fig. 2.3.1 Description of the proximity effect based on Ginzburg-Landau theory.

$\psi(\xi)$  decays exponentially over a length  $\xi_N(T)$  and approaches zero eventually. The consequence of the proximity effect is a decrease in the resistance  $R$  of the normal metal. As we can see in Eq. 2.3.5,  $\xi_N(T)$  increases as the temperature decreases. Therefore, one expects that  $R$  decreases monotonically as a function of temperature.

## 2.4 Quasiclassical Green functions theory

The proximity effect described in last section is determined by the space dependent G-L order parameter. However, as was realized by researchers, Andreev reflection [36] is the microscopic mechanism responsible for the proximity effect. A consequence of Andreev reflection is the existence of electron-hole pair coherence in the normal metal which is energy dependent. Therefore, the proximity effect is also dependent on the energy of the electron. Furthermore, G-L theory is only valid near  $T_c$  and hence provides no information for the proximity effect at temperatures far below the transition temperature. The first attempt at describing the proximity effect was by Blonder, Tinkham, and Klapwijk [71] (BTK), who solved the Bogoliubov equations for a NS interface combining both Andreev and ordinary reflections to obtain the electron-like and hole-like wavefunctions. By assuming a  $\delta$ -function potential barrier of variable strength at the NS boundary, BTK were able to compute the conductance of a NS interface. The result beautifully describes the interface conductance influenced by the interface barrier as well as the energy of the electrons. However, BTK assumed simple plane waves for particles in the normal metal. Therefore, the theory offers no information on the proximity effect in the presence of



impurities in the normal metal. Unique phenomena such as the zero bias anomaly (ZBA) [72] and enhanced Aharonov-Bohm effect [44] have been observed, confirming the importance of the role of quantum coherent effects inside the normal metal. An approach similar to BTK has been extended to include impurity scattering in the normal metal [73-75]. In the attempt by Marmorkos, Beenakker and Jalabert [75], the conductance of the NS system is expressed in terms of transmission matrices and is obtained by numerically computing the transmission coefficients of the matrices. While this approach has successfully explained several results, the transmission matrices are usually not easy to calculate [47].

An alternative way of treating this problem is based on the development of quasiclassical Green functions theory [46-53, 76-80]. Instead of calculating the transmission matrices, this theory obtains a set of equations for the impurity averaged Green functions. With the aid of appropriate boundary conditions for different systems, impurity-averaged transport properties are directly obtained from these equations. Since this approach has been successful in accounting for the proximity effect of most NS systems where N is in diffusive regime, we briefly describe this theory in the following sections.

#### 2.4.1 Green functions in a dirty superconductor

The Green functions technique describing non-equilibrium superconductivity in an inhomogeneous superconductor or in a normal metal with proximity effect is based on the Keldysh diagrammatic technique [81]. In Nambu space, the matrix form of the Green functions is [46-53]:

$$\tilde{G} = \begin{pmatrix} \hat{G}^R & \hat{G}^K \\ 0 & \hat{G}^A \end{pmatrix} \quad (2.4.1)$$

where  $\hat{G}^A$ ,  $\hat{G}^R$  and  $\hat{G}^K$  are the advanced, retarded, and Keldysh Green functions. Here the “ $\sim$ ” denotes 4x4 matrices, and the “ $\wedge$ ” denotes 2x2 matrices which are given by:

$$\hat{G}^i(1, 1') = \begin{pmatrix} G^i(1, 1') & F^i(1, 1') \\ F^{i+}(1, 1') & -G^i(1, 1') \end{pmatrix} \quad (2.4.2)$$

where  $i = R, A, K$ . The normal and anomalous Green functions are given by :

$$G^R(1, 1') = -i\theta(t_1 - t_{1'}) \langle [\psi(1), \psi^+(1')]_+ \rangle \quad (2.4.3a)$$

$$G^A(1, 1') = i\theta(t_{1'} - t_1) \langle [\psi(1), \psi^+(1')]_+ \rangle \quad (2.4.3b)$$

$$G^K(1, 1') = -i \langle [\psi(1), \psi^+(1')] \rangle \quad (2.4.3c)$$

$$F^R(1, 1') = -i\theta(t_1 - t_{1'}) \langle [\psi(1), \psi(1')]_+ \rangle \quad (2.4.3d)$$

$$F^A(1, 1') = i\theta(t_{1'} - t_1) \langle [\psi(1), \psi(1')]_+ \rangle \quad (2.4.3e)$$

$$F^K(1, 1') = i \langle [\psi^+(1), \psi^+(1')] \rangle \quad (2.4.3f)$$

where  $\psi(1) = \psi(t_1, \mathbf{r}_1)$  is the electron field operator,  $\langle \rangle$  denotes the statistical average in the equilibrium state of the system, and  $[\ ]_+$  and  $[\ ]$  denote the anti-commutator and the

commutator respectively. Two properties are observed from Eq. 2.4.3. First, the Keldysh Green function  $\hat{G}^K$  differs from the conventional retarded and advanced Green functions  $\hat{G}^R$  and  $\hat{G}^A$  in that it contains no time ordering, and contains a commutator instead of an anti-commutator. Second, the normal Green functions  $\hat{G}^i$  are one-particle Green functions and describe normal correlations, while the anomalous Green functions  $\hat{F}^i$  are pair Green functions and describe superconducting correlations. ( $i=R, A, K$ )

In the quasiclassical approximation [49-50, 82-85], one can introduce the so-called quasiclassical Green function  $\check{g}$ , which has the form of:

$$\check{g}(\mathbf{r}, \hat{\mathbf{k}}, t_1, t_1') = \frac{i}{\pi} \int d\varepsilon_{\mathbf{k}} \check{G}(\mathbf{r}, \mathbf{k}, t_1, t_1'). \quad (2.4.4)$$

where

$$\varepsilon_{\mathbf{k}} = \hbar^2 \mathbf{k}^2 / 2m - \mu,$$

$$\check{G}(\mathbf{r}, \mathbf{k}) = \int d\mathbf{r}' \exp(-i\mathbf{k}\mathbf{r}') / \hbar \check{G}(\mathbf{r} + \frac{1}{2}\mathbf{r}', \mathbf{r} - \frac{1}{2}\mathbf{r}'),$$

$\mathbf{r} = (\mathbf{r}_1 + \mathbf{r}_1')/2$  and  $\mathbf{r}' = \mathbf{r}_1 - \mathbf{r}_1'$ . The quasiclassical Green function thus defined only depends on the direction  $\hat{\mathbf{k}}$  of the momentum  $\mathbf{k}$ , while the magnitude  $k$  is fixed at the Fermi wave vector  $k_F$ . This is because we have made the assumption that all the physical quantities of interest vary spatially on a length scale much larger than the Fermi wavelength. The normalization for the quasiclassical Green function is:

$$\int dt_1 \check{g}(t_1, t_1) \check{g}(t_1, t_1) = I \delta(t_1 - t_1). \quad (2.4.5)$$

In the diffusive regime we can expand  $\check{g}$  to first order in spherical harmonics:

$$\check{g} = \check{g}_s + \mathbf{k} \check{g}_k, \quad \mathbf{k} \check{g}_k \ll \check{g}_s, \quad (2.4.6)$$

where  $\check{g}_k$  is related to  $\check{g}_s$  through the normalization condition Eq. 2.4.5. The Green's function is then averaged over all angles of  $\mathbf{k}$ . In the stationary case the Green function only depends on the time difference  $\tau = t_1 - t_2$ . Taking the Fourier transform with respect to  $\tau$  one obtains the equation of motion for the Green function and the normalization condition:

$$-D \nabla (\check{g}_\epsilon \nabla \check{g}_\epsilon) + i[\check{H}, \check{g}_\epsilon] + i[\check{\Sigma}, \check{g}_\epsilon] = 0, \quad (2.4.7a)$$

$$\check{g}_\epsilon^2 = I, \quad (2.4.7b)$$

where  $\check{g}_\epsilon = \int d\tau \check{g}_s(\tau) \exp(i\epsilon\tau)$ ,  $D = v_F \ell / 3$  is the normal state diffusion constant, and  $\ell$  is the

elastic mean free path. The self-energy matrix  $\check{\Sigma}$  describes processes due to spin-flip scattering and inelastic scattering with phonons. The Hamiltonian  $\check{H}$  is given by

$\tilde{H} = e\phi\tilde{I} + \varepsilon\tilde{\sigma}_z + \tilde{\Delta}$ , where  $\phi$  is the electrical potential,  $\varepsilon$  is the electron energy relative to the

Fermi energy and  $\tilde{\Delta}$  and  $\tilde{\sigma}_z$  are given by:

$$\tilde{\Delta} = \begin{pmatrix} \hat{\Delta} & 0 \\ 0 & \hat{\Delta} \end{pmatrix}, \quad \hat{\Delta} = \begin{pmatrix} 0 & \Delta \\ -\Delta^* & 0 \end{pmatrix}, \quad (2.4.8a)$$

$$\tilde{\sigma}_z = \begin{pmatrix} \hat{\sigma}_z & 0 \\ 0 & \hat{\sigma}_z \end{pmatrix}, \quad \hat{\sigma}_z = \begin{pmatrix} 1 & 0 \\ 0 & -1 \end{pmatrix}, \quad (2.4.8b)$$

where  $\Delta$  is the pair potential in the metal.

Eq. 2.4.7 is the Usadel equation [54] in Nambu space. Elastic impurity scattering has been taken into account in the Born approximation, causing the presence of the elastic mean free path  $\ell$  in the diffusion constant. Eq. 2.4.7 has to be completed with the self-consistency equation for the pair potential in the normal metal:

$$\hat{\Delta}(\mathbf{r}) = \frac{N(0)V}{4i} \int_0^{\hbar\omega_D} d\varepsilon \text{Tr}\{\hat{G}^K(\hat{\sigma}_x - i\hat{\sigma}_y)\}. \quad (2.4.9)$$

where  $V$  is the strength of the pair interaction and  $N(0)$  is the electronic density of states at the Fermi level.

The retarded and advanced Green functions determine the characteristics of the quasiparticle energy spectrum while the Keldysh Green function describes the way the particles are distributed at each energy and temperature.  $\hat{G}^K$  can be expressed in terms of  $\hat{G}^R$ ,  $\hat{G}^A$  and a distribution function matrix  $\hat{f}$ :

$$\hat{g}_\epsilon^K = \hat{g}_\epsilon^R \hat{f} - \hat{f} \hat{g}_\epsilon^A \quad (2.4.10a)$$

$$\hat{f} = f_0 \hat{1} + f_3 \hat{\sigma}_z. \quad (2.4.10b)$$

where  $f_0$  and  $f_3$  are the odd and even components of  $\hat{f}$  with respect to the Fermi energy respectively. To solve the transport problem, the spectrum at equilibrium is first determined by solving the retarded Green function component of the Usadel equation combined with appropriate boundary conditions associated with the particular system. The Keldysh component is then solved in combination with the boundary conditions for the distribution function when the system is driven out of equilibrium. Finally, the physical quantities of interest are calculated using the three Green functions  $\hat{g}^K$ ,  $\hat{g}^R$  and  $\hat{g}^A$ .

#### 2.4.2 Boundary conditions

The boundary conditions for the quasiclassical Green functions have been derived by Kuprianov and Lukichev [85]. The formula reads:

$$\bar{\sigma} S \check{g} \partial_\mu \check{g} = \frac{G_b^n}{2} [\check{g}(x_{b-}), \check{g}(x_{b+})] \quad (2.4.11)$$

where  $\sigma$  is the conductivity of the wire,  $S$  the cross section of the wire,  $x_{b-}$  and  $x_{b+}$  denote the coordinates on two sides of the interface and  $G_b^n$  is the normal state conductance of the interface. Eq. 2.4.11 confirms the continuity of the Green functions across the interface. This continuity equation can be interpreted as the conservation of the “spectral current”  $\sigma \nabla \hat{G}$ . The existence of the interface conductance is obvious since it influences the proximity effect through the Green functions. However, one should note it is the ratio of the conductance of the interface to the normal wire that determines the penetration strength of the proximity into the normal metal.

The next step is to determine the boundary conditions at the normal and superconducting reservoirs. In the case of sufficiently small quasiparticle, thermal and Thouless energies;  $\epsilon, k_B T, \hbar D/L^2 \ll \Delta$ , Stoof and Nazarov [50] rewrote  $\hat{g}_\epsilon^A$  as:

$$\hat{g}_\epsilon^A = \frac{-1}{\sqrt{(\epsilon - i\delta)^2 - |\Delta|^2}} \begin{pmatrix} \epsilon & \Delta \\ -\Delta^* & -\epsilon \end{pmatrix}, \quad (2.4.12)$$

where  $\delta$  is an infinitesimally small positive number. In a normal reservoir,  $\Delta = 0$  and

$\hat{g}_\epsilon^A = -\hat{\sigma}_z$ . In a superconducting reservoir with phase  $\phi$ ,  $\Delta = \Delta_s e^{i\phi}$  and

$\hat{g}_\epsilon^A = \hat{\sigma}_x \sin\phi + \hat{\sigma}_y \cos\phi$ . The retarded Green function is given by the equation:

$$\hat{g}_\epsilon^R = -\hat{\sigma}_z \hat{g}_{-\epsilon}^A \hat{\sigma}_z \quad (2.4.13)$$

Finally, the Keldysh Green function can be decomposed into an even function  $\hat{f}_3$  and an odd function  $\hat{f}_0$ :

$$\hat{f} = f_0 \hat{1} + f_3 \hat{\sigma}_z \quad (2.4.14)$$

where  $f_0$  and  $f_3$  are given by the following forms in a reservoir biased at a voltage  $V$  and at temperature  $T$ :

$$f_0 = \frac{1}{2} \left( \tanh \frac{\epsilon + eV}{2k_B T} + \tanh \frac{\epsilon - eV}{2k_B T} \right) \quad (2.4.15a)$$

$$f_3 = \frac{1}{2} \left( \tanh \frac{\epsilon + eV}{2k_B T} - \tanh \frac{\epsilon - eV}{2k_B T} \right) \quad (2.4.15b)$$

### 2.4.3 Parametrization of the Green functions

Using the normalization condition, the quasiclassical Green functions governed by the Usadel equation can be parametrized. This makes them easier to manipulate.  $\check{G}^R$  and  $\check{G}^A$  are parametrized in the following form:

$$\check{G}^R = \begin{pmatrix} \cos\theta & e^{-i\phi} \sin\theta \\ e^{i\phi} \sin\theta & -\cos\theta \end{pmatrix} \quad (2.4.16a)$$



$$\check{G}^A = \begin{pmatrix} -\cos\theta^* & e^{-i\phi}\sin\theta^* \\ e^{i\phi}\sin\theta^* & \cos\theta^* \end{pmatrix} \quad (2.4.16b)$$

where  $\theta(\mathbf{r}, \epsilon)$  is a complex function and  $\phi(\mathbf{r}, \epsilon)$  is a real superconducting phase. The Usadel equation in one dimension in the absence of magnetic field can be expressed as follows [48, 53, 86]:

$$\frac{\hbar D}{2} \frac{\partial^2 \theta}{\partial x^2} + (i\epsilon - \hbar \gamma_{sf} \cos\theta) \sin\theta + \Delta(x) \cos\theta = 0. \quad (2.4.17)$$

where  $\gamma_{sf}$  is the spin-flip scattering rate and the inelastic scattering rate is neglected. The boundary conditions for the interface then read:

$$(\sigma S) \partial_x \theta(x, \epsilon) = G_b^n \sin[\theta(x_{b+}) - \theta(x_{b-})]. \quad (2.4.18)$$

and for the S and N reservoirs:

$$\theta = 0 \quad \text{in a N reservoir} \quad (2.4.19a)$$

$$\theta = \begin{cases} \frac{\pi}{2} + i \frac{1}{2} \ln \frac{\Delta + \epsilon}{\Delta - \epsilon} & \text{for } \epsilon < \Delta \\ i \frac{1}{2} \ln \frac{\epsilon + \Delta}{\epsilon - \Delta} & \text{for } \epsilon > \Delta \end{cases} \quad \text{in a S reservoir} \quad (2.4.19b)$$

The self-consistency equation for the pair potential becomes:

$$\Delta(x) = N(0)g \int_0^{\hbar\omega_D} \tanh\left(\frac{\epsilon}{2k_B T}\right) \text{Im}[\sin\theta] d\epsilon. \quad (2.4.20)$$

#### 2.4.4 Some remarks on the theory

Some important concepts of the Usadel equation are presented in this section. The properties of the parametrized angles, i.e.,  $\theta$  and  $\phi$ , can be summarized in a simple physical description introduced by Yu. V. Nazarov [47]. Neglecting spin-flip and inelastic scattering, and assuming zero pair interaction in the normal metal,  $\theta$  becomes a real function at zero energy. One can describe  $\theta$  and its boundary conditions by a real unit sphere [47, 53] as shown in Fig. 2.4.1. The proximity effect along a normal-metal wire connected to a N reservoir at one end and a S reservoir at another can be described by any point on the surface of the unit sphere. The north pole represents the normal state ( $\theta = 0$ ) while the equator represents the superconducting state ( $\theta = \pi/2$ ). If there exist two superconductors the phase difference  $\phi$  between the two superconductors is represented by the angle  $\phi$ . The physical quantities involved in the proximity effect are therefore modulated by  $\phi$ . Experimentally, one can modulate  $\phi$  by applying a magnetic field threading a hybrid loop, part of which is superconducting and the rest normal. Alternatively, one can also apply current through a long superconducting wire to change its phase gradient along the wire. Hence, normal metals connected to different parts of the S

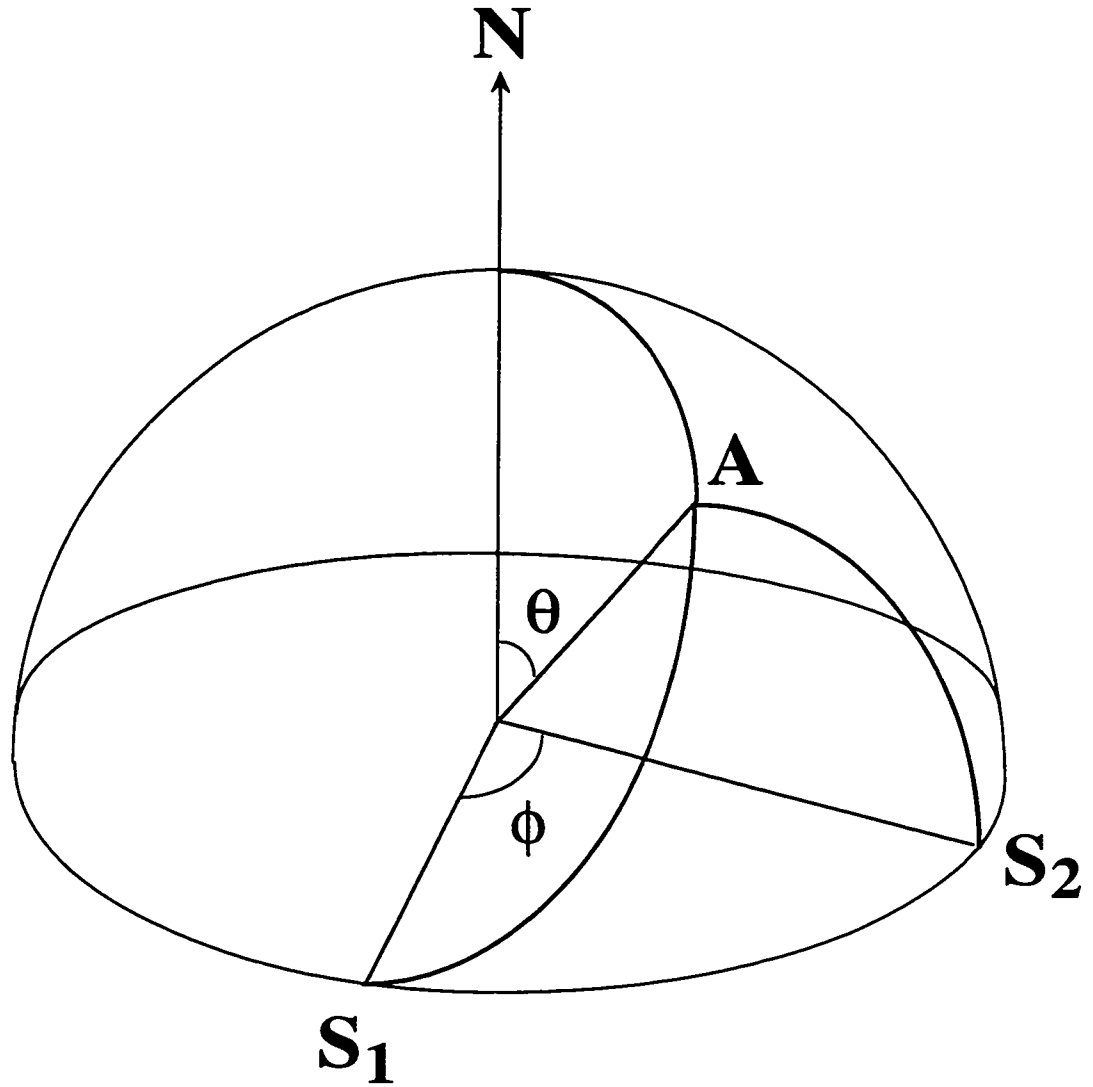


Fig. 2.4.1 A real unit sphere describing the proximity effect in a normal metal (N) connected to two superconductors ( $S_1$  and  $S_2$ ) at zero electron energy. The north pole represents the N reservoir and the equator represents the S reservoir. Between the N and S reservoirs the proximity effect is described by any point on the surface of the sphere. Point A represents the proximity effect described by a parametrized angle  $\theta$  obeying the Usadel equation and modulated by a phase difference  $\phi$  between the two superconductors  $S_1$  and  $S_2$ .

wire acquire different phases [42-44, 87-88].

The proximity effect described by the Usadel equation is a long range pair correlation. Consider a rather long normal wire connected at its two ends to a N and a S reservoir respectively. The pair correlation induced by the S reservoir exists everywhere along the wire since it starts with a finite complex value at the S reservoir and vanishes at the N reservoir.  $\theta(\epsilon, x)$  along the wire depends not only on the position but also on the energy, which is different from the proximity effect based on the Ginzburg-Landau picture [33]. This is observed in Eq. 2.4.17 which shows  $\theta(\epsilon, x)$  decays qualitatively over a length scale the order of  $(\hbar D/\epsilon)^{1/2}$ . As  $\epsilon$  approaches zero, the decay length becomes very long and the pair correlation extends to the whole system. The manifestation of this long range correlation in the transport properties is described by an effective diffusive coefficient ( $D(\epsilon, x)$ ) in the normal. Along the normal wire of length  $L$ ,  $D(\epsilon, x)$  shows a maximum at some intermediate energy of the order of Thouless energy  $\hbar D/L^2$  of the system, recovers its normal state value  $D$  both at zero and at high energies as shown in Fig. 2.4.2. The strange behavior of the reentrance effect occurs when the decay length exceeds the dimensions of the system. At zero energy the decay length is infinite and a pair correlation exists but the effective diffusion coefficient is equal to its normal state value. Therefore the resistance of the normal metal regains its normal state resistance. We will show this effect explicitly in Chapter 5 when we apply the quasiclassical Green functions formula to the experimental results of several NS samples.

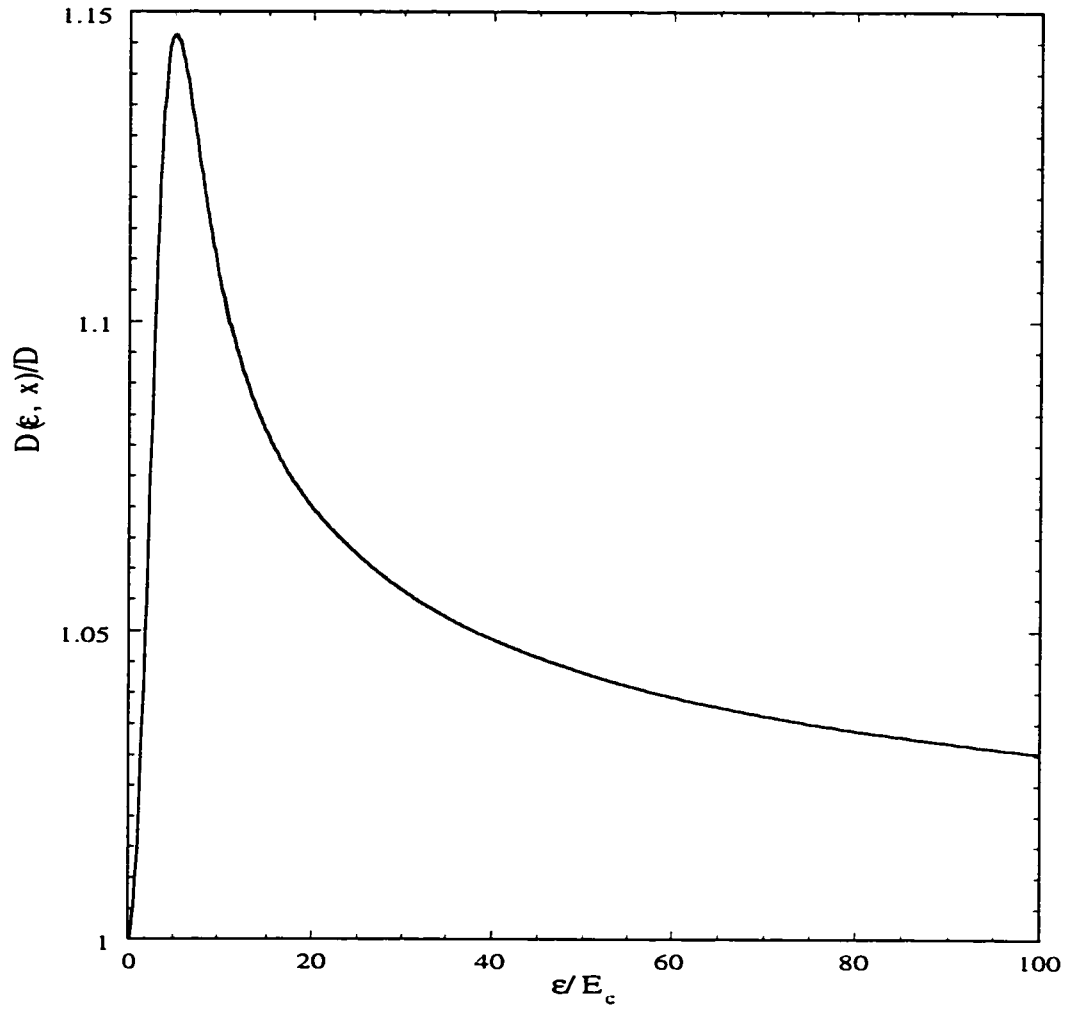


Fig. 2.4.2 Normalized effective diffusion coefficient  $D(\epsilon, x)/D$  as a function of reduced energy  $\epsilon/E_c$  at any location  $x$  along a normal-metal wire of length  $L$  connected to a normal reservoir in one end and a superconducting reservoir in the other.  $D$  and  $E_c$  are the normal state diffusion constant and Thouless energy respectively, where  $E_c = \hbar D/L^2$ .

#### 2.4.5 Previous experiments on the reentrance effect

In the beginning of this section, we use a plot obtained by Nazarov *et al.* [50] (see Fig. 2.4.3) to explain some important properties of the proximity effect based on the quasiclassical Green functions theory applied to a diffusive metal connected to a superconductor. The sample geometry is shown in the inset of Fig. 2.4.3, where a cross-shaped diffusive metal is connected to a superconducting loop at two NS interfaces. This superconducting loop provides a way of changing the phase difference between the two NS interfaces. The resistance of the segment between point A and A' would be measured by a four-probe ac lock-in technique described in Chapter 3 with the ac current applied along the direction of the arrows. Various curves in the plot correspond to the normalized resistance of the segment between point A and A' as a function of temperature  $T$  at different values of the phase difference between the two NS interfaces, where  $T$  is incorporated in the formula  $\xi_N^2 = D/\pi T$ . At a particular temperature, one can see the resistance oscillates between the top and bottom curves corresponding to a phase difference equal to  $\pi$  and 0 respectively, which shows a period of oscillation equal to  $2\pi$ . The manifestation of the reentrance effect in transport is usually shown in three measurements, i.e., resistance as a function of temperature  $R(T)$ , differential resistance as a function of voltage  $dV/dI(V)$  and the amplitude of the magnetoresistance oscillations as a function of temperature. These features are clearly seen in Fig. 2.4.3. For  $R(T)$ , each curve shows a minimum resistance at an intermediate temperature while the normal state resistance is recovered at zero and high temperatures. For  $dV/dI(V)$  one can replace  $k_B T$  with  $eV$  and obtain behavior similar to  $R(T)$ . The reentrance effect revealed in the amplitude of magnetoresistance oscillations is shown in the resistance difference between any two curves in Fig. 2.4.3. This resistance

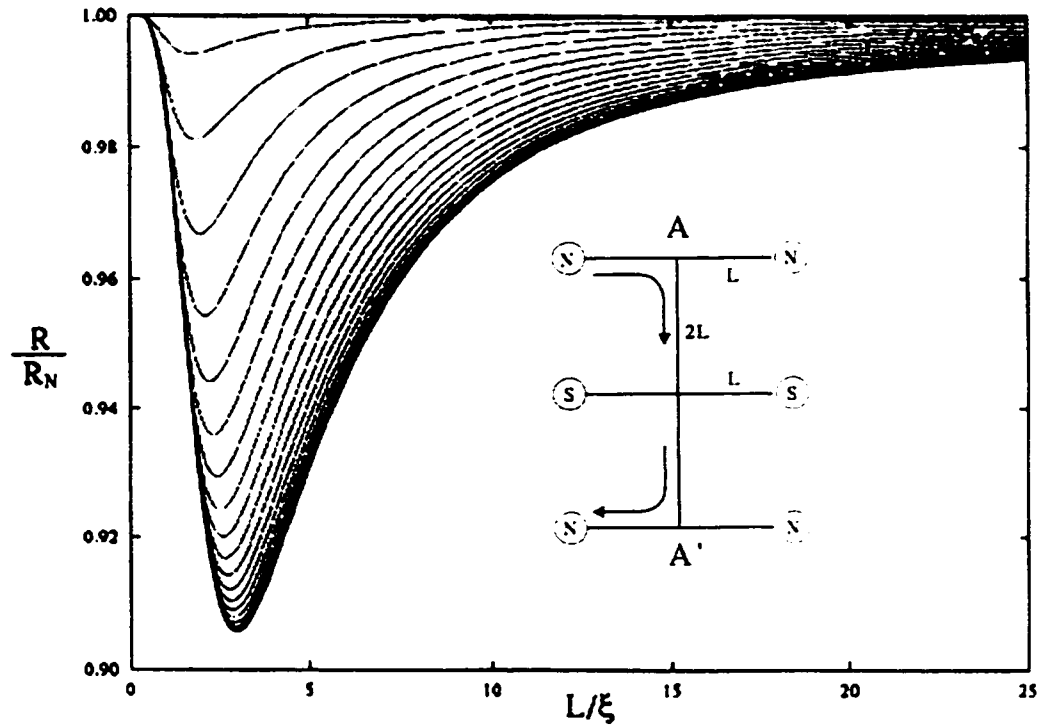


Fig. 2.4.3 Calculated normalized values of the resistance  $R/R_N$  between A and A' (inset) as a function of temperature at different phase difference between two superconductors S. The current flows in the direction of arrows and the voltage is measured between the other two N leads. The phase difference varies from 0 (bottom curve) to  $\pi$  (top curve). The temperature is incorporated in the form  $\xi_N^2 = D/\pi T$ . (From Nazarov *et al.* Ref. [50]).

difference represents the amplitude of oscillations, which increases as the temperature is decreased, reaches a maximum, and decreases again at lower temperatures, being equal to zero at zero temperature.

So far, to our knowledge, the reentrance effect has been observed in two systems. One is in a semiconductor connected to a superconductor (Sm-S). The other is in a diffusive metal connected to a superconductor (N-S).

In the Sm-S system, den Hartog *et al.* [15, 16] reported reentrant behavior in a geometry where a diffusive two dimensional electron gas (2DEG) is coupled to a superconductor to form a loop. The reentrance effect was observed in the measurement of  $dV/dI(V)$  and the amplitude of  $R(H)$  oscillations as a function of  $V$ . Later, Toyoda *et al.* [17] observed the reentrance effect in the magnetoresistance oscillations of a 2DEG connected to a superconducting loop. Due perhaps to the difficulty in controlling the shape of the 2DEG, it is not easy to quantitatively compare these experiments with the theoretical prediction, although they are qualitatively in agreement with the theory of quasiclassical Green functions.

In the N-S system, Courtois *et al.* [40], first observed the reentrance effect in  $R(T)$  in a Cu ring sample with two superconducting stripes. The reentrance was observed in  $R(T)$  when the measuring current was large enough to destroy the Josephson current coupling the superconductors [12]. Fig. 2.4.4 shows these data from the experiment of Ref. 12 with the sample schematic in the inset. The first resistance drop near  $T_c$  of the superconductor (Al) is due to the onset of the superconductivity. When a small measuring current is used the Josephson effect between the two superconductors causes another



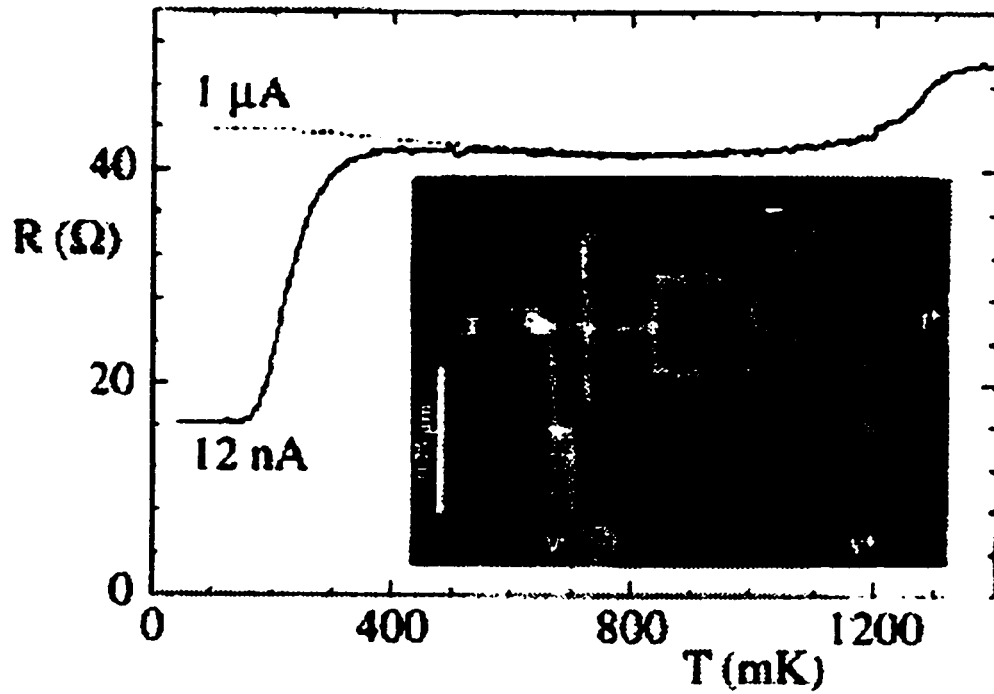


Fig. 2.4.4 Resistance as a function of temperature for the sample shown in the inset with four-probe measurement with  $I^+$  and  $V^+$  shown in the picture. The two vertical stripes on the two sides of the loop are superconductors. With a 12 nA ac probe current, the curve shows a second drop at 350 mK corresponding to the Josephson effect between two superconductors. With a higher probe current of 1  $\mu\text{A}$ , the Josephson effect disappears and the reentrance effect shows up instead. (From Courtois *et al.* Ref.[12]).

resistance drop followed by a plateau in resistance. This second resistance drop disappears when a larger measuring current is used and instead, a reentrance is observed as is shown by the dashed curve. By removing one of the superconducting stripes, Charlat *et al.* [13] were able to observe the reentrance effect in the resistance as a function of temperature for different multiples of the flux quantum  $h/2e$  threading the Cu ring. At about the same time, Petrashov *et al.* [14] also observed the reentrance effect in the amplitude of magnetoresistance oscillations of a piece of diffusive wire whose middle point is connected to a S loop via two N branches.

While all these experiments concentrate on the qualitative aspect of reentrance effect, a serious comparison of the theory with the experimental results is still lacking. Furthermore, the three measurements, i.e.,  $R(T)$ ,  $dV/dI(V)$  and the amplitude of magnetoresistance oscillations, that show a reentrance effect had not been observed in a single device. In chapter 5, we will discuss our observation of the reentrance effect in all three measurements in a single N-S device. A quantitative comparison of our results with the theory of quasiclassical Green functions will also be given.

## Chapter 3

### Sample fabrication and measurement

#### 3.1 Sample fabrication

Most of the samples discussed in this thesis were made by the author using electron beam (e-beam) lithography at Northwestern University. For the pure Al structures, single step e-beam lithography [89-91] was used, while for the NS structures more complicated two step e-beam lithography was used. Occasionally, photolithography [92] was used to pattern larger portions of the samples and the bonding pads. These last samples were mainly used in testing sample properties in the development of fabrication techniques since they allowed testing of many ideas in a short time. The real samples measured were all made by e-beam lithography for reasons which will be described in detail in later sections.

##### 3.1.1 E-beam lithography

The e-beam lithography facility at Northwestern University consists primarily of a JEOL<sup>1</sup> JXA-840 scanning electron microscope (SEM) which was converted to an e-beam writer. Fig. 3.1.1 shows a simple schematic of the setup of an e-beam writer. The desired pattern is generated via a raster program written at Northwestern University on an IBM PC. This pattern is transferred onto an oxidized Si wafer covered with PMMA (Polymethylmethacrylate) through a Digital-Analog Converter (DAC) card purchased from

---

<sup>1</sup>JEOL, Boston, MA

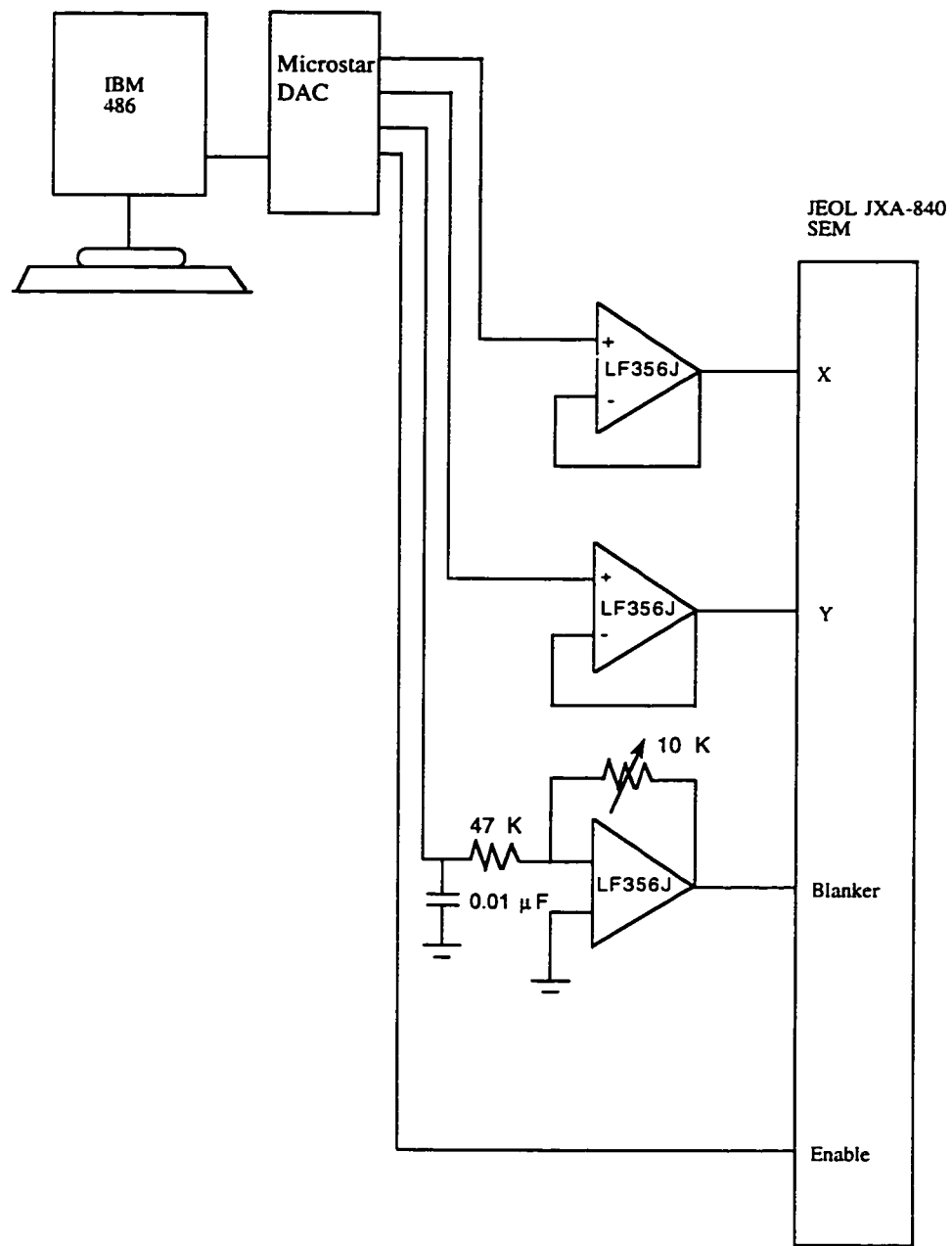


Fig. 3.1.1 Schematic of e-beam writer facility setup converted from JEOL-JXA840 SEM

Microstar.<sup>2</sup> The signals after the DAC card are buffered by a home-made circuit built by the author before entering the SEM and driving the electron beam (e-beam) in a raster pattern. The raster program also feeds beam blanking signals to a magnetic beam blanker inside the SEM column.

The beam current determines the actual dosage required to expose a pattern. It is read by sending the e-beam into a home-made Faraday cup [90] fixed on the corner of the sample stage in good electrical contact with the sample stage. A picoamp current meter is connected to the bottom of the sample stage to monitor the beam current. Usually, for our devices, a beam current of  $\sim 5\text{-}20$  pA is used, while for the large portions such as the contact pads a much larger beam current is used to save time. The main reason for using a small beam current for small structures is to avoid the well-known proximity effect caused by the high density of patterns [93].

After the sample is placed in the SEM column, the e-beam is first sent through a condenser lens, then driven by magnetic scanning coils before entering the objective apertures and lens to finally scan the sample surface. Four different aperture sizes can be chosen in our system. In order to obtain a small beam current to write fine structures, the smallest diameter of  $50\text{ }\mu\text{m}$  was chosen for the e-beam exposures. This allows one to write a pattern using a beam current as low as 4 pA. A built-in objective lens wobbler was used to center the objective lens aperture. The e-beam is focused on the surface of the Faraday cup by first changing the working distance between the objective lens and the sample surface. A stigmator further minimizes the aberrations. The focused beam is then sent into

---

<sup>2</sup>Microstar Laboratories, Inc. Bellevue, Washington.

Faraday cup to be monitored by the picoamp current meter. To align the beam, one has to adjust “GUN ALIGNMENT” knobs on the electronics panel for the correction of tilt and shift of the electron gun filament or crystal until the maximum beam current is read on the picoamp current meter. For a  $\text{LaB}_6$  filament,<sup>3</sup> the maximum current is  $\sim 200$  nA, while for a tungsten filament,<sup>1</sup> the maximum current is usually smaller by a factor of 4. After this, the e-beam is left in the Faraday cup until the filament is completely stabilized. Before the beam is stabilized the centering procedure for the electron beam described above has to be repeated several times. When an e-beam emitted from a stabilized filament is centered, adjusting the GUN ALIGNMENT knob should not change the maximal beam current by more than 10%. The time required for stabilization depends on the type of filament. For a  $\text{LaB}_6$  filament, it takes at least two hours after the filament is excited from its preheated state. For a tungsten filament, it takes about one hour after the filament is turned on.

The basic process of single step e-beam lithography is shown in Fig. 3.1.2. After the substrate is cleaned, a thin PMMA layer with a low molecular weight ( $\sim 150\text{K}$ ) is first spun onto the substrate using a spinner purchased from Headway Research, Inc.<sup>4</sup> at a speed which gives a thickness larger than the desired thickness of metal. The substrate is then baked at  $170^\circ\text{C}$  in an oven for one hour. After baking, the substrate is retrieved from the oven and cooled in air. A second PMMA layer with a higher molecular weight ( $\sim 500\text{K}$ ) is then spun on top of the first PMMA layer and baked at the same temperature for one hour. The substrate with the bilayer PMMA is then placed in the column of the SEM ready

---

<sup>3</sup>Purchased from FEI Co., Hillsboro, Oregon or Denka Co. Tokyo, Japan.

<sup>4</sup>Headway Research Inc., Garland, Texas

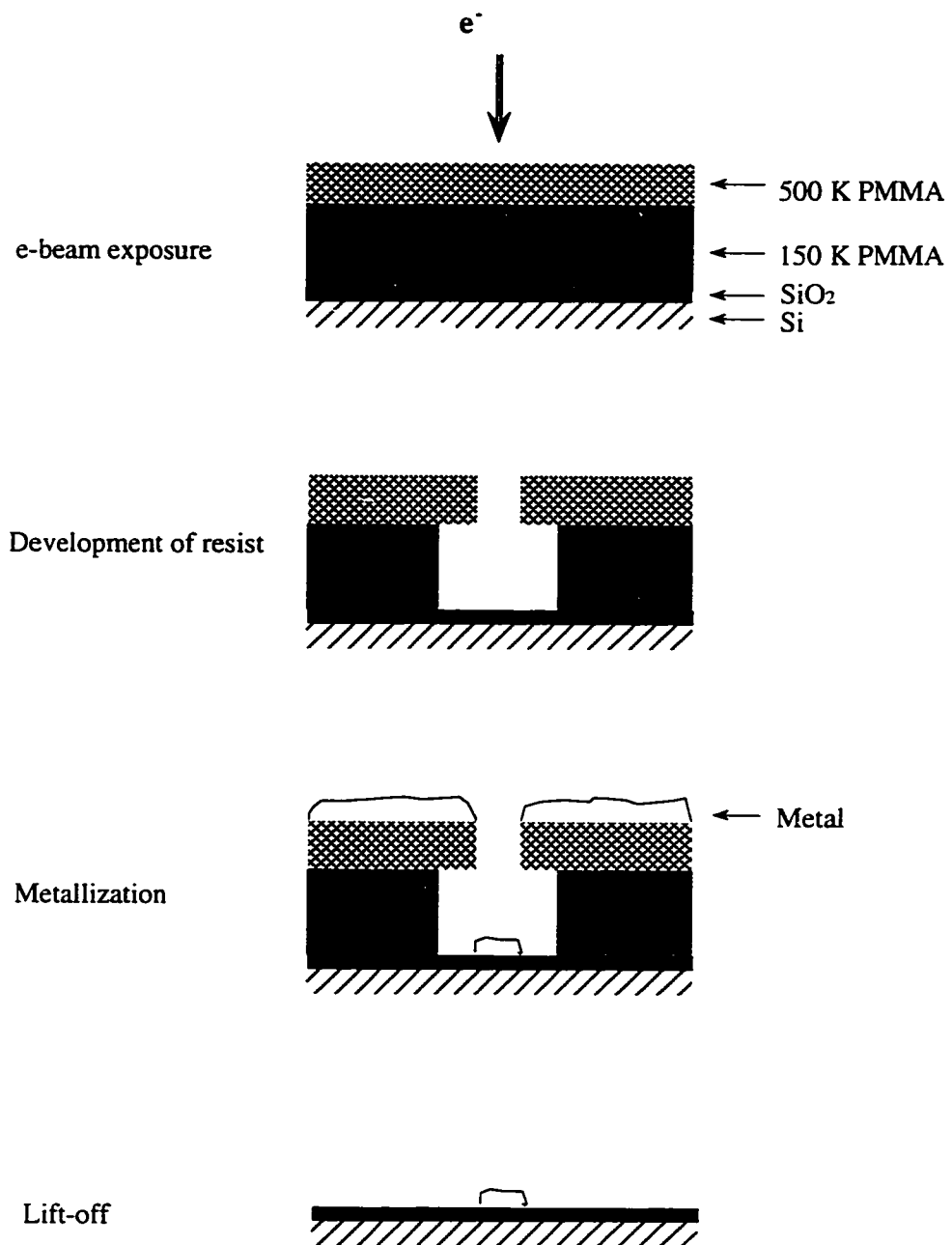


Fig. 3.1.2 Illustration of the basic principle of e-beam lithography.

for the e-beam exposure.

The desired pattern is transferred onto the wafer from a computer by driving the e-beam to expose the desired structure on the wafer. Since PMMA is a positive resist and the lower molecular weight is more sensitive to the e-beam, the exposure creates an undercut after development as shown in the second step of Fig. 3.1.2. The pattern is then metallized by evaporating the desired thin-film metal onto the wafer in a vacuum chamber at a pressure less than  $5 \times 10^{-6}$  Torr. After evaporation the wafer is removed from the vacuum chamber and the undesired portions of the metal on top of the remaining resist are lifted off.

In the fabrication of hybrid structures, a second step e-beam lithography is used after the first thin metal film is patterned. The procedure only differs in the temperature at which the substrate is baked and the baking time. This concern depends on the first metal patterned. Usually a normal metal film such as gold (Au) or silver (Ag) is chosen to serve as a normal metal in the proximity effect experiment. In our experience, the same baking temperature and time can be followed for the second step of lithography if Au is used for the first metal. However, if Ag is used, a lower temperature ( $\sim 95^{\circ}\text{C}$ ) and longer baking time ( $\sim 3$  hours) is chosen. The lower baking temperature avoids destroying the already patterned Ag film and the longer baking time helps dry the PMMA and avoids interlayer mixing. Table 3.1 summarizes the procedure of the fabrication process. In the following sections I describe the details for each step of the e-beam lithography process developed at Northwestern University to fabricate nano-structures.



Table 3.1  
Detail procedure of two-step e-beam lithography

- 
1. Spin 700Å 150K PMMA on a wafer. Bake the wafer at 170 °C for 1 hour in an oven.
  2. Spin 500Å 500K PMMA on the same wafer. Bake the wafer at 170 °C for 1 hour in an oven.
  3. Expose the wafer to e-beam with desired patterns.
  4. Develop the wafer in MIBK:IPA (1:3) for 45 seconds at 21 °C.
  5. Place the wafer in a vacuum chamber and pump down to  $3 \times 10^{-7}$  Torr. Preevaporate the metal for 50Å with the shutter closed. Pump down the chamber to  $3 \times 10^{-7}$  Torr again. Etch the wafer with an *in situ* dc  $O_2^-$  or  $Ar^+$  plasma at 1.5 kV, 40 mtorr for 30 seconds.
  6. Pump down the chamber to  $3 \times 10^{-7}$  torr and evaporate the desired metal.
  7. Remove the wafer from the vacuum chamber and soak it in acetone for 1 hour.
  8. Lift off the resist by shooting the metal surface with acetone.
  9. Clean the wafer and repeat step 1 to 8 except step 5 replaced by step 10.
  10. Place the wafer in a vacuum chamber and pump down to  $3 \times 10^{-7}$  Torr. Preevaporate the metal for 50Å with the shutter closed. Pump down the chamber to  $3 \times 10^{-7}$  Torr. Etch the wafer with an *in situ* dc  $Ar^+$  plasma at 1.0 kV, 40 millitorr for 30 seconds. Pump down the chamber to  $3 \times 10^{-7}$  Torr again.
-

### 3.1.1.1 Substrates and cleaning

Doped silicon wafers, since they are conducting at room temperature, prevent electrostatic damage of devices by shorting them. An additional oxidation on top of the wafer provides an insulating layer at room temperature and allows one to check for the continuity of the devices [90]. Another great concern is charge accumulation during dc plasma etching [94]. For all these reasons, a thin oxidation layer should be chosen. Alternatively, one can pattern a grounding loop for the devices before etching and disconnect them just before testing.

The Si wafer is cleaned with acetone and then isopropyl alcohol. Since acetone vaporizes quickly, isopropyl alcohol helps keep the surface wet before the wafer is dried by blowing with high purity nitrogen gas. Most of the dirt on the wafer surface will be taken away by the acetone and isopropyl alcohol.

### 3.1.1.2 Oxidation of wafer

Oxidation is one of the key process in modern semiconducting integrated circuit (IC) fabrication. The utilities of silicon dioxide include: it acts as a component of the MOS structure, it isolates one level of metal from another, and it serves as a mask against the diffusion of dopant into silicon [95]. Extreme care must be taken in handling wafers to prevent possible contamination. One should always handle the clean dry wafers with special gloves and tweezers. For our purpose a thin layer of  $\text{SiO}_2$  of  $\sim 0.07 - 1 \mu\text{m}$  thickness was grown on a Si wafer by thermal oxidation in a quartz tube with dry  $\text{O}_2$  flowing through. For the aluminum structures prepared by one-step e-beam lithography, oxidation layers of thickness  $\sim 700\text{\AA}$  were grown on bare Si wafers purchased from

Virginia Semiconductor, Inc.<sup>5</sup> using the chart shown in Fig. 3.1.3 [96]. After oxidation, the SiO<sub>2</sub> on the back of wafer was etched away by buffer-HF for 5 minutes to ensure good electrical contacts with the sample holder. Before etching, a thin resist layer was spun on the front surface of the wafer to protect the oxidation layer. For the hybrid structures, Si wafers with an oxide layer ~ 0.5 - 1 μm thick were directly purchased from Polishing Corp. of America.<sup>6</sup>

### 3.1.1.3 Resist

PMMA serves as the resist for patterning the masks in e-beam lithography. The resist was purchased from Microlithography Chemical Corp.<sup>7</sup> For the fabrication of plain Al wires PMMA of 150K and 500K molecular weights were used in single step e-beam lithography. The lower molecular weight resist is more sensitive to e-beam exposure and thus can create an undercut for clean lift-off. The PMMA was dissolved in MIBK (methyl-isobutyl-ketone) to create a solution of 2-3 % by weight. This is achieved by mixing the PMMA with the proper amount of MIBK in a quartz bottle placed on a hotplate maintained at a temperature less than 80<sup>0</sup>C, since PMMA is flammable [90]. The mixture in the bottle was constantly stirred by a magnetic bar to accelerate the dissolution. Different solvents can be chosen for particular purposes. A weaker solvent such as xylene has been tested for the purpose of preventing interlayer mixing [90, 91]. In order to dissolve

---

<sup>5</sup>Virginia Semiconductor Inc., Ronoke, Virginia

<sup>6</sup>Polishing Corp. Of America, Santa Clara, CA.

<sup>7</sup>Microlithography Chemical Corp. Newton, MA.

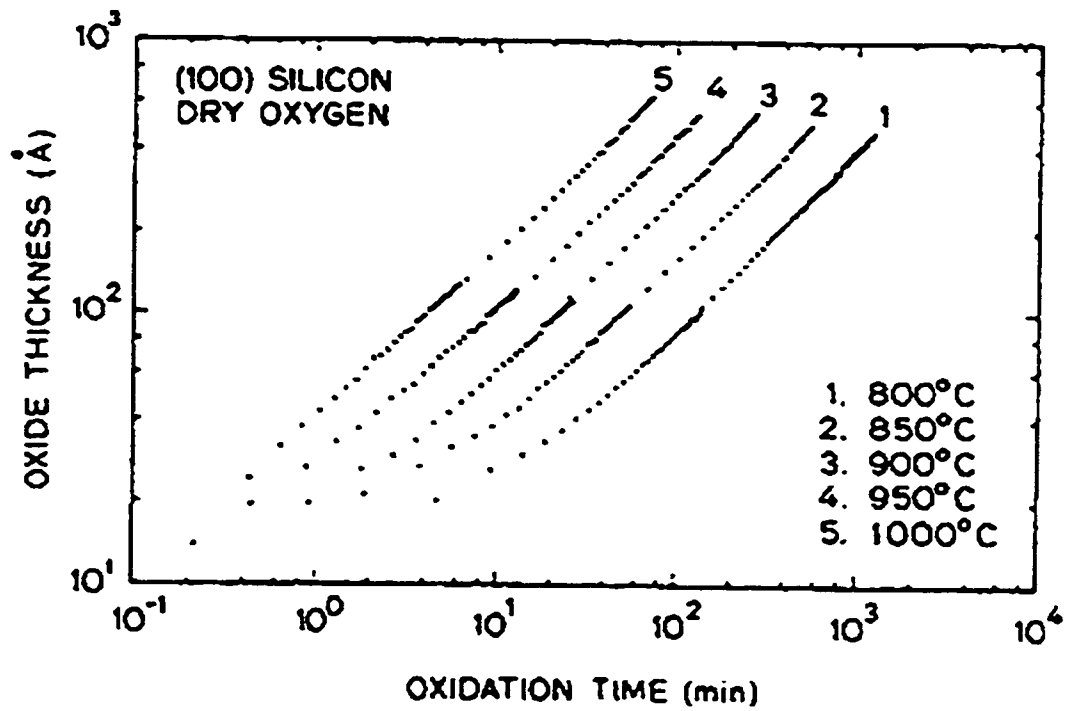


Fig. 3.1.3 Thermal oxide thickness grown on a <100> Si wafer as a function of time at different temperatures. (From Massoud *et al.* Ref. [96]).

PMMA in xylene, one needs to keep stirring for over 48 hours. Completely dissolved resist looks transparent and contains no PMMA particles in the solvent. Resist of good quality is crucial for successful devices, since undissolved resist usually gives a nonuniform thin resist layer and causes irreproducible results. Great care should be taken in storing the resist since any dirt in the resist would cause defects in the devices. A resist thus prepared gives a thin layer of few thousand angstroms at a spinning speed of few thousand rpm. Fig. 3.1.4 is an example of two spin curves for two different molecular weights. A PMMA of lower molecular weight gives a thinner layer at the same spinning speed as a higher molecular weight.

The general procedure for spinning the resist is as follows: The wafer is first cleaned by the procedure in Sec. 3.1.2.1. It is very important to keep the substrate dry before spinning the resist. After cleaning, the substrate is immediately placed on the spinner. To ensure a clean surface one can clean the wafer by blowing the substrate surface with clean and dry nitrogen gas while spinning the substrate for few seconds. When the spinner stops the resist is dropped onto the surface of the substrate and the substrate is spun immediately. It is very important to cover the whole substrate with resist in order to obtain a uniform coating. Furthermore, PMMA dries quickly. Therefore one should always start spinning the substrate as soon as the whole substrate is covered with resist.

#### 3.1.1.4. Exposure and development

Devices were usually patterned within a  $10\text{ }\mu\text{m} \times 10\text{ }\mu\text{m}$  exposure field (See Fig. 3.1.5 (a)). With a  $700\text{\AA}/500\text{\AA}$  bilayer PMMA resist, a dosage ranging from 600 to  $900\text{ }\mu\text{C}/\text{cm}^2$

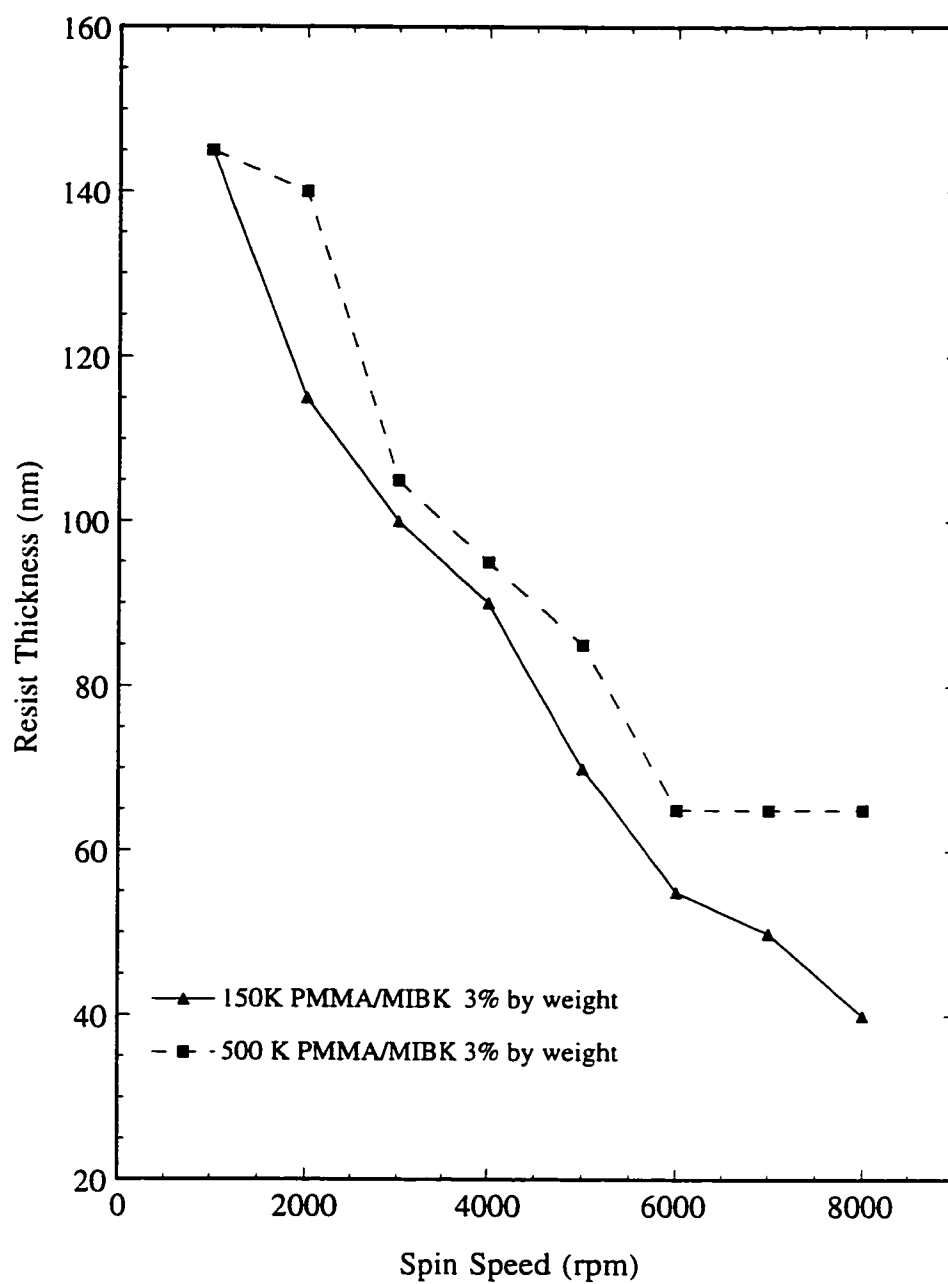


Fig. 3.1.4 The spin curves for PMMA of two different molecular weights. The PMMA is Dupont 2010, Microlithography Chemical Corp.

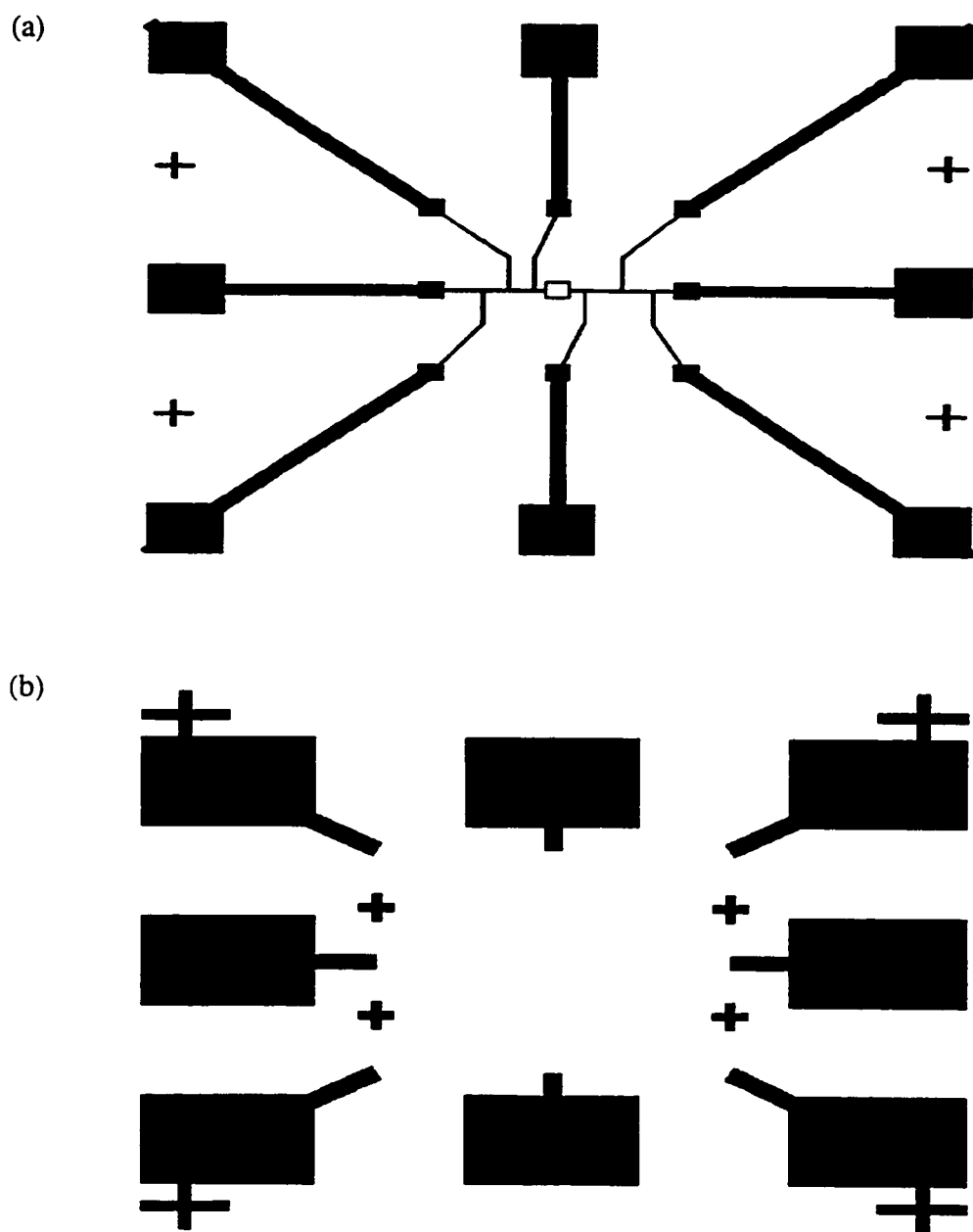


Fig. 3.1.5 Examples of lithography patterns. (a) Small sample pattern for e-beam lithography inside a  $10\ \mu\text{m} \times 10\ \mu\text{m}$  exposure field. (b) Large contact pads pattern for photolithography. Also shown are the alignment marks (crosses).

was used. Using a low beam current  $\sim 5$  pA it takes less than 1.8 seconds to write a  $10\text{ }\mu\text{m}$  long,  $0.1\text{ }\mu\text{m}$  wide line, so it takes less than 45 seconds to finish a single level exposure for a sample containing 16 leads. However, it takes 9 seconds to finish a single bonding pad of dimensions  $200\text{ }\mu\text{m} \times 150\text{ }\mu\text{m}$ , large enough to allow several tries for successful wire bonding. Therefore, it usually takes more than 4 minutes to finish a complete pattern taking into account other factors such as focusing, alignment, etc, for a skilled operator. This is obviously not a good choice from the business point of view. Still, e-beam lithography has its own advantages, such as flexibility of patterning masks and capability of producing a finer linewidth compared with photolithography. The solution for the above problem is to pattern the large structures outside the exposure field of the actual device by using photolithography. Fig. 3.1.5(b) shows an example of such a pattern. After the pattern is metallized, the procedure in Table 3.1 is followed to pattern the real devices. A major concern in this procedure is to keep good electrical contacts between two patterns generated from two different processes. The general way to solve this problem is to keep the film thickness of the outside patterns less than that of real devices. However, decreasing the thickness of the bonding pads can also lead to difficulty in wire bonding. To overcome this, one can increase the area of each contact. For this reason the e-beam exposure field is sometimes extended until the minimal safe contact area is satisfied.

Focusing the electron beam and mutual alignment of different lithography layers are two other critical issues which needs to be addressed to produce fine and reliable multilevel devices. A PMMA layer by itself does not provide any contrast on which to focus. The multilevel alignment marks shown in Fig. 3.1.5 are created to solve these problems. By focusing and aligning on these alignment marks, one can place the fine



pattern within the layer contact patterns with an accuracy better than 100 nm. Fig. 3.1.6 shows one of the devices made using this technique. An alternative focusing method for creating very fine lines is to “burn” a small hole in the resist by using the “spot” mode in the SEM. Since it is at the same level as the top of the resist in the exposure field, focusing on the spot can produce even more accurate results. One can also check the astigmatism of the beam by examining the roundness of the spot at high magnification. This technique takes advantage of the clear contrast which occurs when PMMA is cross linked when it is overexposed by the electron beam.

After exposure the wafer is developed in a developer made of MIBK mixed with Isopropyl alcohol in the ratio 1:3 by weight for 45 seconds at 21 °C. The residual developer is then blown away immediately with dry nitrogen.

#### 3.1.1.5 Metallization

Metals of high purity 99.999 % for the devices were purchased from ESPI<sup>8</sup> or Alfa.<sup>9</sup> They were deposited on the wafer in an Edwards<sup>10</sup> vacuum evaporator at a pressure less than  $5 \times 10^{-6}$  Torr. The pressure was monitored by a cold cathode gauge. The metal was thermally evaporated on a tungsten boat from R. D. Mathis<sup>11</sup> and the film thickness was

---

<sup>8</sup>Electronic Space Products International, Ashland, Oregon.

<sup>9</sup>Alfa Products, Denver, MA.

<sup>10</sup>Edwards, Wilmington, MA

<sup>11</sup>R. D. Mathis Co., Long Beach, CA.

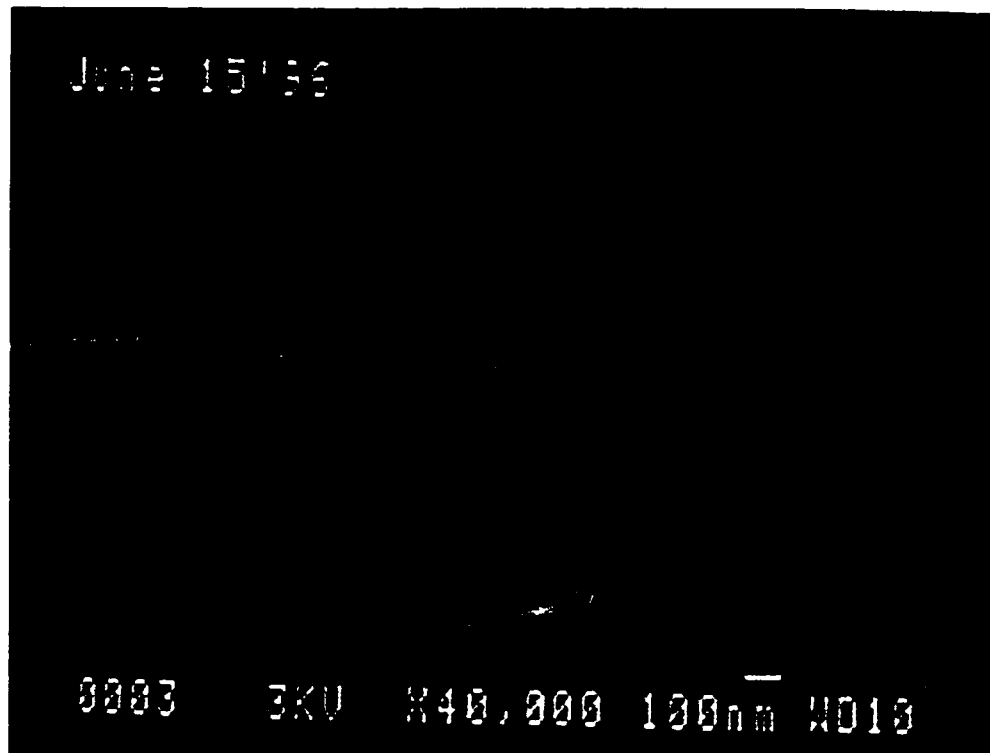


Fig. 3.1.6 An example of a NS device patterned by e-beam lithography. The lighter lines are Au (N) and the darker lines are Al (S).

monitored with an Au coated crystal sensor from Sycon Instruments, Inc.<sup>12</sup> To obtain a clean metal film with larger grain sizes a high deposition rate is preferred so that the deposition can be finished in a short time before the pressure rises.

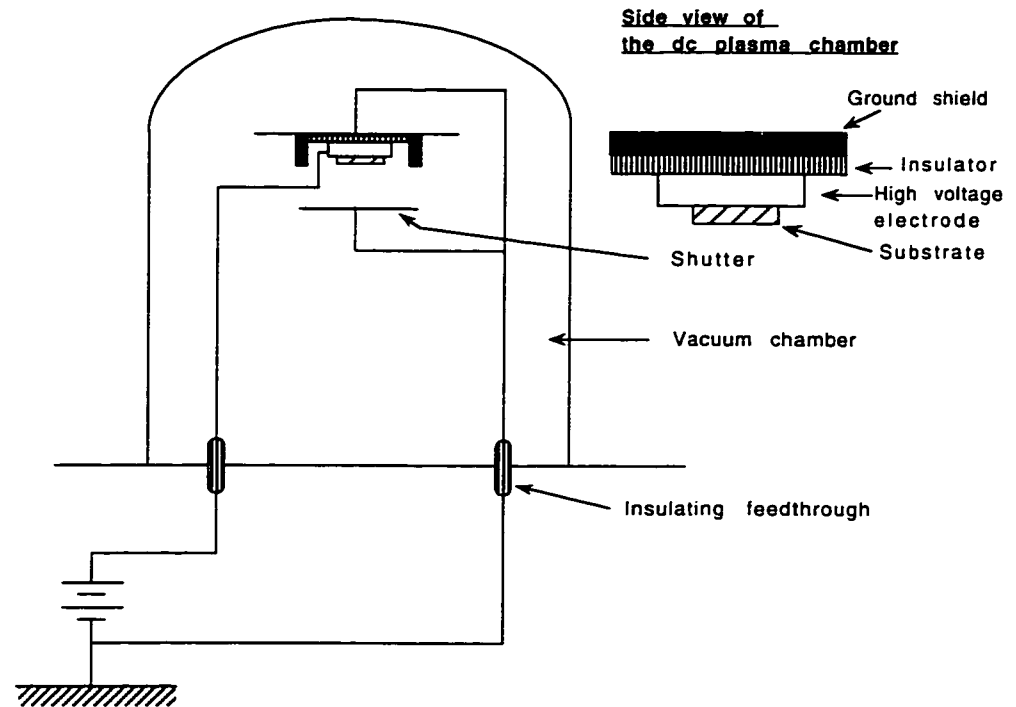
#### 3.1.1.6 Etching

The key problem in the fabrication of N-S hybrid devices is in achieving a good N-S interface. This is overcome by cleaning the normal metal surface with dc plasma prior to the deposition of superconducting film. A schematic of the *in situ* etching setup is shown in Fig. 3.1.7(a). The plasma is generated by applying a high voltage dc bias between the sample plate and the shutter. The high dc voltage is supplied by a high voltage ac transformer through a bridge rectifier whose schematic is shown in Fig. 3.1.7(b). The pressure is monitored by a TC gauge directly connected to the chamber through a feedthrough. Different gases can be introduced into the vacuum chamber for different purposes. An O<sub>2</sub> plasma was used to clean the samples after development prior to evaporation. Since the oxygen ions clean the substrate through chemical reaction with the resist, lighter damage to the metal film results. Technically, it is better than etching by argon ions, where the cleaning process is mainly via particle bombardment. The possible disadvantage for O<sub>2</sub> plasma is it may cause oxide residue in the undercut after cleaning. This is a more critical problem in the two-step lithography process, where in our experiments aluminum, which oxidizes easily, serves as the second metal. Consequently, for the charge imbalance experiments, O<sub>2</sub> was selected as the gas for plasma etching, while in proximity experiments Ar was selected. The substrate is attached to an electrode which

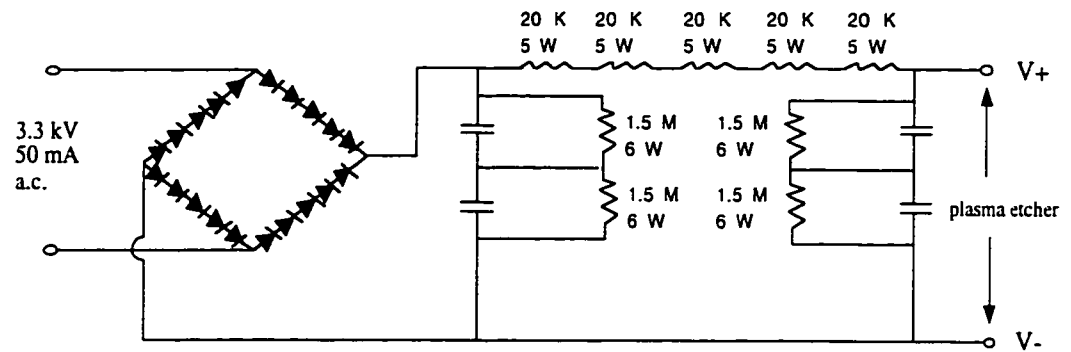
---


<sup>12</sup>Sycon Instrument, Inc., East Syracuse, New York.

(a)



(b)



 2  $\mu$ F / 2.5 kV D.C.

 1N4007

Fig. 3.1.7 Schematic of the dc plasma etching setup. (a) Electrodes and substrate setup. (b) A circuit for the high power rectifier.

is biased at a positive voltage to the shutter for O<sub>2</sub> gas and at a negative voltage to the shutter for the Ar gas.

Gas pressure, etching time, etching power are some of major factors which influence the etch. It is, of course, a tricky process when hybrid structures are needed since it is usually not easy to control the property of an interface of area less than  $10^{-2} \mu\text{m}^2$ . Furthermore, a thin film of thickness  $\sim 10^2 \text{ \AA}$  is easily damaged by etching. It is good to keep most of the etching parameters constant while only varying one or two parameters to obtain the most reproducible process. For the reentrance experiments, the only parameter varied was the etching time. Before the etching process the metal was preevaporated to get rid of possible contamination of the metal surface. Dry Ar gas was then introduced and kept at 40 mTorr by controlling the pumping rate of the diffusion pump and the gas flow rate through a needle valve at the same time. A high voltage of 1.2 kV is then applied between two electrodes. Charge accumulation is an important problem in dc plasma cleaning. The nano device can be easily blown out by a high power dc plasma. Fig. 3.1.8 shows an example of a failed etching process. A device is usually blown from the interface area if the etching power or time is too strong. A simple solution to this problem is to first etch the sample for 30 seconds and then pump down the chamber to base pressure. This repumping process takes less than 10 minutes in our system. The sample is then etched for another 30 seconds after which chamber is pumped down to base pressure before the deposition. The detailed etching process can be found in Ref. 94.

#### 3.1.1.7 Lift-off

After metallization the sample is soaked in acetone for more than one hour. The undesired

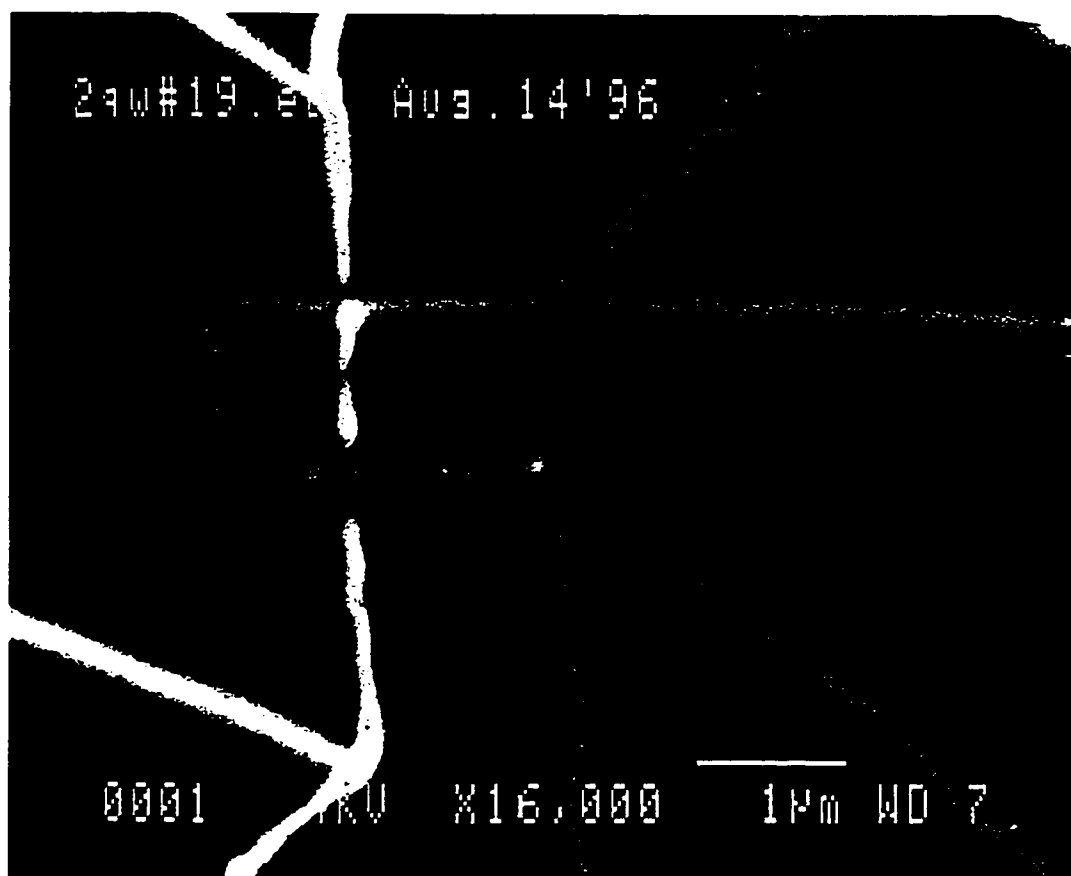


Fig. 3.1.8 A scanning electron micrograph showing the damage due to a strong dc plasma in a NS nano device. The sample is usually blown from the NS interfaces.

part of the metal film is then washed away by shooting the sample surface with acetone. It is important to avoid drying the sample surface before lift-off is complete. Alternatively, one can place the substrate in a beaker filled with acetone and ultrasonically cleaning the substrate. Since this process is very destructive, one should be very careful not to over-clean the substrates.

### 3.2 Measurement

Fig. 3.2.1 shows the schematic of the measurement setup. The setup is composed of three parts, i.e., the refrigerator, measuring electronics and data recording. All the electrical lines are connected to the room temperature electronics from the refrigerator through two terminal boxes which can ground all electrical lines and separate the measurement electronics from the refrigerator. In the dilution refrigerator, these electrical lines are composed of CuNi wires above the mixing chamber and copper wires between the mixing chamber and the sample mounting block in order to provide strong thermal link between the sample and the mixing chamber. For the  $\text{He}^4$  cryostat and  $\text{He}^3$  refrigerator, CuNi wires were used from room temperature down to the  $\text{He}^4$  or  $\text{He}^3$  pot. The sample was mounted on a variable sample block attached to the pot by a weak thermal link. The wires were purchased from Supercon, Inc.<sup>13</sup> The two boxes also have high frequency  $\pi$ -filters with a cut-off frequency of 10 MHz through which the excitation signals enter the samples and the response is detected by the electronics. These filters prevent possible radio-frequency noise coupling down to the fridge from the environment.

---

<sup>13</sup>Supercon, Inc., Shrewsbury, MA

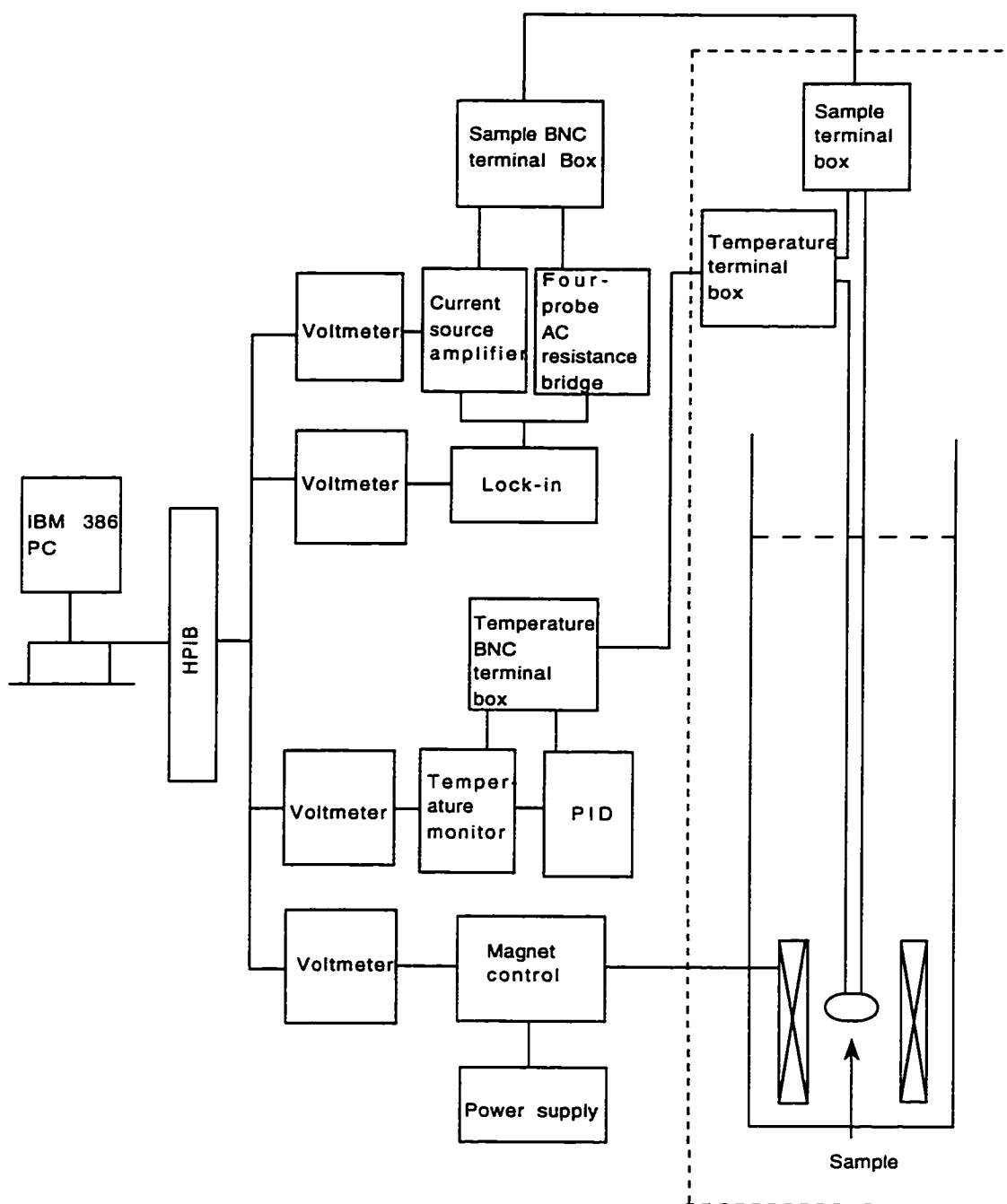


Fig. 3.2.1 Schematic of the measurement setup.



### 3.2.1 Sample handling and testing

All samples were wire bonded with a Kulicke & Soffa<sup>14</sup> Model 4123 wedge bonder. 0.001" AlSi(1%) wires were used for all bonding. Extreme care should be taken in handling the nano devices as they are very sensitive to static charge. The hybrid devices, when patterned after lift-off, are very delicate. The resistance of the interface could change dramatically in few hours when exposed in air. For this reason, all the samples were kept in a liquid nitrogen storage dewar right after lift-off. Exposure to air was minimized before cooling in the fridge. This is especially critical for Ag, which tarnishes in air very rapidly.

### 3.2.2 Low temperature cooling facilities

The basic principle of cooling uses the unique property of the two isotopes of helium -  $\text{He}^3$  and  $\text{He}^4$ . A  $\text{He}^3/\text{He}^4$  mixture separates into two phases below a critical temperature (tricritical point) of 0.86K, one rich in  $\text{He}^3$  (concentrated phase), the other rich in  $\text{He}^4$  (dilute phase). The unique properties of the two phases are : First, the  $\text{He}^3$  can travel through  $\text{He}^4$  without interacting with it at all. Second, there is still some  $\text{He}^3$  concentration left even at zero temperature. Therefore it is possible to obtain a very low temperature by pumping the  $\text{He}^3$  out of the mixture below the tricritical point. Detailed discussion of low temperature techniques using liquid helium can be found in Refs. [97-100].

Three major cryostats were operated in these measurements. An Oxford<sup>15</sup>

---

<sup>14</sup>Kulicke & Soffa Industries, Inc., Horsham, PA

<sup>15</sup>Oxford Instruments, Oxford, England

Kelvinox 300 dilution fridge was used to cool the samples down to 30 mK to study the proximity effect. The temperature was monitored by a home-made thermometer built by J. Eom at Northwestern University [110]. It has an ac excitation as low as 5 nA to avoid possible heating of the resistor. The temperature was controlled by a PID (Proportional - Integral - Differential) temperature controller built by the author. This PID allows control of the temperature to within 1 mK. Fig. 3.2.2 shows the circuit of the PID. It was modified from the PID circuit in Ref. 101.

The second cryostat was purchased from Janis Research Company, Inc.<sup>16</sup> It cools the samples by pumping  $\text{He}^3$  in a closed system and is useful for measurements in the temperature range between 4 K and 270 mK. The operation of this cryostat is as follows. The  $\text{He}^3$  gas is first absorbed by a charcoal pump and then condensed into a  $\text{He}^3$  pot by heating the charcoal pump. During this process the 1K pot is maintained at a temperature less than 1.4 K by pumping liquid  $\text{He}^4$  through an adjustable impedance line to the  $\text{He}^4$  recovery system. When all the  $\text{He}^3$  is condensed the temperature reaches about 1.5 K. The  $\text{He}^3$  pot is then further cooled to 270 mK by pumping the liquid  $\text{He}^3$  out of the pot while maintaining the 1K pot below 1.4 K. This is achieved by cooling the charcoal pump with  $\text{He}$  from the bath. The cooling rate of the charcoal pump is controlled by a capillary with  $\text{He}^4$  flowing from the bath through to the air. The  $\text{He}^4$  flow rate is controlled and monitored by a flow meter before being vented into the air. The whole procedure, when in a hurry, takes less than 3 hours to cool from room temperature to base temperature and the holding time is over 48 hours. Therefore it is an economical facility with great

---

<sup>16</sup>Janis Research Company, Inc., Wilmington, MA.

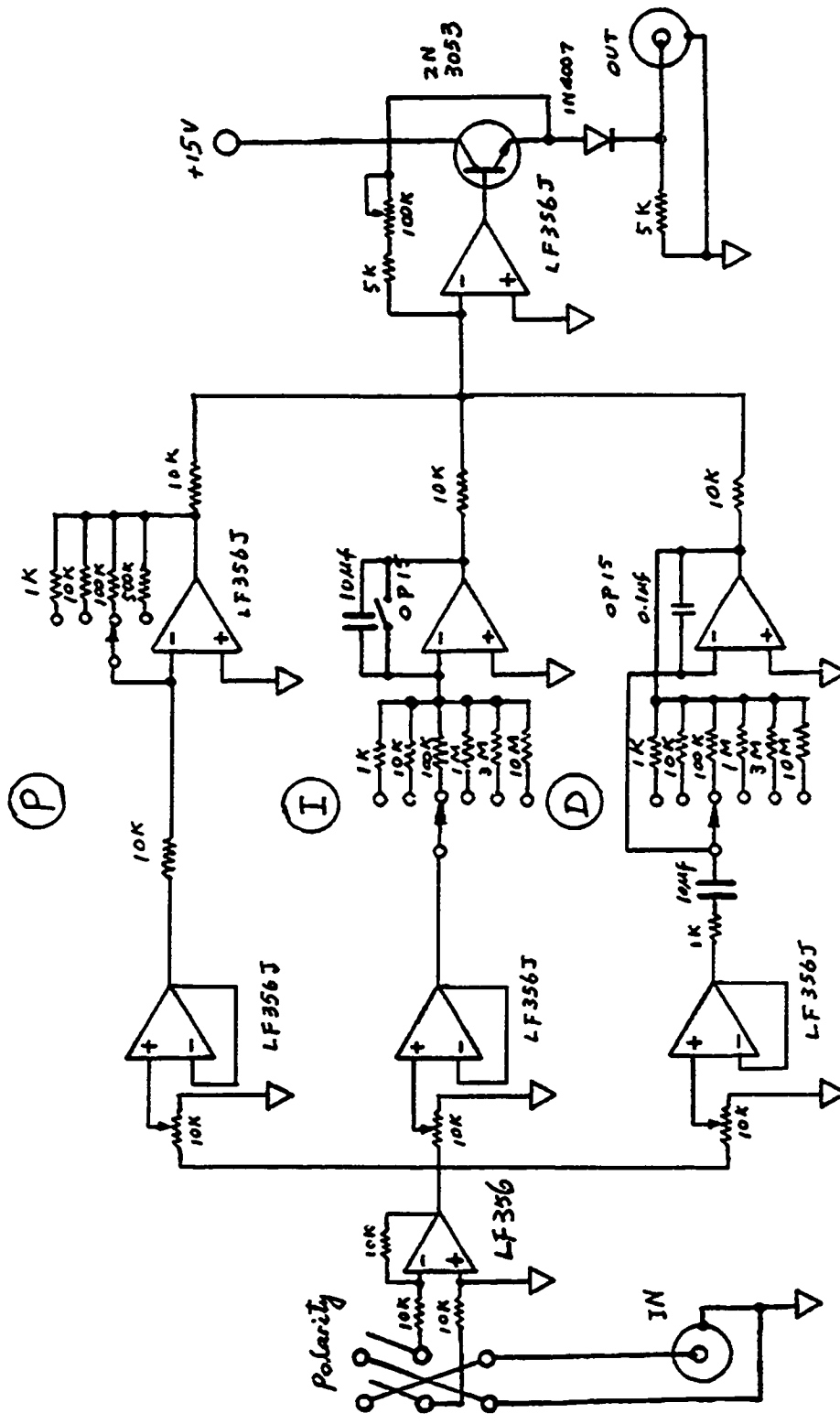


Fig 3.2.2 A P-I-D circuit

performance. When the experiment is finished the cryostat is warmed up by simply heating the charcoal pump or  $\text{He}^3$  pot and dumping all the  $\text{He}^3$  gas back to the storage tank on top of the cryostat.

Temperatures at both the charcoal pump and the 1K pot are monitored by an attached silicon diode thermometer whose I-V characteristics were provided by Janis, Inc. These temperatures are read by a simple current source whose circuit is part of Fig. 3.2.3 designed by the author and built by M. Z. Lin at Northwestern University. The samples are wire bonded and connected to the  $\text{He}^3$  pot through the same procedure mentioned above. A Matshushita resistor provided by Janis, Inc and a  $\text{RuO}_2$  resistor attached to the sample block are used to read the temperature of the samples. They are also monitored and controlled by the same home-made electronics mentioned above through part of the circuit in Fig. 3.2.3. This circuit also provides the power for heating the sample block,  $\text{He}^3$  pot and charcoal.

The last cryostat is a  $\text{He}^4$  cryostat. It was built at Northwestern University by J. Eom. The sample is simply connected to a 1K pot and cooled by pumping liquid  $\text{He}^4$  out of the pot through a fixed impedance line to the  $\text{He}^4$  recovery system.

### 3.2.3 Measuring electronics

Since most of the samples measured had resistances less than  $100\ \Omega$ , an ac lock-in technique combined with a high impedance current source was used to perform the measurement. The home-made electronics were built or modified by J. Eom at

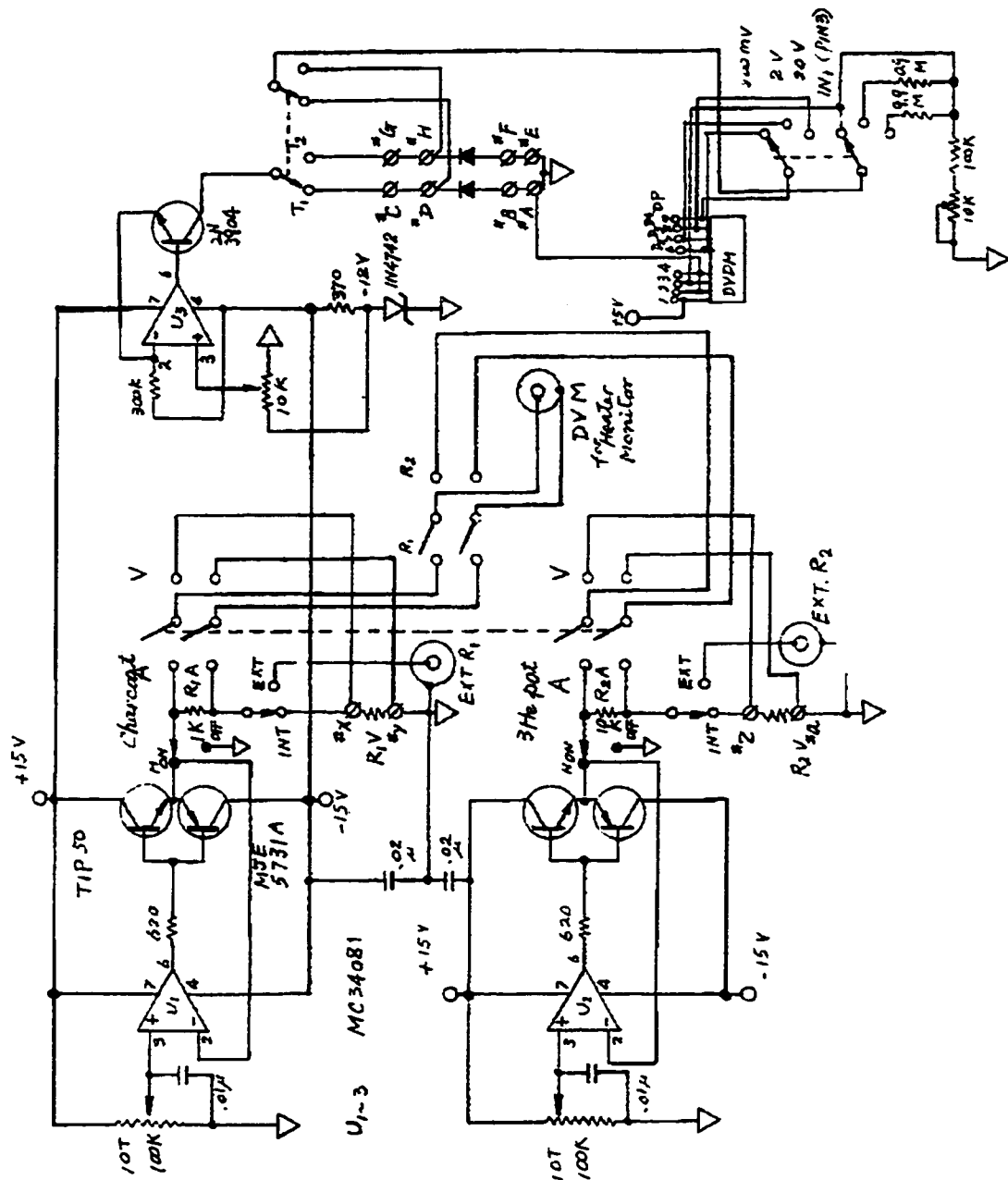


Fig. 3.2.3 Schematic of the circuit of the temperature controller for the  $\text{He}^3$  cryostat.

Northwestern University. Fig. 3.2.4 shows some of the major electronic circuits.

*Ac resistance measurement of the sample*

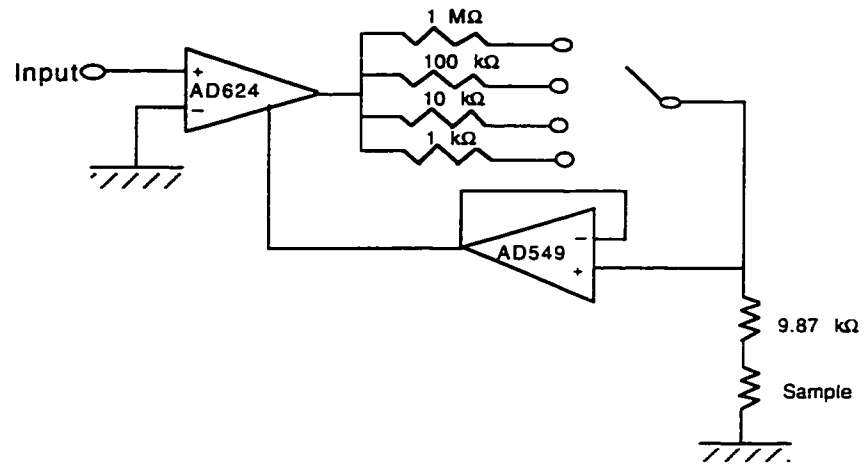
The ac resistance can be measured directly using a lock-in amplifier and current source, or using a four-point bridge circuit (Fig. 3.2.4(b))[90, 101-102]. For the measurement setup using Fig. 3.2.4(a), the ac current is supplied by applying a low frequency (10~100 Hz) voltage to the input of the circuit from an EG&G PAR124 or 124A lock-in amplifier.<sup>17</sup> The frequencies used were selected to avoid possible coupling from 60 Hz noise. The high precision, low noise instrumentation amplifier AD624 purchased from Analog Devices<sup>18</sup> has an high input impedance  $\sim 10^9 \Omega$ . Combined with low input bias current operational amplifier AD549 ( input impedance  $\sim 10^{13} \Omega$ ), the circuit in Fig. 3.2.4(a) provides a high output impedance voltage to current converter with a constant current proportional to the input voltage. Before the measurement is carried out, the circuit is phased by minimizing the out-of-phase component of the response. The constant excitation current is then measured by reading the voltage across a 9.87 k $\Omega$  resistor in series with the sample current leads using a lock-in amplifier. After the desired current is measured, the input of the lock-in amplifier is switched to detect the voltage across the sample by connecting the input of the lock-in amplifier to the voltage leads of the sample. To use the circuit of Fig. 3.2.4(b), the four leads of the sample are directly connected to the four wires as shown in the figure.

---

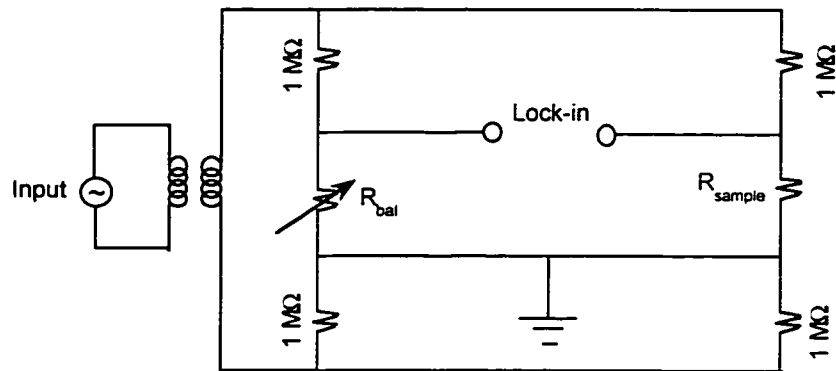
<sup>17</sup>EG&G Princeton Applied Research, Princeton, NJ

<sup>18</sup>Analog Devices, Norwood, MA

(a)



(b)



(c)

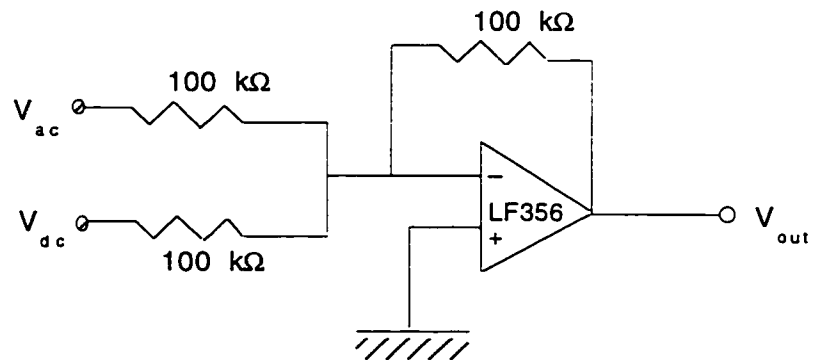


Fig. 3.2.4 Circuits for transport measurements. (a) Voltage-current converter. (b) ac four-probe resistance balance bridge. (c) voltage summer.

The 1432-W decade resistor from General Radio USA<sup>20</sup> has a precision of  $10^{-2} \Omega$  and a high stability. Therefore it provides a reliable way of measuring mesoscopic samples. This decade resistor is balanced with the sample resistance before the measurement. The circuit is then phased by changing the phase offset until the out-of-phase component of the response is unchanged as one varies the decade resistor. The ac excitation is measured by reading the ratio of the voltage change on the lock-in amplifier to the change of the decade resistance. After the ac excitation is calibrated the decade resistance is switched back to the balance value. During the measurement, any change of the sample resistance is read directly from the voltage change on the lock-in amplifier divided by the ac excitation. One of the advantages of using the resistance bridge is its high sensitivity and stability.

#### *Differential resistance measurement*

To measure the differential resistance  $dV/dI$ , an additional dc signal is summed with the ac signal via a summing amplifier (LF356)(Fig. 3.2.4(c)) before the total excitation enters the current source. The dc current is supplied from the output voltage of a HP3325A<sup>21</sup> synthesizer at a low frequency of  $\sim 10^2$ - $10^3$   $\mu\text{Hz}$ . This voltage is converted to dc current through the voltage to current converter (Fig. 3.2.4(a)) and is monitored by reading the dc voltage of the  $9.87 \text{ k}\Omega$  resistor with HP34401A<sup>22</sup> voltmeters through an AD624 amplifier used as a buffer. The differential resistance is then obtained by detecting the ac signal with

---

<sup>20</sup>General Radio Co., Concord, MA.

<sup>21</sup>Hewlett Packard, Santa Clara, CA.

<sup>22</sup>Hewlett Packard, Palo Alto, CA.



a lock-in amplifier. The resistors of various values following the AD624 in the circuit of Fig. 3.2.4(a) allow one to adjust the dc current in various ranges. For our measurements on the 1D Al lines, the critical current is less than 200  $\mu\text{A}$  which can be easily achieved by adjusting the maximal output of 3325A or the resistance value in Fig. 3.2.4(a). One can also place the dc current source in parallel with the decade resistance bridge to perform the  $dV/dI$  measurement.

### *Magnetoresistance measurement*

The low magnetic fields needed in the experiments were obtained from superconducting magnets. The magnetic field was swept by controlling the current through the magnet using a bipolar KEPCO-1M or 20M<sup>23</sup> power supply in voltage mode. The sweep signal was provided by a HP3325A<sup>20</sup> or a DS345 synthesizer.<sup>24</sup> The current was sent through a home-made low field box, in which a 1  $\Omega$ /10W wirewound shunt resistor is connected in series with the superconducting magnet in the refrigerator. The magnetic fields in the experiments of this thesis are less than 1000 gauss, which is larger than the critical field of thin aluminum films (~600-800 gauss). This requires only a maximum current less than 1 ampere applied into our magnet according to the current-field conversion ratio for the 14 Tesla magnet attached to the dilution refrigerator or the 6 Tesla magnet for the He<sup>3</sup> or He<sup>4</sup> inserts. This low current does not change the value of the shunt resistor significantly. The magnetic field can be monitored by reading the voltage of the shunt resistor with

---

<sup>23</sup>KEPCO, Inc. Flushing, NY.

<sup>24</sup>Stanford Research Systems, Sunnyvale, CA.

HP34401A<sup>21</sup> voltmeters through an AD624 amplifier.

Finally, all the measured data were recorded by a program on IBM PCs, written by J. Eom at Northwestern University through GPIB interfaces.<sup>24</sup> One should always be extremely careful in handling and testing mesoscopic samples since any electrostatic shock can destroy the samples. Furthermore, noise problems are important in the transport measurement of mesoscopic samples since the response signals are usually small. The measurement setup should always minimize ground loops in order to avoid picking up noise signals from the environment. On measuring samples, it is important to avoid heating the samples. Examples of these concerns are given in the following paragraph as the final remarks of this chapter.

For the sample heating problems, consider the example of a  $100\ \Omega$  sample. Using a typical ac current of 100 nA rms, the power generated from Joule heating is  $\sim 1$  picowatt. Whether this amount of power results in appreciable heating of the samples depends on the manner in which heat is lost to the environment. Typically, by coupling to the bath, one usually checks for heating self consistently by performing the measurement several times using steadily smaller ac excitations until the measurement does not change as a function of the ac excitation. As for the noise problem, without shielding, the typical 60 Hz noise in our measurements is  $\sim 200\ \text{nV} / \sqrt{\text{Hz}}$ . With proper shielding of the electrical lines and minimizing the grounding loops, this noise can be cut down to less than  $5\ \text{nV} / \sqrt{\text{Hz}}$ , which is much smaller than the signal.

---

<sup>24</sup>National Instruments, Austin, TX.

## **Chapter 4**

### **Resistance anomaly in mesoscopic superconducting wires**

This chapter is divided into three parts. The first two parts, which are described in sections 4.1 and 4.2 respectively, deal with measurements of the so-called resistance anomaly in mesoscopic superconducting wires. In section 4.1, we discuss the results of measurements on the role of radio frequency (rf) in inducing the resistance anomaly in narrow 1D Al wires. In section 4.2, we show that mixing a low frequency signal with the measuring signal also gives rise to a resistance anomaly. A comparison between the two methods of inducing the resistance anomaly is given in section 4.3 and confirms the intrinsic origin of rf induced resistance anomaly described in section 4.1. This work on the resistance anomaly was performed in close collaboration with Professor Chris van Haesendonck's group at the Katholieke Universiteit in Leuven, Belgium. The last part of the chapter is included in sections 4.4 and 4.5 which present measurements of mesoscopic devices containing NS interfaces in the charge imbalance regime. The author is indebted to C. Strunk of Katholieke Universiteit Leuven and B. Burk of Northwestern University who had done the primary work in sections 4.1 and 4.2 respectively.

#### **4.1 Resistance anomalies in pure Al structures induced by rf signals**

To our knowledge, the resistance anomaly in narrow one dimensional (1D) superconducting wires was first observed by Santhanam *et al.* [1]. The physics

responsible for this phenomenon is thought to be charge imbalance near a phase-slip center (PSC) in the sample (see Chapter 2). This PSC-induced charge imbalance had been observed in an earlier experiment by Dolan and Jackel [27], where a PSC was induced in the sample by means of a notch. The fact that there is no clear evidence for a PSC or a NS interface in the sample of Santhanam *et al.* has motivated more investigations on similar systems. Soon after Santhanam *et al.*, Vloeberghs *et al.* [2] observed anomalous Little-Parks oscillations [2] in a 1D Al wire containing a square loop and explained these anomalous oscillations in terms of the physics of charge imbalance. In a recent experiment by Park *et al.* [5], the nonlocal nature of the PSC was further demonstrated in a 2D Al sample.

In this section, we discuss our experiments on the resistance anomaly [6, 9]. After a description of the samples in our experiments, we show that the resistance anomaly can be induced in 1D Al samples by applying rf radiation or a magnetic field. This is manifested in the transport measurements,  $R(T)$  and the I-V characteristic. The properties related to charge imbalance are discussed in the data.

#### 4.1.1 Sample properties and measurement setup

We have measured two types of samples. One type is a pure 1D Al line with multiple voltage probes. This type of sample allowed us to investigate the spatial dependence of the resistance anomaly induced by rf radiation. The second type of sample is a 1D Al line containing a loop. This type of sample allowed us to investigate how a magnetic field affected the resistance anomaly. The loop sample and all the measurements presented here were made at the Katholieke Universiteit, Leuven.

Fig. 4.1.1(a) shows an AFM micrograph of the Al loop sample (which we shall denote Al Loop). The loop size is  $1\text{ }\mu\text{m} \times 1\text{ }\mu\text{m}$ . When a perpendicular magnetic field is applied, one expects a periodic suppression of the order parameter in the loop at temperatures near  $T_c$  due to classic Little-Parks effect [103]. The order parameter in the loop is suppressed when  $T_c$  is suppressed. Consequently, it is most likely to induce a phase slip center inside the loop when its  $T_c$  is suppressed by the magnetic field [1, 5, 6, 9, 27]. Two Al line samples are discussed in this chapter (which we shall denote Line#1 and Line#2). The AFM micrograph of Line#1 is shown in Fig. 4.1.1(b) and the SEM picture of Line#2 is shown in Fig. 4.1.1(c). The properties and dimensions of all three samples are list in Table. 4.1. In view of the experiment of Dolan and Jackel [27], where a phase-slip center was nucleated preferentially at one point by means of an artificial notch, it is relevant to check whether there are any defects in the topology of our samples which may act as preferential nucleation sites for PSCs. SEM and AFM pictures show that there is no apparent defect in the film. Fig. 4.1.2 shows a detail of part of sample Line#1 along with its height profile, confirming the smoothness of the thin film. The width of the sample is larger than the variation of the film thickness and grain size by at least a factor of 5. Consequently, it is unlikely that the grain structure would lead to the experimental results discussed in this chapter. The relevant characteristic length  $\xi(T)$  is estimated using the Ginsburg-Landau formula in the dirty limit [18]:

$$\xi(T) = 0.855 \frac{\xi_0 l}{\sqrt{1 - \frac{T}{T_c}}} \quad (4.1.1)$$

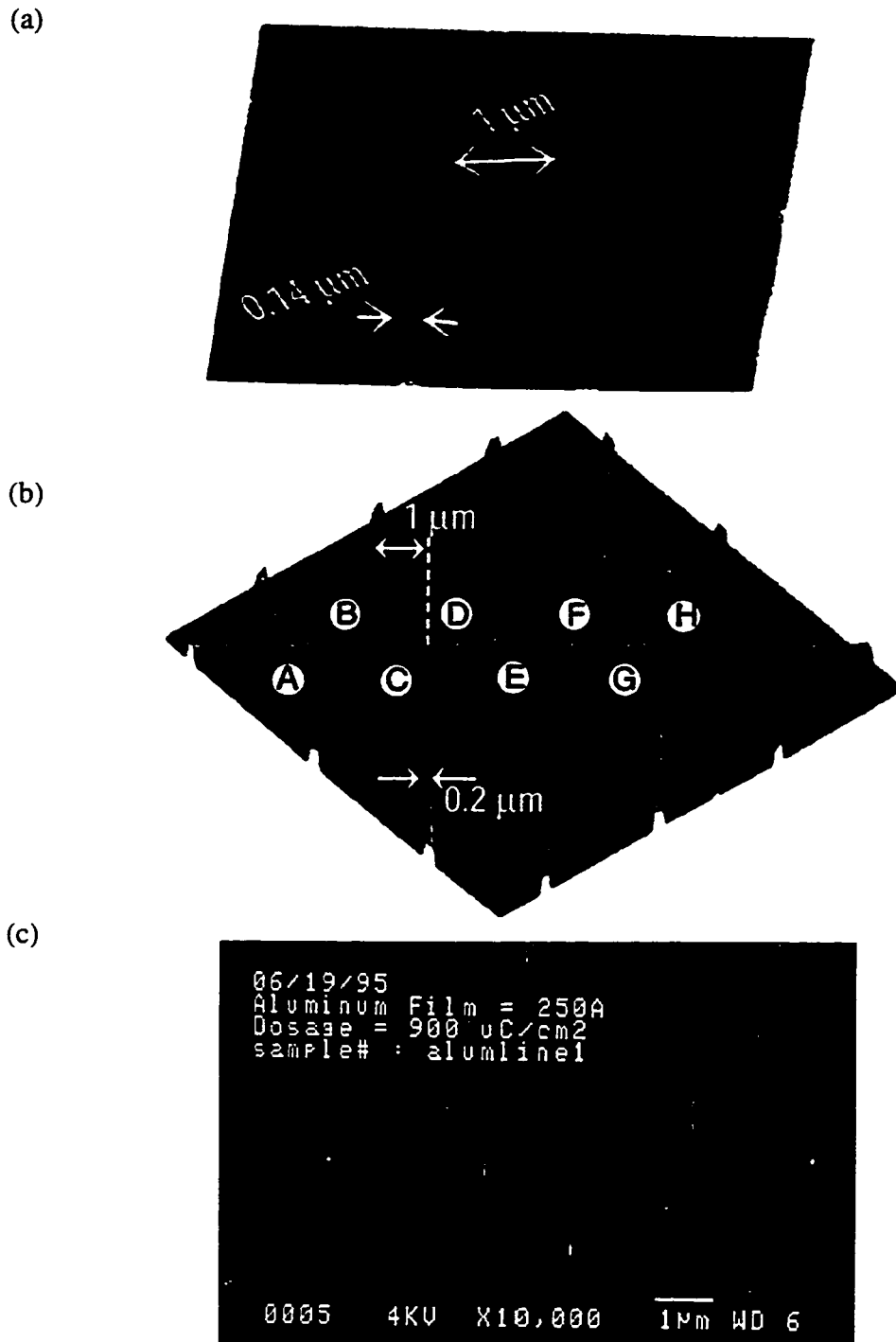


Fig. 4.1.1 AFM micrograph of (a) Al loop structure and (b) Al Line#1 structure. (c) SEM micrograph of Al Line#2 structure. ((a) and (b) from C. Strunk *et al.* Ref. [9]).

Sample	t(nm)	w(nm)	$R_N(\Omega)$	$\rho(\mu\Omega\text{cm})$	$D(\text{cm}^2/\text{sec})$	$T_{c0}(\text{K})$	$\xi_{\text{GL}}(\mu\text{m})$
Loop	43	140	$8.4(V_1-V_2)5.5(V_1-V_3)$	2.3	70	1.294	0.14
Line#1	30	200	6.4 (Segment B)	3.8	48	1.372	0.13
Line#2	25	200	2.3 ( $R_{18,45}$ )	2.4	72	1.324	0.14

Table. 4.1 Material parameters for the measured samples. Identical parameters for all samples are:  $\rho l_{\text{el}} = 4 \times 10^{-16} \Omega\text{m}^2$  (see Ref. [104]),  $v_F = 1.3 \times 10^6 \text{ m/s}$ ,  $\xi_{\text{GL}} = 0.86(\xi_0 l_{\text{el}})^{1/2}$ , and  $\xi_0 = 1.6 \mu\text{m}$ . (Adapted from C. Strunk *et al.* Ref.[9]).

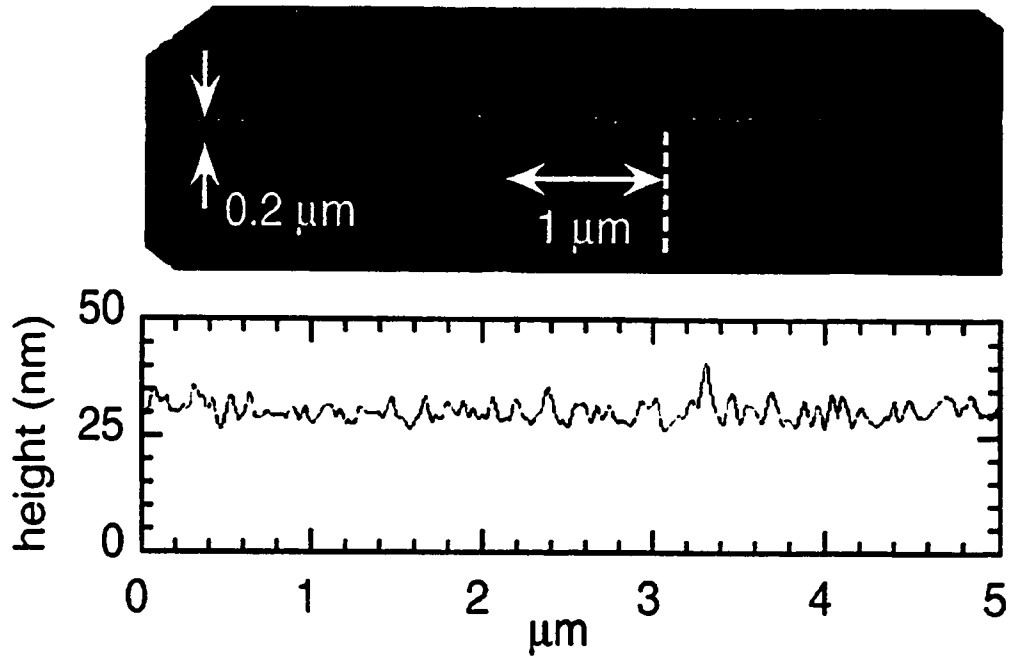


Fig. 4.1.2 Detail of Fig. 4.1.1(c) with the segment B (see Fig.4.1.3(c)) showing the anomaly and its two neighboring segments A and C. Also shown below is the height profile along the center of the wire for the same part of the sample. (From C. Strunk *et al.* Ref.[9]).

where  $l$  is calculated from a given result for the product  $\rho l = 4 \times 10^{-16} \Omega\text{m}^2$  [104],  $\rho$  being the resistivity of the film,  $\xi_0$  is Pippard coherence length [18].

The measurements were performed in a  $\text{He}^3$  fridge. Details of the ac resistance measurement techniques have been described in Chapter 2. The frequency used here is 27 Hz. For the I-V curves, a HP34420A dc nanovoltmeter was used to measure the I-V characteristic directly. The RF signal was supplied to the sample with two coaxial cables in a separate tube and capacitively coupled to the current leads. (see Fig. 4.1.3(a)). All electric lines were shielded by  $\pi$ -filters with a cut-off frequency of 1 MHz. Due to the resistance change of the sample at the superconducting transition, the actual rf power injected into the sample is difficult to determine. Furthermore, some of the rf power may be lost in the electrical lines and the capacitors. However, by interchanging the two current leads we can check the experimental result is independent of the injection point. The normal-superconducting phase boundary,  $T_c(\text{B})$  was measured by tracing the sample at the midpoint of the resistive transition while slowly ramping the magnetic field.

In order to remain consistent in our discussion of the data, we present the results on the loop structure since it shows additional effects when a magnetic field is applied perpendicular to the loop.

#### 4.1.2 Resistance anomaly in $R(T)$

Fig. 4.1.4(a) shows the superconducting transition for the line segment between voltage leads  $V_1$  and  $V_3$  of the Al Loop sample (see Fig. 4.1.3(a)) for various amplitudes of an



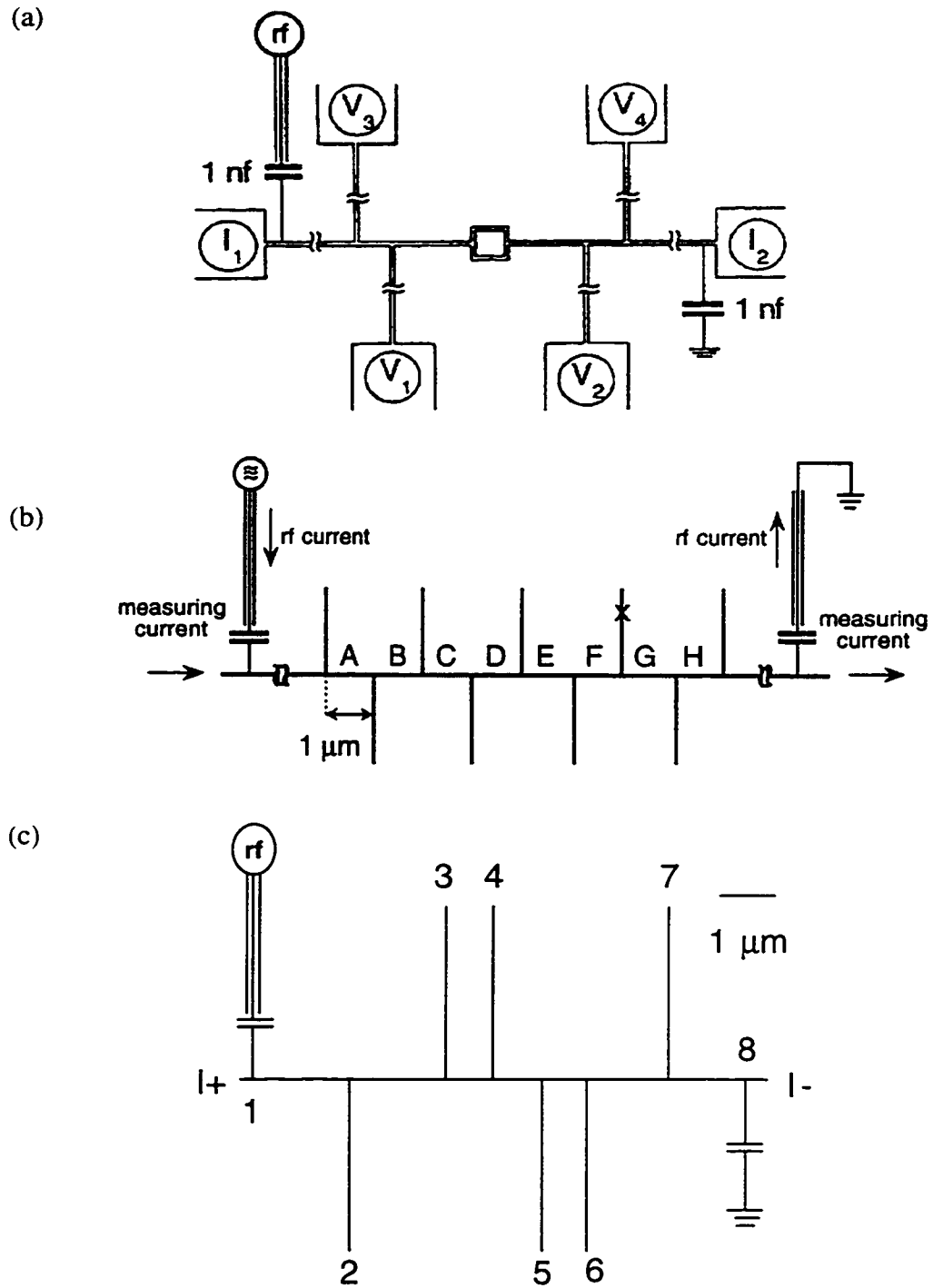


Fig. 4.1.3 Schematic of the lead configuration for applying a rf signal (a) for the Al Loop structure (b) for Al Line#1 structure and (c) for Al Line#2 structure. (Adapted from C. Strunk et al. [6, 9] and B. Burk et al. [8]).

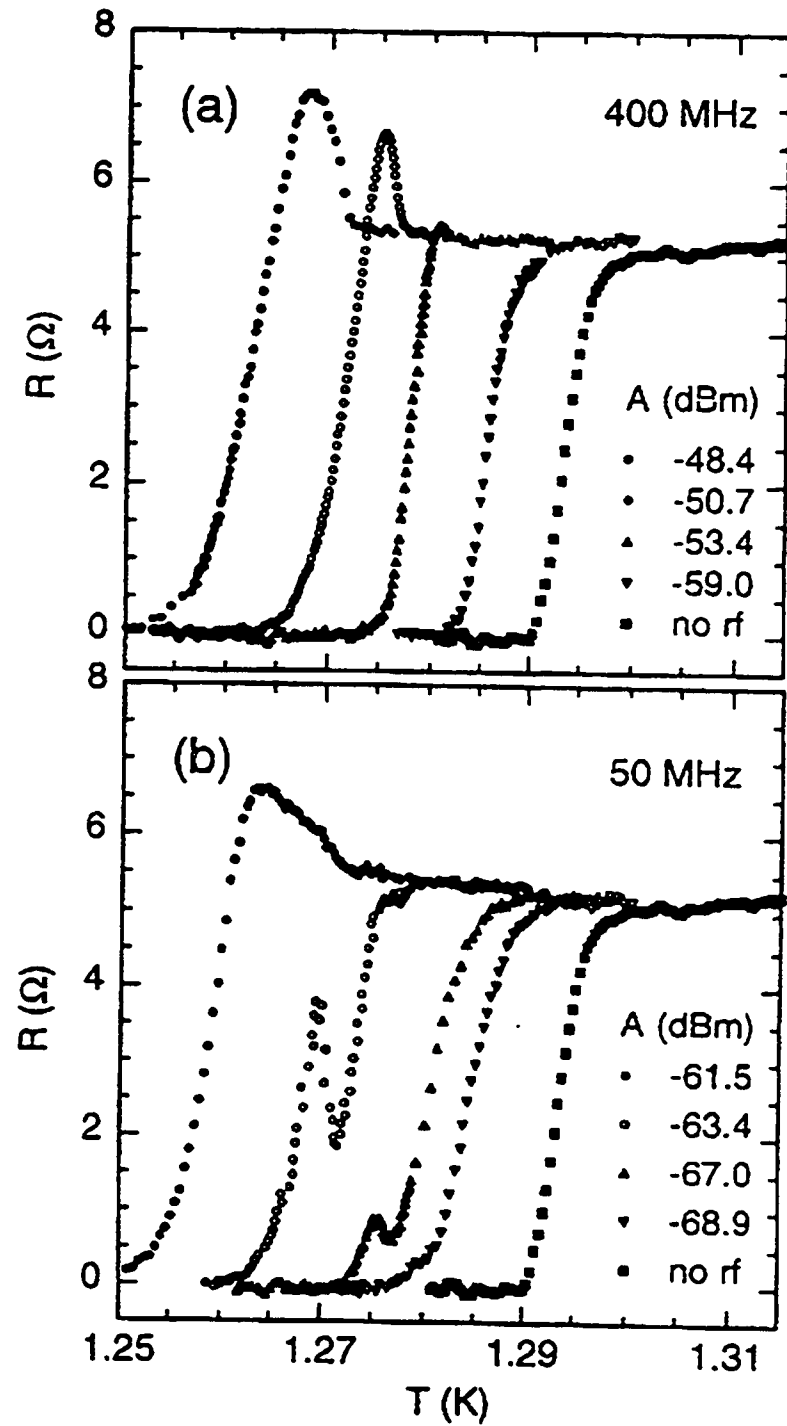


Fig. 4.1.4  $R(T)$  curves of the Al Loop sample measured with voltage probes  $V_1/V_3$  (see Fig. 4.1.3) for an applied rf signal of different amplitudes and frequency (a) 400 MHz (b) 50 MHz. (From Strunk, *et al.* Ref. [6]).

applied rf signal of 400 MHz. With this choice of voltage leads, the part of the sample measured does not contain the loop, but only a straight wire segment. Without any applied rf signal, the curve shows the usual superconducting transition with  $T_{c0} \sim 1.294$  K, where  $T_{c0}$  is measured at the midpoint of the transition with no magnetic field applied. With a rf signal applied,  $T_{c0}$  is first suppressed due to Joule heating or pair breaking. By increasing the rf power, a clear resistance anomaly is induced in the trace for -48.8 dB and -50.7 dB, similar to that observed by Santhanam *et al.* [1]. Fig. 4.1.4(b) shows similar data for a frequency of 50 MHz. In this sample, one observes a peak appearing below the apparent transition temperature, which evolves into the usual resistance anomaly at higher rf powers. These effects do not depend on thermal cycling of the sample.

The fact that the resistance anomaly appears below  $T_{c0}$  but above the bottom of transition indicates that it is associated with a nonequilibrium superconducting state. While there is no apparent NS boundary in the sample, one can think of a PSC as a dynamic NS boundary based on the model of charge imbalance near a PSC as discussed in Chapter 2. An important property of charge imbalance is that the quasiparticle chemical potential  $\mu_q$  varies over a characteristic length  $\Lambda_Q^*$ , while the pair chemical potential  $\mu_p$  remains almost constant (see Chapter 2). Therefore the voltage leads (which are superconducting) can measure an excess voltage as compared to normal leads. Within this picture, one expects the resistance anomaly to disappear as the separation between the two voltage probes is increased [1-9]. To verify this, we measured over different voltage probes of the same sample in order to check the spatial dependence of the excess voltage. Fig. 4.1.5 shows the normalized  $R(T)$  curves using different combination of the voltage probes with a 400

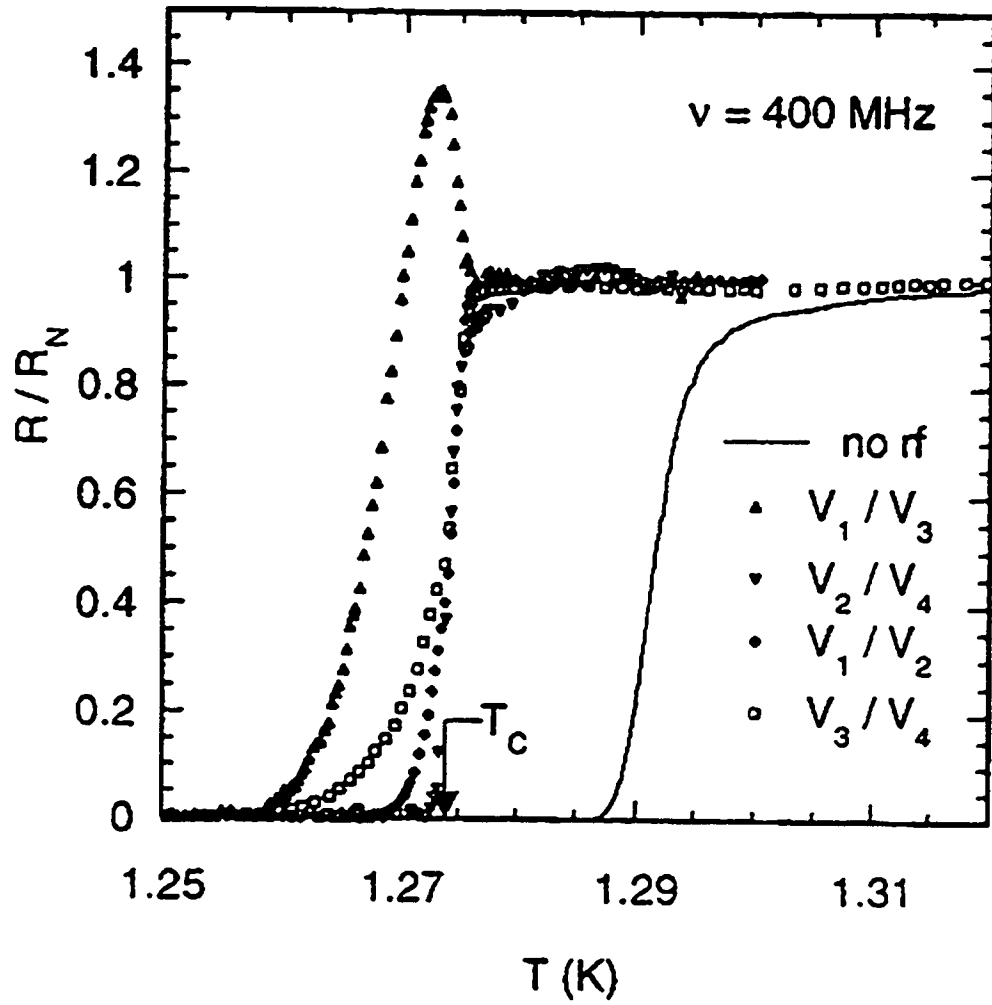


Fig. 4.1.5 Normalized  $R(T)$  curves for an applied rf signal of 400 MHz, -50 dB measured across different segments of the sample. A clear RA shows up across segment  $V_1/V_3$  only. Note that the depression of  $T_c$  is the same for all segments and the RA in segment  $V_1/V_3$  indeed rises below  $T_c$ . For comparison, the solid line shows  $R(T)$  for segment  $V_3/V_4$  without rf radiation. (From Strunk *et al.* Ref. [6]).

MHz, -50 dB signal applied. The resistance anomaly can be induced only in the short segment between leads  $V_1$  and  $V_3$ . Other segments, while they experience the rf signal (as can be seen in the decrease of  $T_{c0}$ ), do not show any resistance peak. In contrast to segment  $V_1/V_3$ , the longer segment  $V_3/V_4$ , which includes the segment  $V_1/V_3$  does not show any resistance anomaly, which is in agreement with the charge imbalance model. Although segment  $V_2/V_4$  has the same dimensions as that of segment  $V_1/V_3$ , the  $R(T)$  curve corresponding to this segment does not show any resistance anomaly. This is probably due to the monotonic decrease of rf power from the injecting lead along the sample as mentioned in section 4.1.1, although  $T_c$  of this segment is clearly suppressed. Alternatively, one can consider the segment  $V_1/V_3$  to have a point of locally suppressed superconductivity, which acts as a favored point for the nucleation of a PSC. The detailed mechanism responsible for the different effects of rf radiation on  $T_c$  and resistance anomaly is not clear. The data of Fig. 4.1.5 again confirms that the resistance anomaly is induced in the superconducting state.

#### 4.1.3 Resistance anomaly in $V(I)$

The excess voltage stemming from probing different chemical potentials in the same sample as described in the previous section can be further investigated in the I-V curves of the sample. By measuring the I-V curves of the same segment  $V_1/V_3$  with a rf signal of the same amplitude and frequency at various temperatures, a maximal excess voltage in the curve is observed at a temperature (1.273 K) corresponding to the resistance maximum observed in  $R(T)$  (see Fig. 4.1.5). This is shown in Fig. 4.1.6. This maximum excess voltage decreases as the temperature moves away from 1.273 K. The inset of Fig. 4.1.6

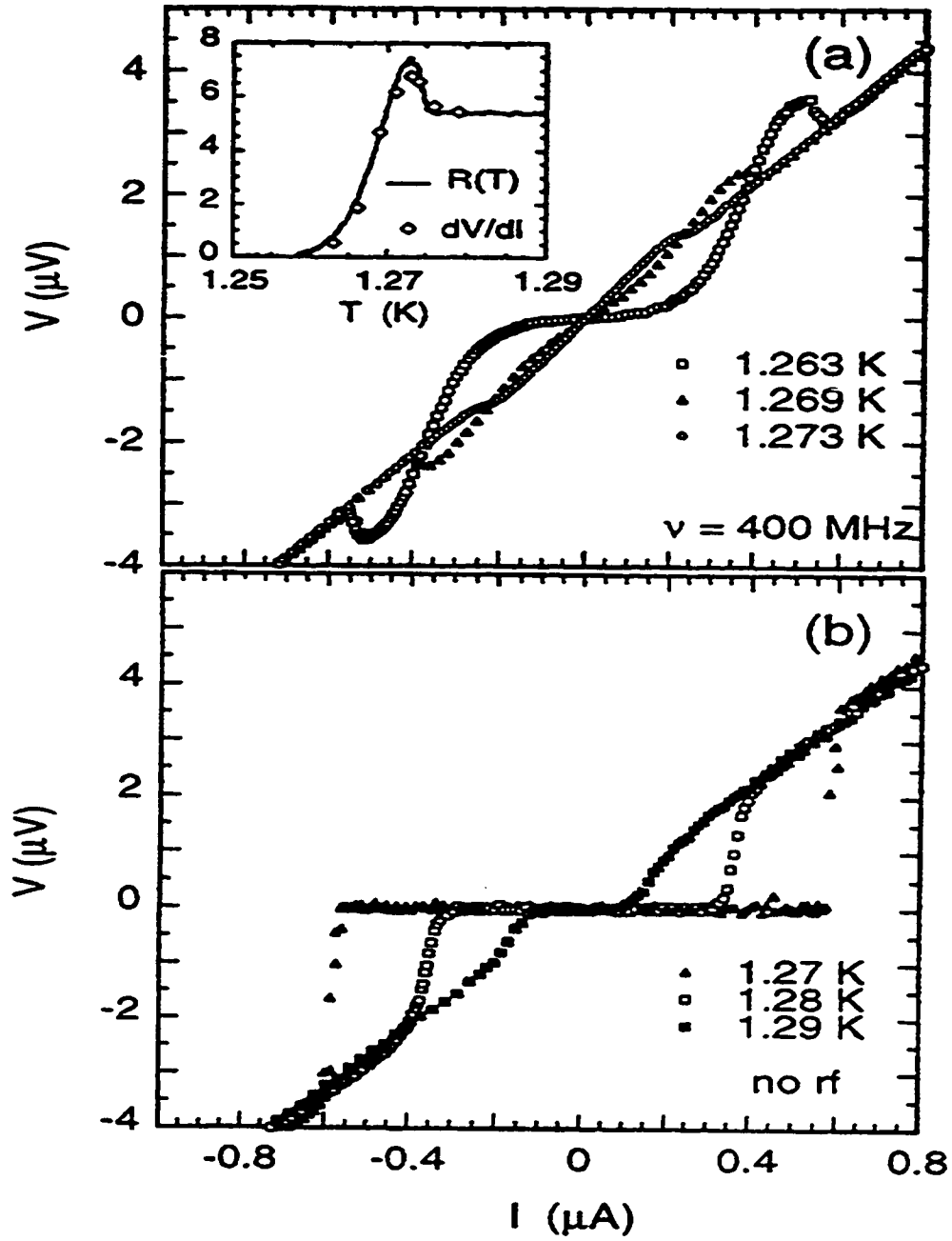


Fig. 4.1.6 (a)  $V(I)$  characteristic measured over  $V_1/V_3$  with a 400 MHz, -50 dB rf signal applied. The inset of (a) compares the resistance obtained from ac resistance measurement and the slope of the  $V(I)$  curves at zero dc current. (b) is the same measurement without an applied rf signal at different temperatures. (From C. Strunk *et al.* Ref. [6]).

compares the previous  $R(T)$  curve with the data taken from the zero-current slopes of several I-V curves measured at different temperatures. They show good agreement and therefore confirm that the origin of the resistance anomaly observed in  $R(T)$  is from the excess voltage in I-V curve. Fig. 4.1.6(b) is the I-V measurement at different temperatures near 1.273 K without any rf signal applied. The data does not show any excess voltage.

#### 4.1.4 Resistance anomaly induced by a magnetic field

The results of previous two sections strongly show the properties of charge imbalance. Since there is no apparent NS interface in the sample, a PSC has been suggested to explain the origin of the NS interface. Although the origin of the rf induced PSC is still not clear [9], the model of PSC is commonly introduced to explain the broadening of the  $R(T)$  curve of a 1D superconducting wire. A PSC is most likely induced at the spot of weakest superconductivity [1, 5, 9, 27]. Instead of applying rf signals, an alternative way of forming a PSC in our sample is to apply a magnetic field perpendicular to the loop. Near the superconducting transition, due to fluxoid quantization,  $T_c$  oscillates as a function of the flux threading the loop, the well known Little-Parks (LP) oscillations [104]. Therefore, one can perform the previous measurement by tuning  $T_c$  of the loop to suppress its order parameter, and therefore create a PSC in one arm of the loop.

Replacing the film thickness  $t$  with the width of the wire, one can use a formula derived by Tinkham [18] for the  $T_c$  suppression of a 1D S wire exposed to a perpendicular magnetic field  $B$ :

$$T_c(B) = T_{c0} \left[ 1 - \frac{\pi^2}{3} \left( \frac{d\xi_{GL} B}{\Phi_0} \right)^2 \right] \quad (4.1.2)$$

In the case of a loop, the Little-Parks oscillations are superimposed with the monotonic background suppression of  $T_c$  given by Eq. 4.1.2 [105]:

$$T_c(B) = T_{c0} \left\{ 1 - \left( \frac{\xi_{GL}}{R_m} \right)^2 \left[ \left( \frac{\pi R_m^2 B}{\Phi_0} \right)^2 (1 + z^2) - 2n \frac{\pi R_m^2 B}{\Phi_0} + \frac{n^2}{2z} \ln \left( \frac{1+z}{1-z} \right) \right] \right\} \quad (4.1.3)$$

where  $R_m = (R_{max} + R_{min})/2$  is the average of the inner and outer radii of the loop,  $w = R_{max} - R_{min}$  is the width of the wire and  $z = w/2R_m$ , the loop aspect ratio. The integer  $n$  has to be chosen such that  $T_c(B)$  is maximized for a given value of  $B$ .

Fig. 4.1.7 shows the magnetic field dependence of the critical temperature of the segment  $V_1/V_2$  (termed loop segment) as well as that of segment  $V_1/V_3$  (termed lead segment).  $T_c(B)$  corresponds to the point of the transition curve where  $R(T, B) = R_N/2$ . At low magnetic fields the LP oscillations are clearly seen in the loop segment, while only small oscillations due to nonlocal effects [106] are seen in the lead segment. The solid line in Fig. 4.1.7 represents the case of the classical LP effect for an isolated loop.

In Fig. 4.1.8 the  $R(T)$  curves for the loop segment were measured at half-integer (a) and integer (b) values of the reduced flux  $\Phi/\Phi_0$ , where  $\Phi_0 = h/2e$  is the superconducting



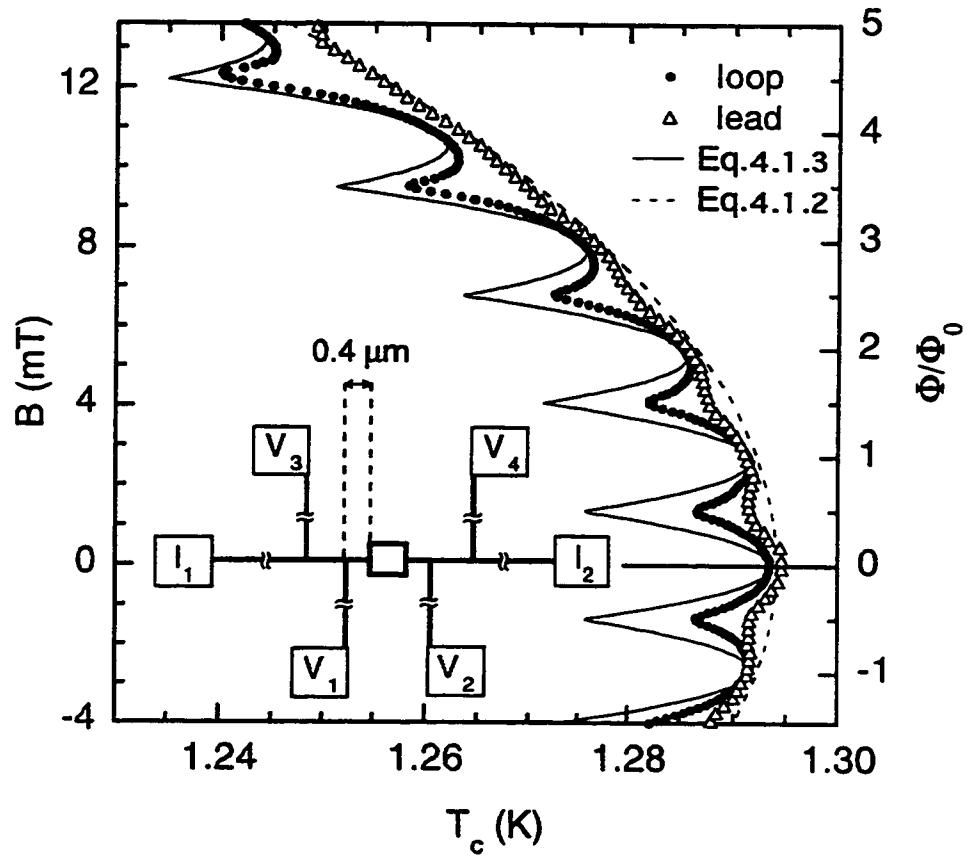


Fig. 4.1.7 Phase boundary  $T_c(B)$  for the loop segment ( $V_1/V_2$ ) and the lead segment ( $V_1/V_3$ ) for the Al Loop structure. Dashed and solid lines are fits according to Eq. 4.1.2 and 4.1.3, respectively. (From C. Strunk *et al.* Ref.[9]).

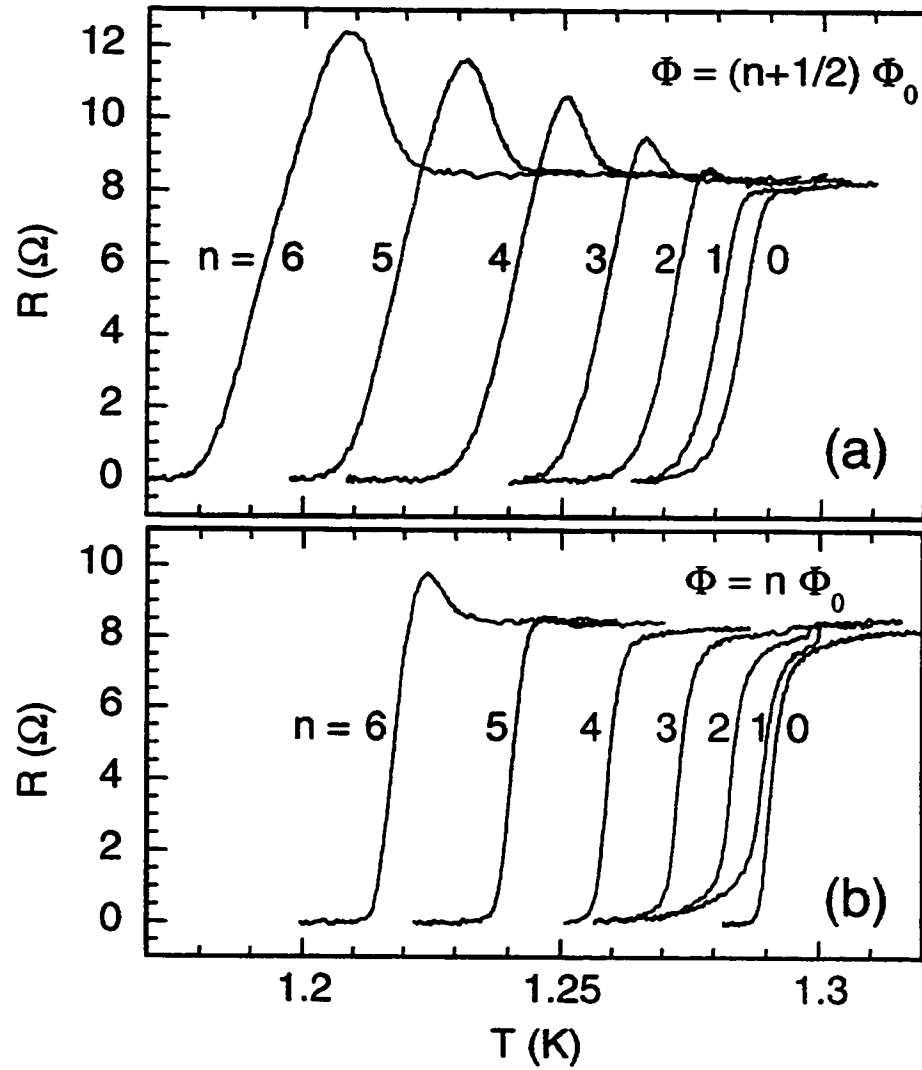


Fig. 4.1.8  $R(T)$  curves of the loop sample measured with voltage leads ( $V_1/V_2$ ) corresponding to the resistance of the loop for the Al Loop structure at (a) half-integer and (b) integer values of  $\Phi/\Phi_0$ . (From C. Strunk *et al.* Ref. [9]).

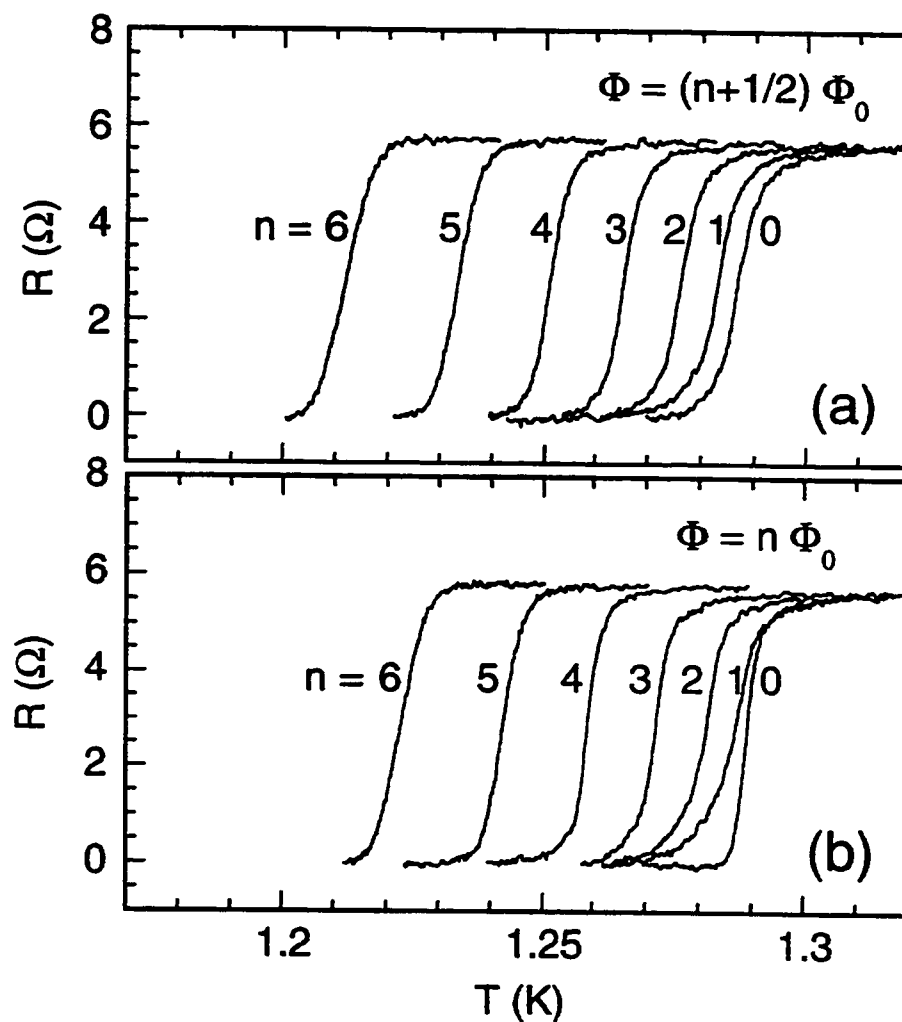


Fig. 4.1.9  $R(T)$  curves measured with voltage leads ( $V_1/V_3$ ) corresponding to the resistance of the line adjacent to the loop for the Al Loop structure at (a) half-integer and (b) integer values of  $\Phi/\Phi_0$ . (From C. Strunk *et al.* Ref. [9]).

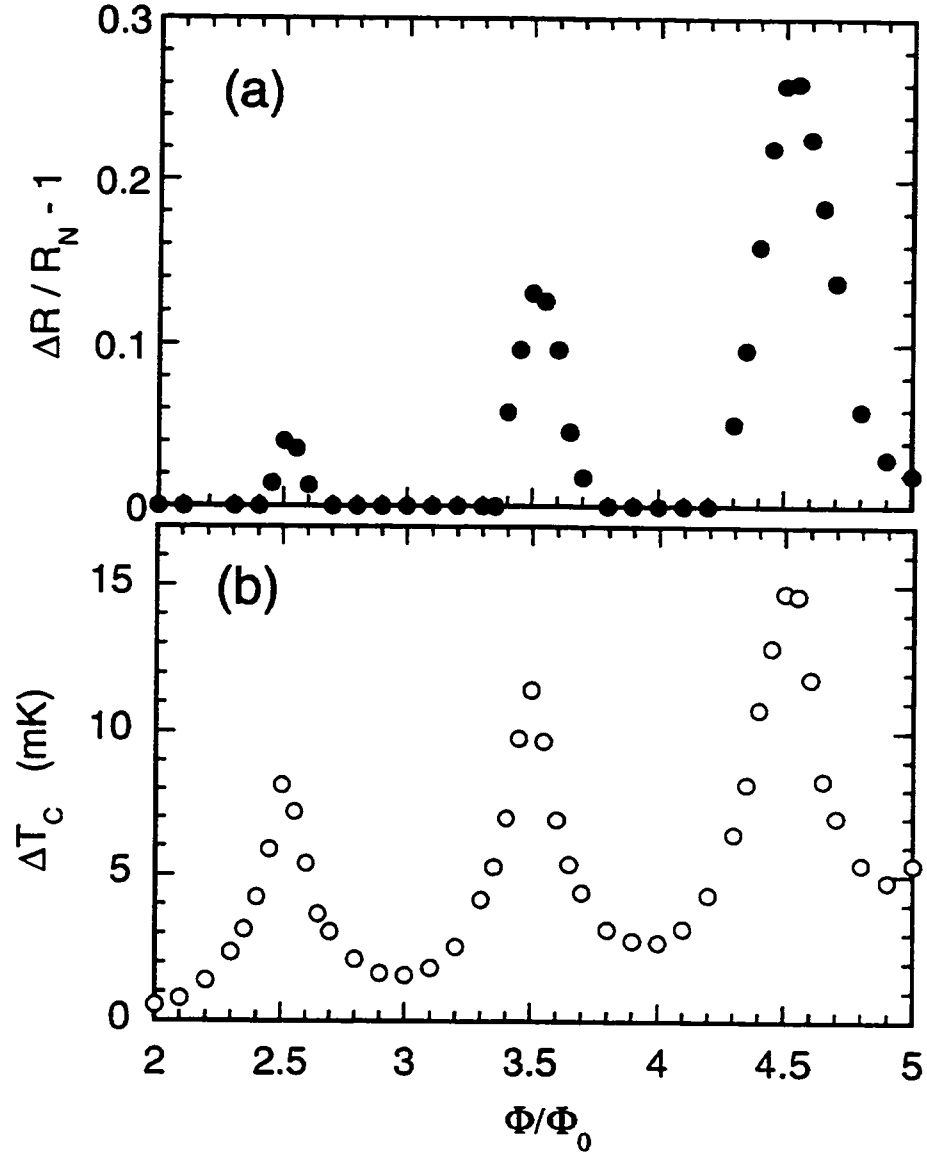


Fig. 4.1.10 (a) Normalized height  $R_{\max}/R_N - 1$  of the resistance anomaly and (b) difference in the critical temperature  $\Delta T_c = T_c^{(\text{lead})} - T_c^{(\text{loop})}$  vs.  $\Phi/\Phi_0$ . (From C. Strunk *et al.* Ref. [9]).

flux quantum. At  $\Phi = (n+1/2)\Phi_0$ , corresponding to a local minima of the order parameter in one arm of the loop, large resistance anomalies appear for  $n \geq 3$ . The resistance anomaly increases with  $n$  and can become as high as 50% of the normal state resistance  $R_N$  for  $n = 6$ . In contrast, when  $\Phi = n\Phi_0$  no anomalies are seen for  $n \leq 4$ . At higher values of  $\Phi/\Phi_0$ , i.e.,  $\Phi = 5\Phi_0$  and  $\Phi = 6\Phi_0$ , smaller resistance anomalies appear. For the lead segment, no anomaly appears in the same field range (Fig. 4.1.9).

A correlation between the height of the resistance maximum  $R_{\max}$  and the locally suppressed transition temperature  $T_c$  in the loop is clearly shown in Fig. 4.1.8 and 4.1.9. This correlation is clearly shown in Fig. 4.1.10 where the top and bottom panels show the normalized height of the resistance peak  $R_{\max}/R_N - 1$  and the variation of  $\Delta T_c$  as a function of  $\Phi/\Phi_0$ , respectively. We can conclude that the resistance anomalies observed in Fig. 4.1.8(a) are indeed due to the suppression of  $T_c$  of the loop when a magnetic field is applied.

## 4.2 Noise-induced resistance anomaly in a plain Al wire

Motivated by the results of the previous section, B. Burk *et al.* [7, 8] found that the resistance anomaly can also be induced by a ‘noise’ current of lower frequency applied to the current leads of the sample. The idea is that unfiltered rf or 50-60 Hz noise can also

result in a resistance anomaly, but due to a very different mechanism. As shown in Fig. 4.2.1, a noise current  $I_n$  superimposed on the dc current during the measurement, if large enough, can sample the nonlinear portion of the I-V curve of a superconductor, where the slope of this curve  $dV/dI$  is much larger than the normal state resistance. Consequently, the detected voltage  $V_{ave}$  can be larger than the normal state voltage  $V_{norm}$  at the same dc current, and an excess voltage results.

#### 4.2.1 Sample properties and measurements

The SEM picture of the sample discussed in this section is shown in Fig. 4.1.1(c) and its properties are summarized in Table 4.1. Since  $T_c = 1.324$  K, above  $T = 1.274$  K the 1D criterion  $\xi(T) \gg w, t$  is satisfied. The samples were measured using standard four-terminal ac measurement techniques as described in Chapter 2. In addition to the ac probe current  $I_p$  applied, a sinusoidal ac 'noise' current  $I_n$  was also imposed on the sample by injecting  $I_n$  into the same current leads where  $I_p$  is applied during the measurement. In order to minimize interference from external electromagnetic sources, each lead into the low temperature cryostat was passed through a  $\pi$ -filter with a cutoff frequency of 10 MHz. The sample was made by the author and the measurement was performed by B. Burk at Northwestern University.

#### 4.2.2 Resistance anomaly in $R(T)$ induced by applying a noise current

We shall use the notation  $R_{ij,kl}$  to denote the ac resistance measured when the ac current is applied through contacts  $i$  and  $j$ , and the ac voltage measured across contacts  $k$  and  $l$ . Fig.

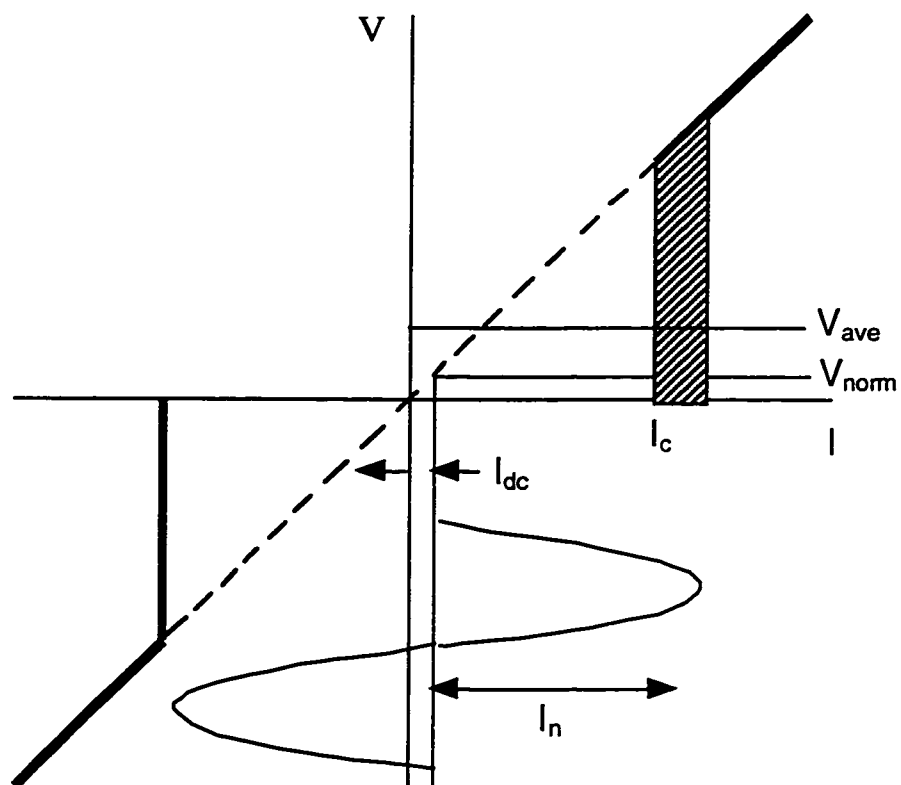


Fig. 4.2.1 Phenomenological picture of the mixing effect. (From Burk *et al.* [8]).

4.2.2 shows  $R_{18,45}$  with various rms amplitudes of a 1 kHz 'noise' current applied through the current leads 1 and 8 shown in the sample schematic in the inset. Without any noise current, no resistance anomaly is observed. As a noise current  $I_n$  is applied, the amplitude of the resistance anomaly clearly increases with  $I_n$ . The peak is relatively sharp for intermediate amplitudes of the noise current, but becomes broader as the noise current is increased. These data are similar to Fig. 4.1.4, the resistance anomaly induced by an rf signal.

#### 4.2.3 Model of Mixing

In order to explain the result of Fig. 4.2.2, a numerical simulation based on the mixing model described above is presented here. Following B. Burk *et al.* [8] we first numerically expand the intrinsic current voltage characteristic  $V(I)$  without any noise signal obtained from the superconductor in a Fourier series of the form:

$$V(I) = \sum_{m=-\frac{N}{2}}^{\frac{N}{2}} V_m \exp \left[ i 2\pi m \left( \frac{I}{I_0} \right) \right] \quad (4.1.4)$$

where  $I_0$  is the current range of the current voltage characteristic,  $N$  is the number of data points in the curve, and  $V_m$  is the  $m$ th Fourier component of the voltage.  $I = I_{dc} + I_p(t) + I_n(t)$  is the total current, where  $I_p(t) = I_{po} \sin(2\pi f_p t)$  is the probe or measuring current with frequency  $f_p$ , and  $I_n(t) = I_{no} \sin(2\pi f_n t)$  is the noise current with frequency  $f_n$ . Using the



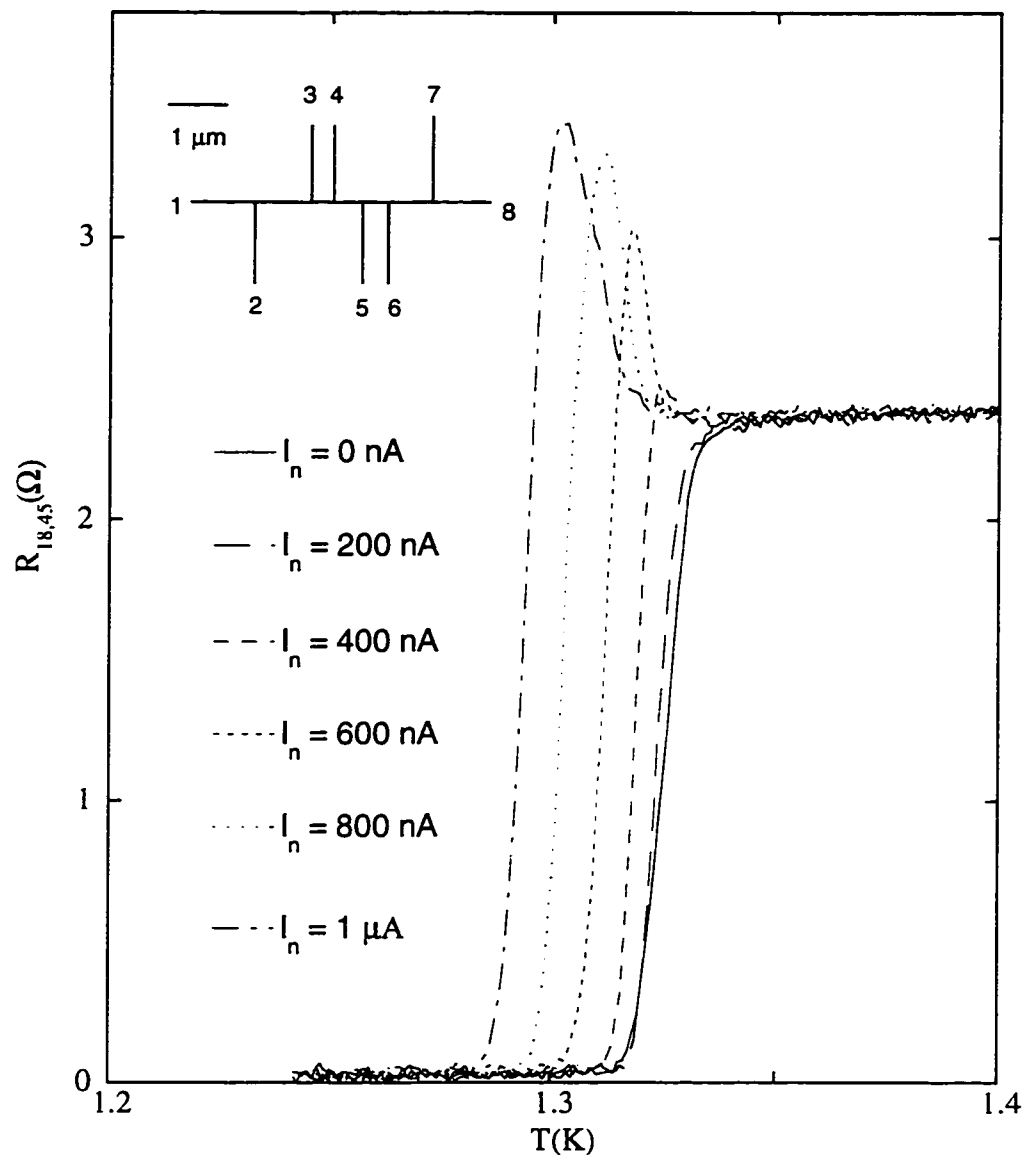


Fig. 4.2.2  $R_{18,45}$  as a function of temperature  $T$  for the sample schematic shown in the inset with a low frequency ( $\sim 1$  kHz) signal of different amplitudes applied through the current leads. (From B. Burk *et al.* Ref.[8]).

Bessel series expansion for  $\exp(z\sin(x))$ , we obtain the component  $V_p$  of the voltage corresponding to the probe frequency  $f_p$

$$V_p = \sum_{m=-\frac{N}{2}}^{\frac{N}{2}} (2i)^m V_m \exp\left[i2\pi m \left(\frac{I_{dc}}{I_o}\right)\right] J_1\left[2\pi m \left(\frac{I_{po}}{I_o}\right)\right] J_0\left[2\pi m \left(\frac{I_{no}}{I_o}\right)\right] \quad (4.1.5)$$

where  $J_r(x)$  is the Bessel function of  $r$ th order. The calculated differential resistance is then given by

$$\left(\frac{dV}{dI}\right)_{calc} = \frac{V_p}{I_{po}} \quad (4.1.6)$$

The input to above analysis is the intrinsic differential resistance curve measured without an intentional superimposed noise current.

#### 4.2.4 Resistance anomaly in $dV/dI$ induced by applying a noise current

We now apply the calculation to our experimental data. Without any intentional noise applied to the sample and with proper shielding of all electrical lines, a set of  $dV/dI(I_{dc})$  curves for the configuration  $R_{18,45}$  are first measured at various temperatures ( $I_p=10$  nA and  $f_p=11.7$  Hz). They are shown in Fig. 4.2.3(a). Their corresponding I-V curves are obtained by numerically integrating the  $dV/dI(I_{dc})$  curves (4.2.3(b)). These curves show the usual behavior of a S wire. No excess voltage is observed.

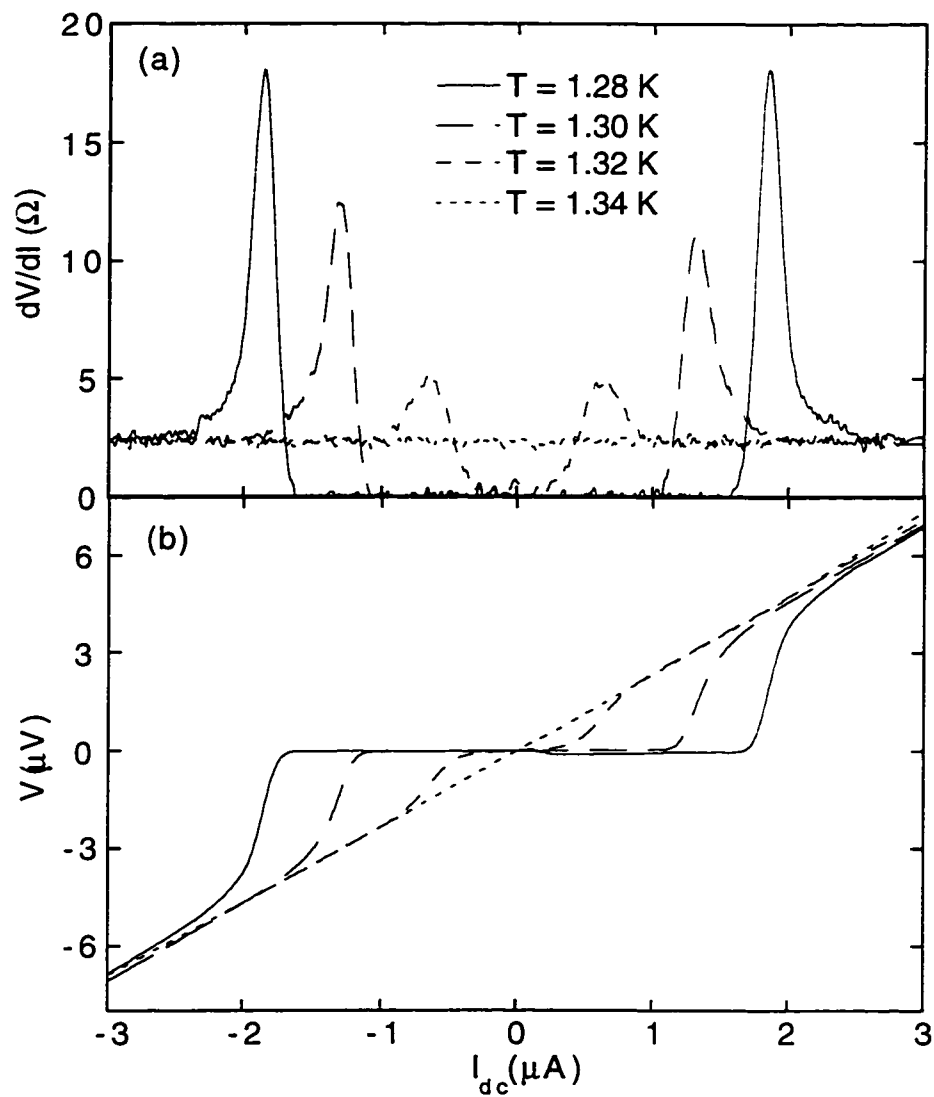


Fig. 4.2.3 (a) Differential resistance curves for the configuration  $R_{18,45}$  with no intentional noise current applied, at four different temperatures near  $T_c$ . (b) Numerically integrated IV curves obtained from (a). (From B. Burk *et al.* Ref.[8]).

We first test our calculation on the I-V curve corresponding to  $T=1.30$  K with a noise current  $I_n=1$   $\mu$ A,  $f_n=1$  kHz applied to the same current leads where  $I_p$  and  $I_{dc}$  are injected. The curve obtained from the procedure in section 4.3.3 is compared with the measured curve and is shown in Fig. 4.2.4(a). The agreement is good. Both curves peak at  $I_{dc} = 0$  nA where they exceed the normal state resistance  $R_n$ , become smaller than  $R_n$  at  $I_{dc} = 500$  nA, and finally reach  $R_N$  at larger  $I_{dc}$ .

In order to reconstruct the calculated  $R(T)$  curve, we calculated several  $dV/dI(I_{dc})$  curves at different temperatures whose result is shown in Fig. 4.2.4(b). By plotting the zero-dc current  $dV/dI$  as a function of the temperature we obtain the calculated  $R(T)$  curve with a noise current 1  $\mu$ A and 1 kHz applied. This result is compared with the measured curve shown in Fig. 4.2.5, in which a  $R(T)$  curve without any intentional noise current applied is also plotted. The calculated curve shows an excellent fit to the measured curve.

### 4.3 Comparison of the “rf” and “noise” induced resistance anomalies

The mixing effect discussed above raises the question of whether the rf induced resistive anomaly is due to an intrinsic property related to charge imbalance in the sample or an extrinsic effect due to a possible mixing of the measuring current with an external noise signal. How can we distinguish between these two effects? Relying on our structural characterization, we can exclude local variations of the cross section as a possible cause of the resistance anomaly (see Fig. 4.1.2). No significant structural defects are found at

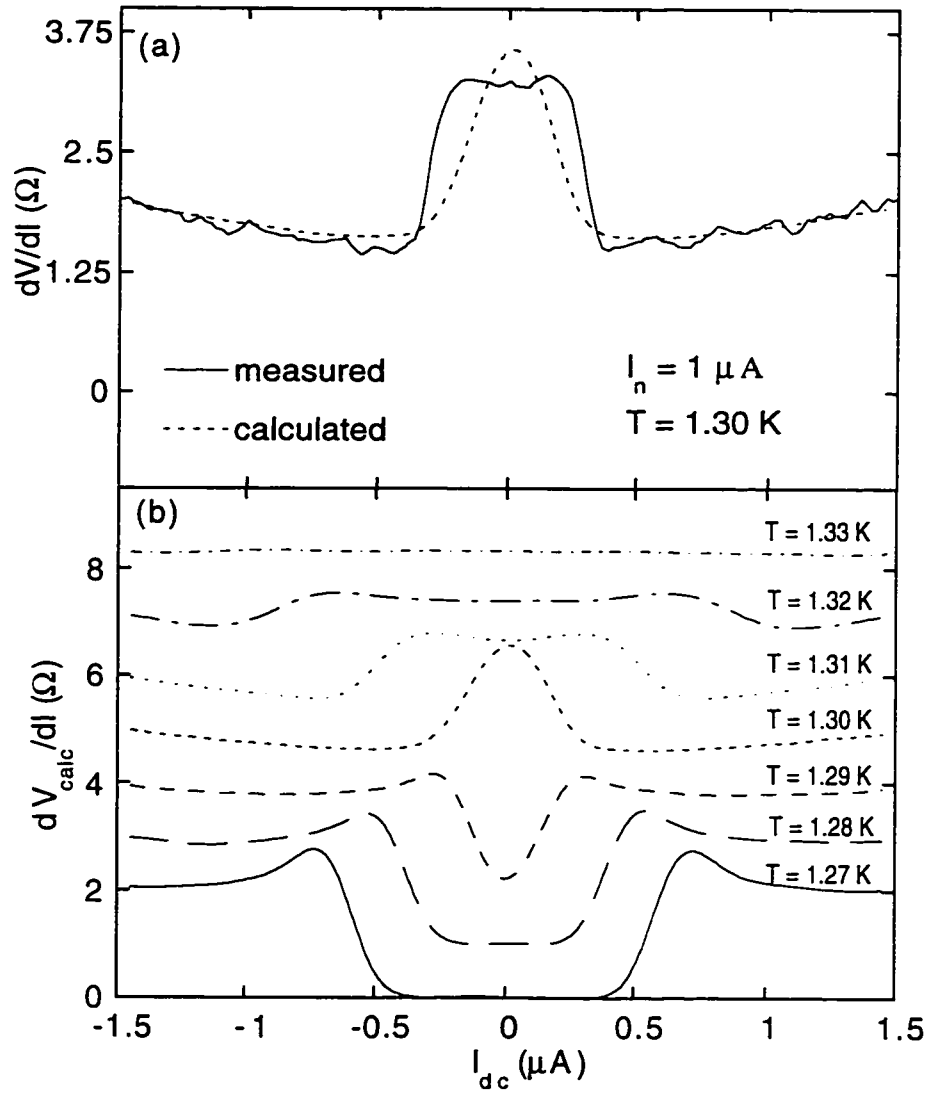


Fig. 4.2.4 (a) Comparison of measured and calculated differential resistance curve for the configuration  $R_{18,45}$  in the presence of a 1 kHz noise current of rms amplitude 1  $\mu A$ . The calculated curve is obtained from a measured  $dV/dI$  curve with no noise current applied. (b) Calculated  $dV/dI$  curves with 1 kHz noise current of rms amplitude 1  $\mu A$  at various temperatures. For clarity, the curves are successively offset by 1  $\Omega$ . Note the peak near zero bias at  $T = 1.30 K$ , which gives rise to the resistance peak in  $R(T)$ . (From B. Burk *et al.* Ref.[8]).

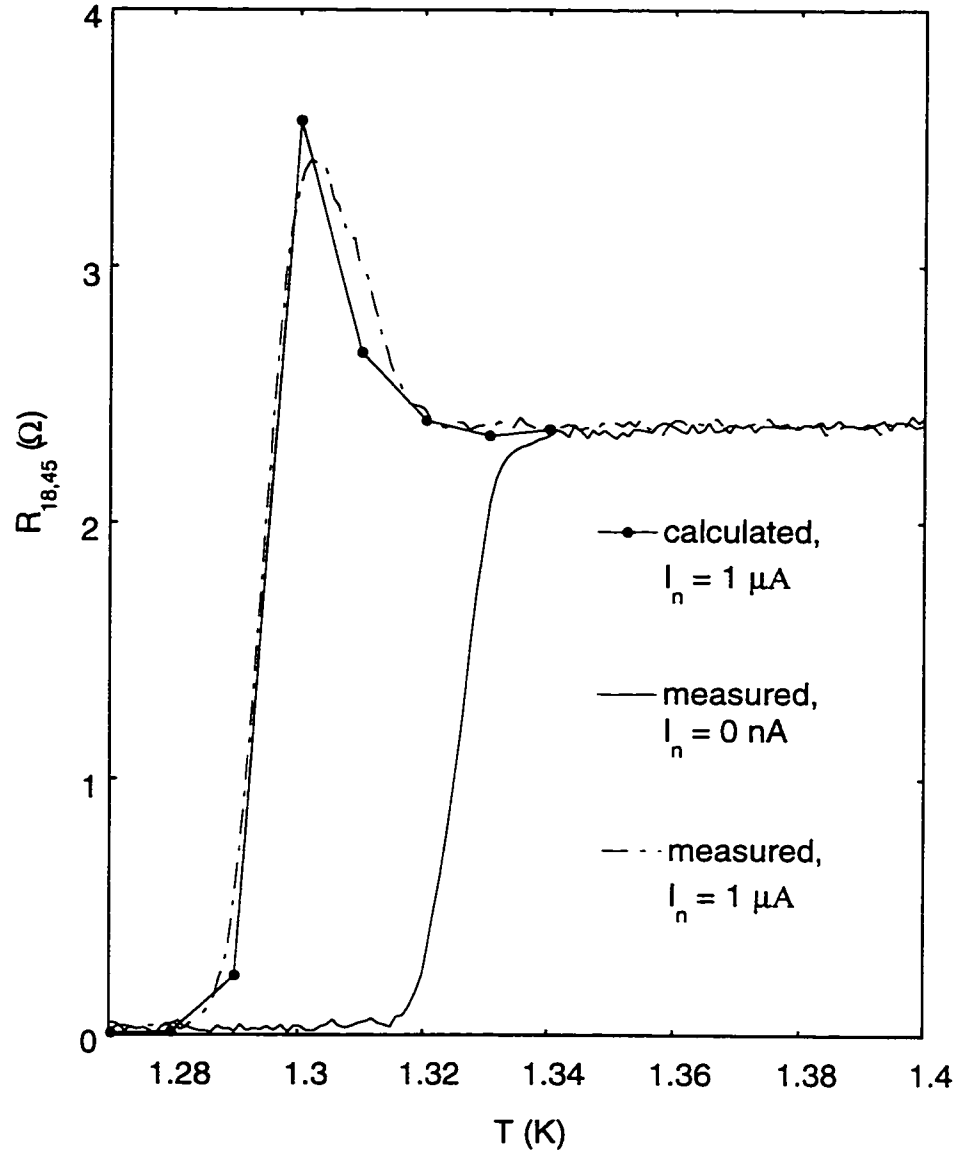


Fig. 4.2.5 Comparison of the resistance  $R_{18,45}$  as a function of  $T$  in the presence of a 1 kHz noise current of rms amplitude  $1 \mu\text{A}$ , with the corresponding calculated value obtained by taking the differential resistance at zero bias from the calculated  $dV/dI$  curves of Fig. 4.3.3(b). Also shown is the measured intrinsic  $R_{18,45}$  as a function of  $T$  with no noise current applied. (From B. Burk *et al.* Ref.[8]).

different locations of the sample. The first difference between the rf induced RA and the noise induced RA is in the I-V characteristic. The mixing effect can induce an enhancement of the differential resistance above  $R_N$  near zero bias current. However, in contrast to the rf induced RA,  $dV/dI$  is expected to remain always positive for a simple mixing mechanism. Therefore, it cannot explain the observation of negative  $dV/dI$  in some superconducting samples [5, 9, 70]. The second difference between the two mechanisms is in the spatial dependence of the resistance anomaly. Since the mixing effect is observed on a mesoscopic wire the critical current is expected to be rather homogeneous. Therefore the RA due to mixing should not be suppressed by increasing the spacing between two voltage probes significantly. All these suggest an origin of the rf induced resistance anomaly in favor of an intrinsic property related to charge imbalance in the sample.

#### 4.4 Resistance anomaly observed in a 1D NS wire

In the last section, we described experiments on one system in which a resistance anomaly can be observed. This was a pure superconducting wire, which can be either one dimensional [1, 3, 4, 6-9] or two dimensional [2, 5, 27]. The common explanation of the resistance anomaly in this system arises from the nucleation of a PSC in the sample and consequently the existence of a charge imbalance region. An important property of the charge imbalance is the coexistence of two chemical potentials, i.e.,  $\mu_p$  and  $\mu_q$  in the charge imbalance region.  $\mu_q$  decays over a characteristic length  $\Lambda_Q$  much longer than  $\xi(T)$  while  $\mu_p$  remains almost constant in the entire charge imbalance region. A PSC can be created by intentionally weakening the superconductivity at a local spot. This can be achieved by

intentionally creating a defect in the sample geometry [27] or by applying an external parameter such as a magnetic field [3, 9] or a rf signal [6, 9].

Another system for studying the resistance anomaly is in a NS system. In this system the most common way to create a NS interface is to etch part of a 2D superconducting stripe. The etched region becomes a weak superconductor whose properties are usually revealed by a slight suppression of  $T_c$  and  $I_c$ . Consequently, a charge imbalance region is created near the boundary between the superconductor (S) and the weakened superconductor (W). By placing various N or S probes near the boundary, one can detect the difference between  $\mu_p$  and  $\mu_q$ . The spatial dependence of the charge imbalance is implied in the gradual decrease of the resistance anomaly as the voltage probes move away from the WS boundary (W denotes a weaker superconductor with respect to S). An example is the experiment done by Park *et al.* [5]. Since the resistance anomaly observed in such a system stems from charge imbalance, one is easily lead to another important phenomenon associated with charge imbalance, that is, the excess voltage as discussed in section 4.2.2. This excess voltage can further be revealed in the negative differential  $dV/dI$  which was shown in the experiment by Yu and Mercereau [70] and the experiment by Park *et al.* [5] as discussed in Chapter 2. Although these experiments have beautifully demonstrated the major properties of charge imbalance, they were done in 2D systems. In addition, both metals are superconductors; for example, in the experiment of Park *et al.*, the temperature at which the differential resistance measurements were performed was below the transition temperatures of both superconductors. As the dimensions of the system are decreased, one may expect some usual results. To our knowledge, there are not many experiments of charge imbalance done in a 1D NS wire.



Hence, in this and the following sections we present results of our measurements on the study of nonequilibrium effects in 1D NS structures.

We first present some data for a N-S cross structure as shown in Fig. 4.4.1. This sample is made of an Au film as the normal metal and an Al film as the superconductor by using two-step e-beam lithography as described in chapter 2. The film properties are as follows: Au thickness  $\sim 26$  nm, Al thickness  $\sim 36$  nm, wire linewidth  $\sim 0.2$   $\mu\text{m}$ , normal metal Au coherence length  $\xi_N(T) \sim 0.6 \mu\text{m}/T^{1/2}$ , superconducting coherence length  $\xi_{Al}(T=0) = 0.14 \mu\text{m}$ , and  $T_{c0} = 1.268$  K. Therefore, near  $T_{c0}$ ,  $\xi_{Al}(T)$  is much larger than the wire linewidth, and the Al line satisfies the 1D criterion.

#### 4.4.1 Resistance anomaly in $R(T)$

Fig. 4.4.2 shows the normalized resistance as a function of temperature measured for four different measurement configurations. Only the combination of short superconductor ( $S_1$ ) with either short ( $N_1$ ) or long ( $N_2$ ) normal metal shows the resistance anomaly. This is consistent with the spatial dependence of the quasiparticle chemical potential  $\mu_q$  within the picture of charge imbalance. As the temperature is cooled through  $T_c$ , a charge imbalance is created in  $S_1$  and  $S_2$  near the NS interface respectively. This implies, for the combination including the long superconductor ( $S_2$ ), the superconducting voltage probe is placed at a distance larger than the charge imbalance length. In the experiment by Kwong *et al.* [2], in which a weak superconducting region (W) was created in the middle of a 2D

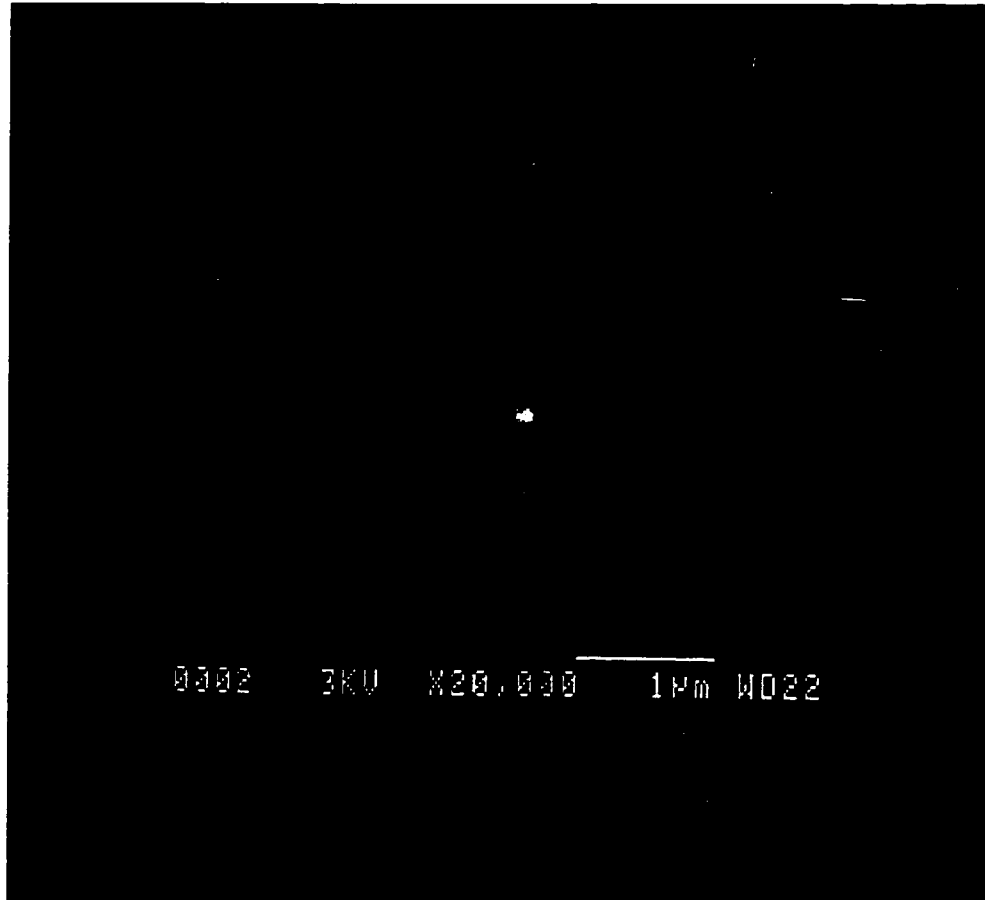


Fig. 4.4.1 Scanning electron micrograph of the 1D NS cross sample.

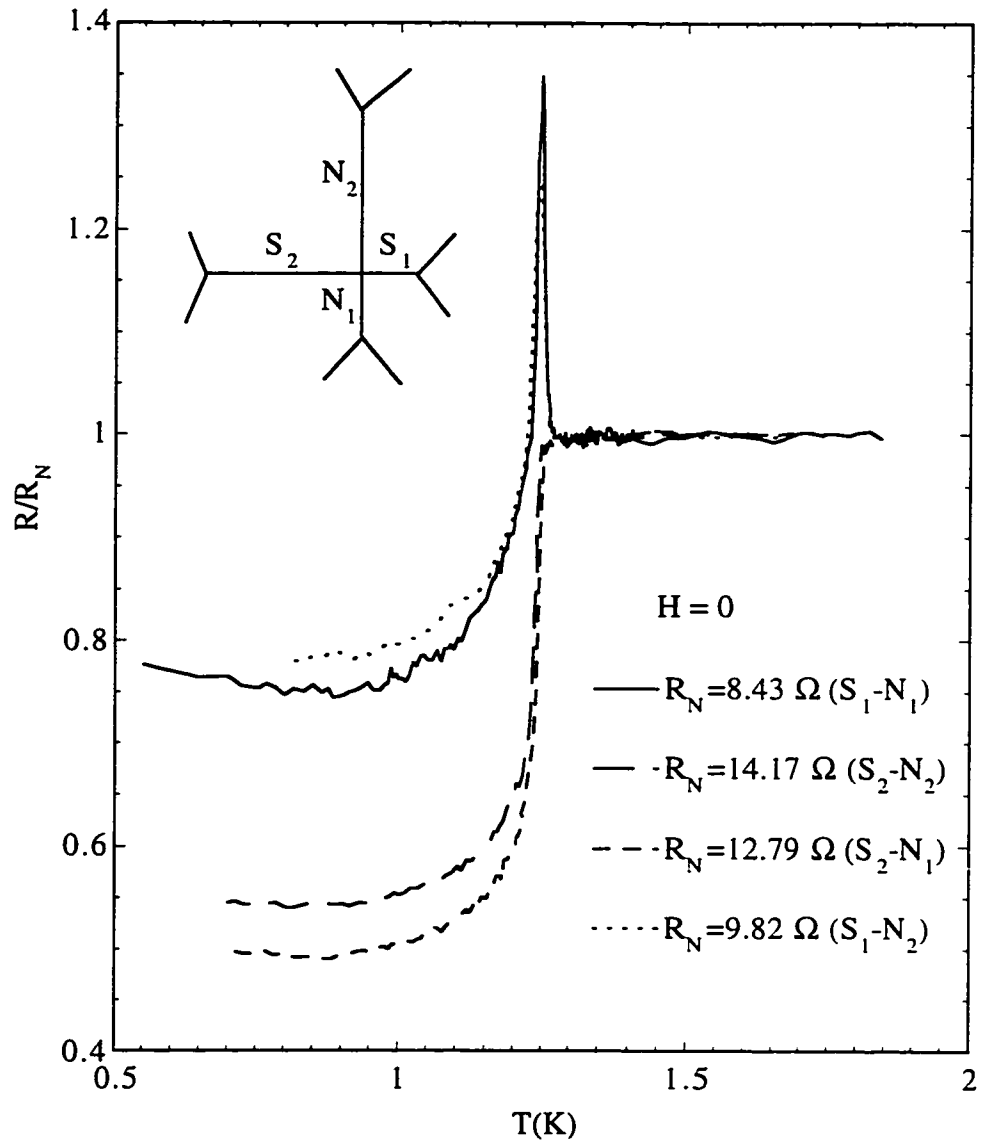


Fig. 4.4.2 Normalized resistance as a function of temperature  $T$  for different measurement configurations at zero magnetic field. The bracket behind each normal state resistance  $R_N$  denotes the combination of two sections measured as shown in the inset. Only the combination including a short superconductor shows a resistance anomaly.

superconducting stripe and various W and S voltage probes were placed at different distances on the two sides of the W region. Although their geometry differs from our sample in the dimension of the superconductor where the charge imbalance occurs, it may be instructive to compare our experiment with their results. We found two major differences. First, the charge imbalance length observed in our sample is shorter by a factor of  $\sim 20$ . Second, the resistance anomaly observed in our sample is  $\sim 35\%$  of the normal-state resistance, which is larger than the result of Kwong *et al.* by a factor of 7. The amplitude of the resistance anomaly observed in our sample is similar to the observation of Santhanam *et al.* [1], in which the resistance anomaly was observed in a 1D pure superconducting wire. However, in the experiment of Santhanam *et al.*, the charge imbalance length extends over a distance longer than  $5\text{ }\mu\text{m}$ . Note that the presence or absence of the resistance anomaly does not depend on the length of the normal arm, showing that the resistance anomaly is indeed related to effects in the superconductor.

#### 4.4.2 Negative $dV/dI(I)$

We now examine the differential resistance  $dV/dI$  as a function of dc current  $I$ . Fig. 4.4.3 shows the  $dV/dI(I)$  curves at  $T=280\text{ mK}$  corresponding to the four measurement configurations in the previous  $R(T)$  measurement (Fig. 4.4.2). A small peak visible at zero current is similar to the reentrance effect observed in some proximity effect experiments [12-17]. This effect is a consequence of the long range coherence of the electron-hole pair correlation due to Andreev reflection at the NS interface [36]. A detailed study of this reentrance effect is presented in Chapter 5. At  $I \sim 10\text{ }\mu\text{A}$ , rich features containing peaks and dips are observed. The general behavior is as follows: A small peak first develops, followed by one or two dips and a sharp peak and a small broad bump is finally reached

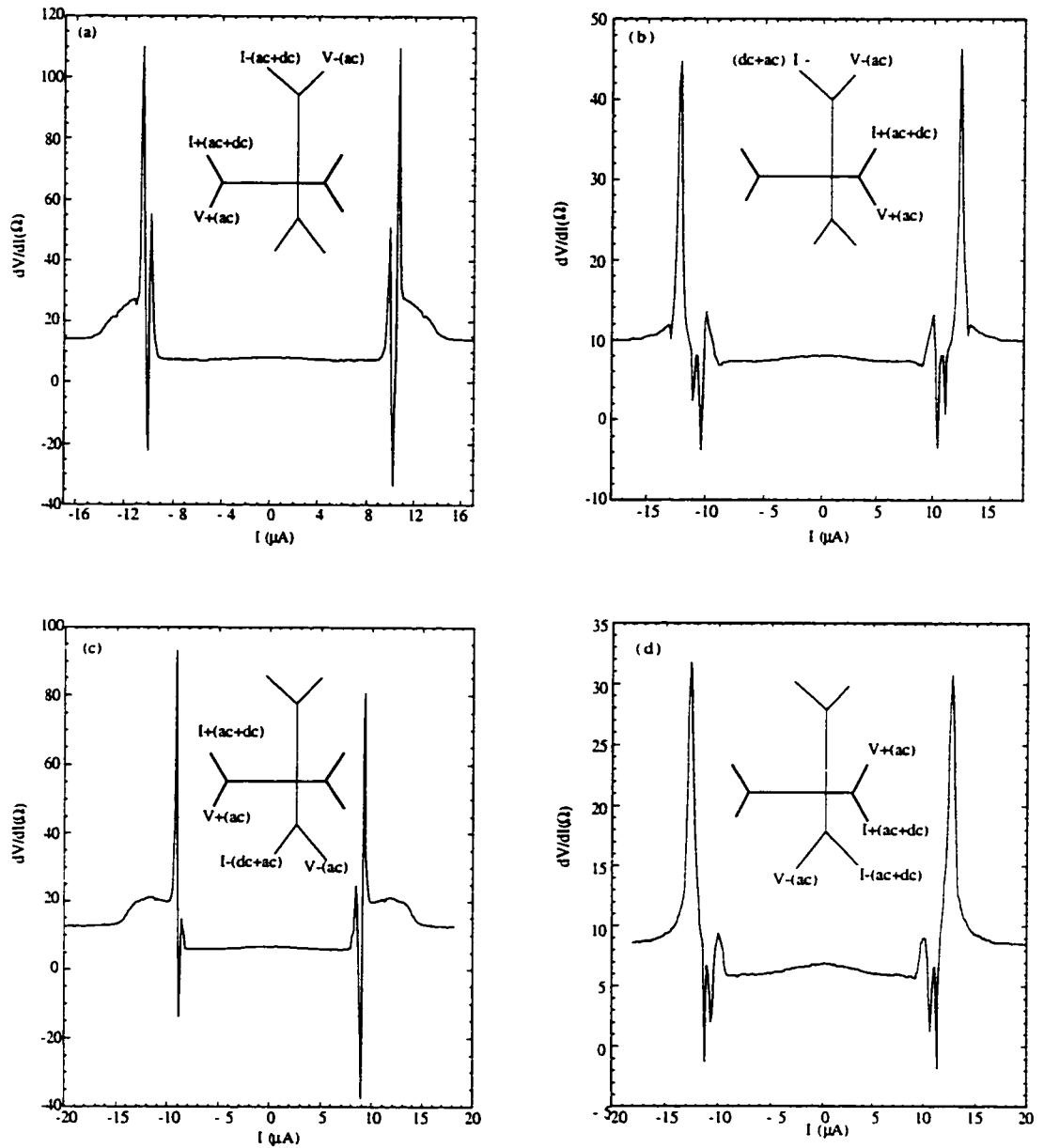


Fig. 4.4.3 Differential resistance  $dV/dI$  as a function of dc current measured for various measurement configurations shown in the inset of each plot. The curves for the measurement configuration including a long superconductor clearly show a negative  $dV/dI$  while the curves including a short superconductor show double dips, one of which goes to negative resistance.

before the normal state resistance. The detailed features depend on the measurement configuration. This dependence can be generalized as follows: (i) Only one dip is observed in the configuration which includes a long superconductor, while when the short superconductor is measured, two dips are observed. (ii) In general, these peaks and dips are symmetrical. (The asymmetry visible in Fig. 4.4.2 is associated with the sweep rate of the current and is not an intrinsic effect.) (iii) A negative  $dV/dI$  is observed in each measurement configuration, being more pronounced when the long superconductor is measured. (iv) All these curves are reproducible upon sweeping the current in the opposite direction.

As described in Section 4.1.2 another manifestation of the charge imbalance is an excess voltage existing in the I-V curve. The negative  $dV/dI$  is a consequence of the excess voltage [5, 9]. It was also observed in the experiment by Park *et al.* [5], who created a WS boundary in the middle of a 2D Al stripe by etching part of the stripe. The W part has a slightly lower  $T_c$  than the S part. The critical current  $I_c$  of the W part decreases along the W part of the stripe as one moves away from the WS interface, while  $I_c$  in the S part remains almost constant, being equal to  $I_c$  of the W part at the WS boundary. Thus, a phase-slip center is formed at the WS boundary. On the two sides of the WS boundary various etched and unetched voltage probes were placed with equal spacing to detect the quasiparticle potential and the pair potential. As a current is injected from the W part to the S part, a nonequilibrium region exists due to the unequal distribution of quasiparticles on the two branches of excitations. The inhomogeneity of the critical current in W region causes a moving PSC along the W region as the current is increased. As a result, they observed a sequence of negative  $dV/dI$  dips as the PSC moves in and out of each region between two

voltage probes, the multiple negative peaks being due to the nonlocal interaction between different PSCs. Within this picture, one is lead to the speculation that there exist two PSCs in our measurement containing the short superconductor. However, there is no additional voltage lead and therefore no apparent PSC exists adjacent to the voltage probes used in our measurement .

Recently, C. Strunk *et al.* [9] also reported negative  $dV/dI$  in a pure 1D S wire in which a resistance anomaly was induced by rf radiation. The negative  $dV/dI$  was attributed to the excess voltage due to charge imbalance near a rf radiation induced PSC. We would like to point out that phase-slip centers are mostly likely induced in pure superconductors (Chapter 2). The experiment of Park *et al.*, although was performed on an WS system, the explanation based on the PSC model is essentially applied to a *pure* superconductor considering the fact that their measurement was performed at temperatures below  $T_c$ . The difference between Ref. 9 and Ref. 5 is that in Ref. 9, the PSC is *fixed* at some particular spot while in Ref. 5, the PSC is *moving* in the superconductor. Our measurement, on the other hand, is performed in a 1D NS system with one fixed “PSC” - the NS interface. The additional negative  $dV/dI$  observed in the measurements containing the short superconductor, therefore, leads us to the speculation of an additional PSC being nucleated in the short superconductor. The absence of this additional PSC in the long superconductor may be due to the detailed morphology of the sample, which allows the nucleation of a PSC in the short section, perhaps in a region of suppressed superconductivity.

#### 4.4.3 Resistance anomaly in $R(T)$ at finite magnetic fields

One of the properties in all reported measurements of resistance anomalies is that the

resistance anomaly is sensitive to a small magnetic field. The general behavior of the resistance anomaly subjected to a small magnetic field is that  $T_c$  is first enhanced at a small field of few gauss, indicating that the resistance anomaly occurs in the superconducting state [6, 9]. As the field is further increased the resistance anomaly is suppressed and disappears at a field of  $\sim 20$ -30 gauss due to the suppression of the charge imbalance length [1-6, 9]. Based on the SBT model [66], C. Strunk *et al.* [9] plotted the charge imbalance length  $\Lambda_Q$  as a function of magnetic field  $B$  (Fig. 4.4.4). Near  $T_{c0}$ ,  $\Lambda_Q$  first decreases from the zero-field value as a small field is applied, reaches a minimum at a field of 35 gauss for a temperature 5 mK lower than  $T_{c0}$ , and eventually increases due to the depletion of  $\Delta$  as the field is further increased. We have observed this behavior in our 1D NS cross sample.

Fig. 4.4.5 shows an example corresponding to the measurement configuration  $S_1 - N_1$  in Fig. 4.4.2. A similar behavior was also observed in the  $S_1 - N_2$  configuration. For a magnetic field less than 10 gauss, the resistance anomaly is slightly increased. This increase was also observed in the experiment of Kwong *et al.* [2] and the origin is still not clear. At a field of 20 gauss, the resistance anomaly is completely suppressed and increases again at higher magnetic fields. The negative magnetoresistance at the temperature corresponding to maximum resistance in the resistance peak has been observed by Santhanam *et al.* [1]. In their experiment, the magnetoresistance showed similar behavior. However, their result did not show a reentrance of the resistance anomaly at high magnetic fields ( $R(H)$  reached  $R_N$  at high magnetic fields). Our observation provides a possible way of studying the resistance anomaly via the microscopic mechanism that



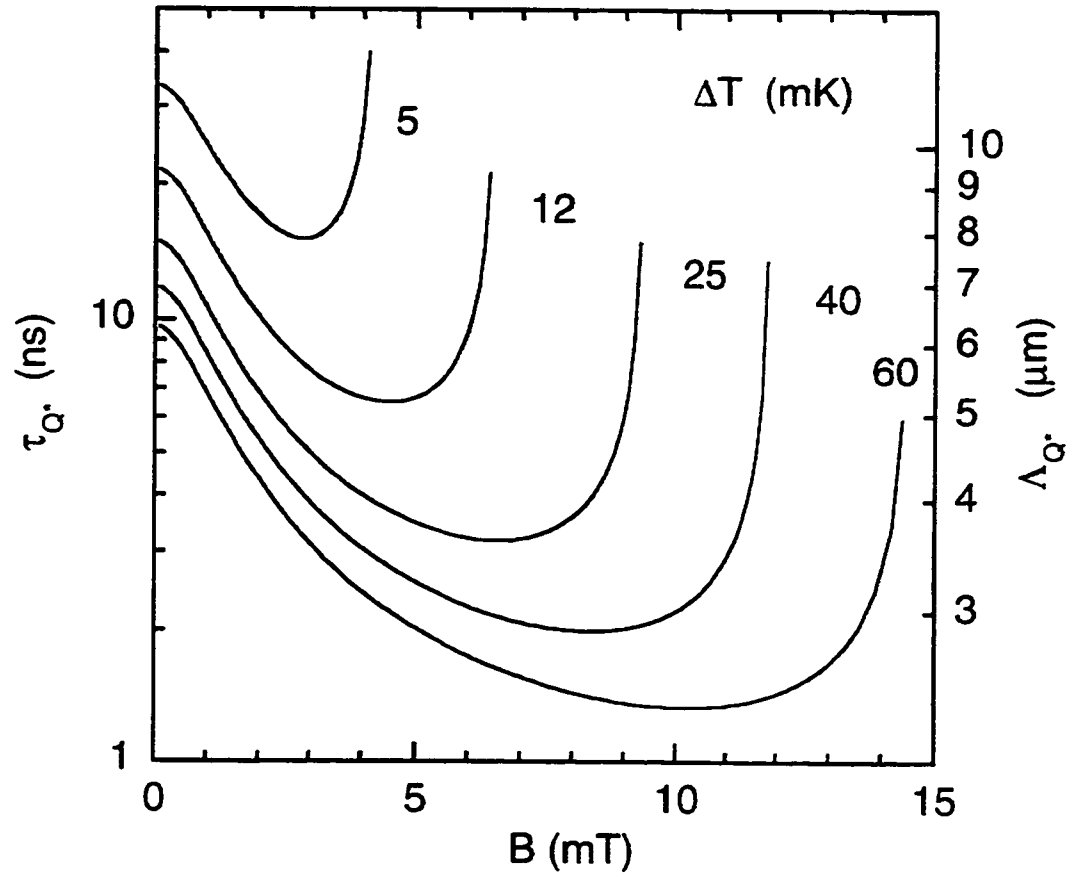


Fig. 4.4.4 Charge relaxation length  $\Lambda_{Q^*}$  and charge relaxation time as a function of magnetic field  $B$  at various temperatures below  $T_c$ .  $\Delta T = T_c - T$ . (From C. Strunk *et al.* Ref.[9]).

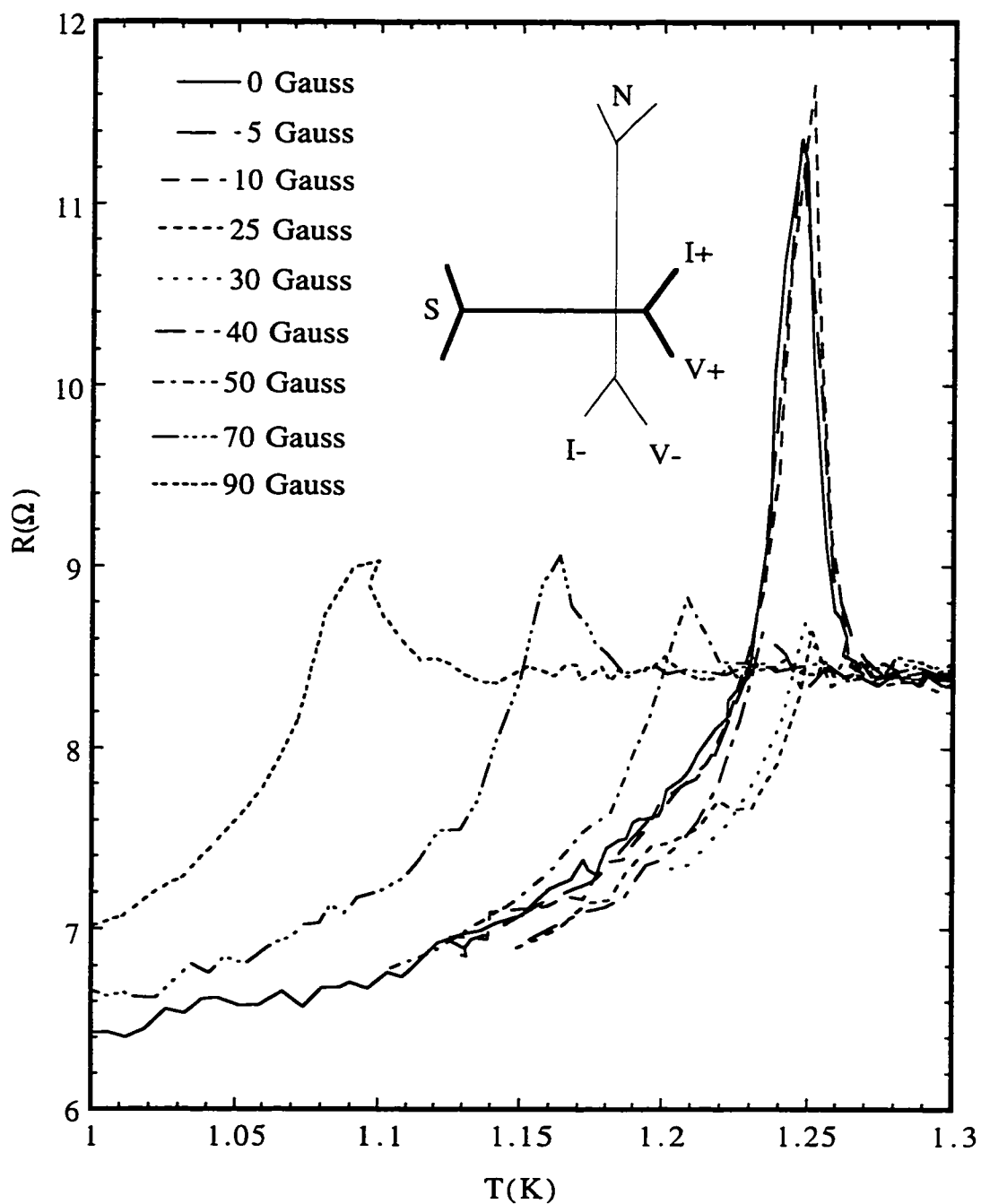


Fig. 4.4.5  $R(T)$  measured at different finite magnetic fields  $H$  for the measurement configuration shown in the inset. The data shows reentrant behavior at  $H = 40$  gauss.

leads to the relaxation of charge imbalance in 1D NS systems.

## 4.5 Charge imbalance in a 1D NS hybrid loop

Recent research on the proximity effect on mesoscopic systems [10-17, 40-44] has motivated us to fabricate several mesoscopic NS hybrid loops which contain a normal-metal arm and a superconducting arm. In one of these samples we also observed effects similar to charge imbalance as is expected in any NS system. We present some of the data regarding charge imbalance in this section. Fig. 5.1.1 shows a SEM picture of one of the samples, as well as schematics of two of the loops. The sample properties are discussed in Chapter 5. Chapter 5 concentrates on the low temperature ( $T < T_c$ ) and low bias ( $I < I_c$ ) behavior of the samples. Here we discuss measurements of these samples in the charge imbalance region.

### 4.5.1 Negative $dV/dI$ in the NS hybrid loop

Fig. 4.5.1(a) shows two traces of the differential resistance  $dV/dI$  as a function of dc current at  $T = 30$  mK for sample B of Fig. 5.1.1. The measurement configuration is shown in the inset. The measurement technique is the same as that described in Chapter 2. A slight difference here is that we impose two ac signals of different frequencies on the dc current so that by lock-in detecting these two signals at different reference frequencies, we can measure simultaneously  $dV/dI$ 's corresponding to the two configurations shown in the plot. At zero current, the top curve in Fig. 4.5.1(a) shows an enhancement of  $dV/dI$  due to the reentrance effect [12-17], which will be discussed in Chapter 5. This enhancement, which is also observed in the bottom curve of Fig. 4.5.1(a), is not clearly seen in the curve

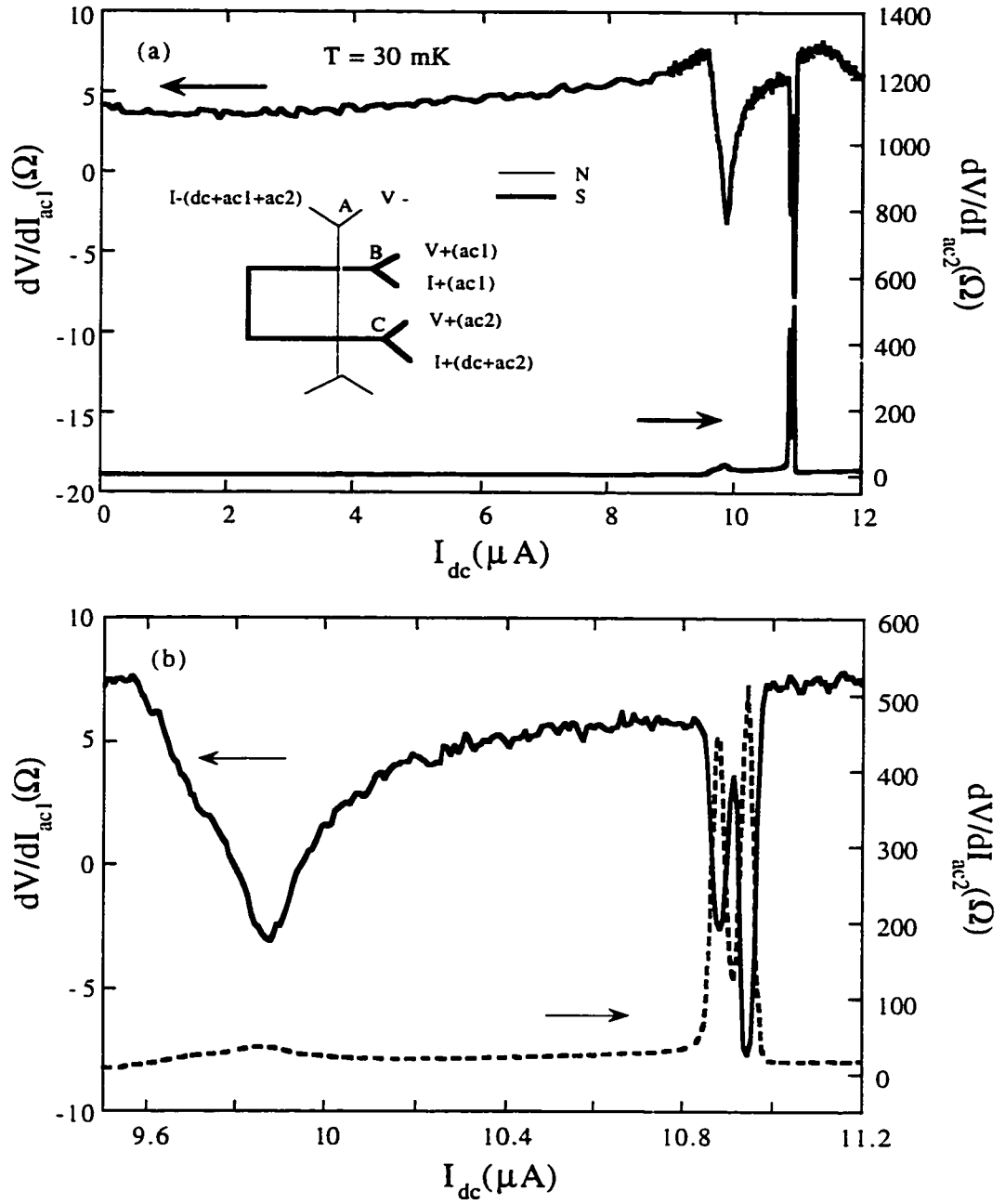


Fig. 4.5.1 Negative differential resistance  $dV/dI$  as a function of dc current  $I_{dc}$  at  $T = 30$  mK observed in a NS hybrid loop whose schematic is shown in Fig. 5.1.1 (b) shows an expanded region of the data in (a).

because of the large scale of the plot. At a current near  $10\ \mu\text{A}$ , the top curve clearly shows a negative  $dV/dI$  dip. Following this dip, two dips close to each other are observed again between  $10.8$  and  $11\ \mu\text{A}$ . Fig. 4.5.1(b) shows the enlarged plot of the two curves between  $9.6$  and  $11.2\ \mu\text{A}$ . One should note the difference between the two measurement configurations is that top curve represents a less conventional  $dV/dI$  of the segment between point A and B since the dc and ac current do not follow the same path while the bottom curve represents  $dV/dI$  of the segment between A and C. The general behavior of the two traces of  $dV/dI$  curves are: (i) The amplitudes and positions of these peaks and dips change upon thermal cycling. This may be due to the property of the NS interface. (ii) One difference between the first peak (dip) and the group of second and third peaks (dips) is that the first peak (dip) is much more stable than the second and third peaks (dips). In our experience, upon carrying out many measurements, the two traces show a sudden transition to normal state resistance between the first and second peaks (dips), indicating the second and third peaks are in a metastable state and are sensitive to external factors such as temperature or magnetic field. This behavior is shown in Fig. 4.5.2(a). The two  $dV/dI$  curves correspond to the same measurement configuration for the bottom curve in Fig. 4.5.1(a) (but sweeping dc current in the opposite direction). While using the same measuring techniques, the dotted curve of Fig. 4.5.2(a) has a sudden transition to a low  $dV/dI$  value between  $-10$  and  $-11.2\ \mu\text{A}$  instead of developing two sharp peaks as in the solid curve. We will return to discuss this metastability in detail later. (iii) Both the positions and amplitudes of the peaks and dips are sensitive to a small magnetic field, being periodic as a function of the flux threading the hybrid loop with a period equal to a flux quantum corresponding to the area of the loop. (iv) Both the positions and amplitudes of

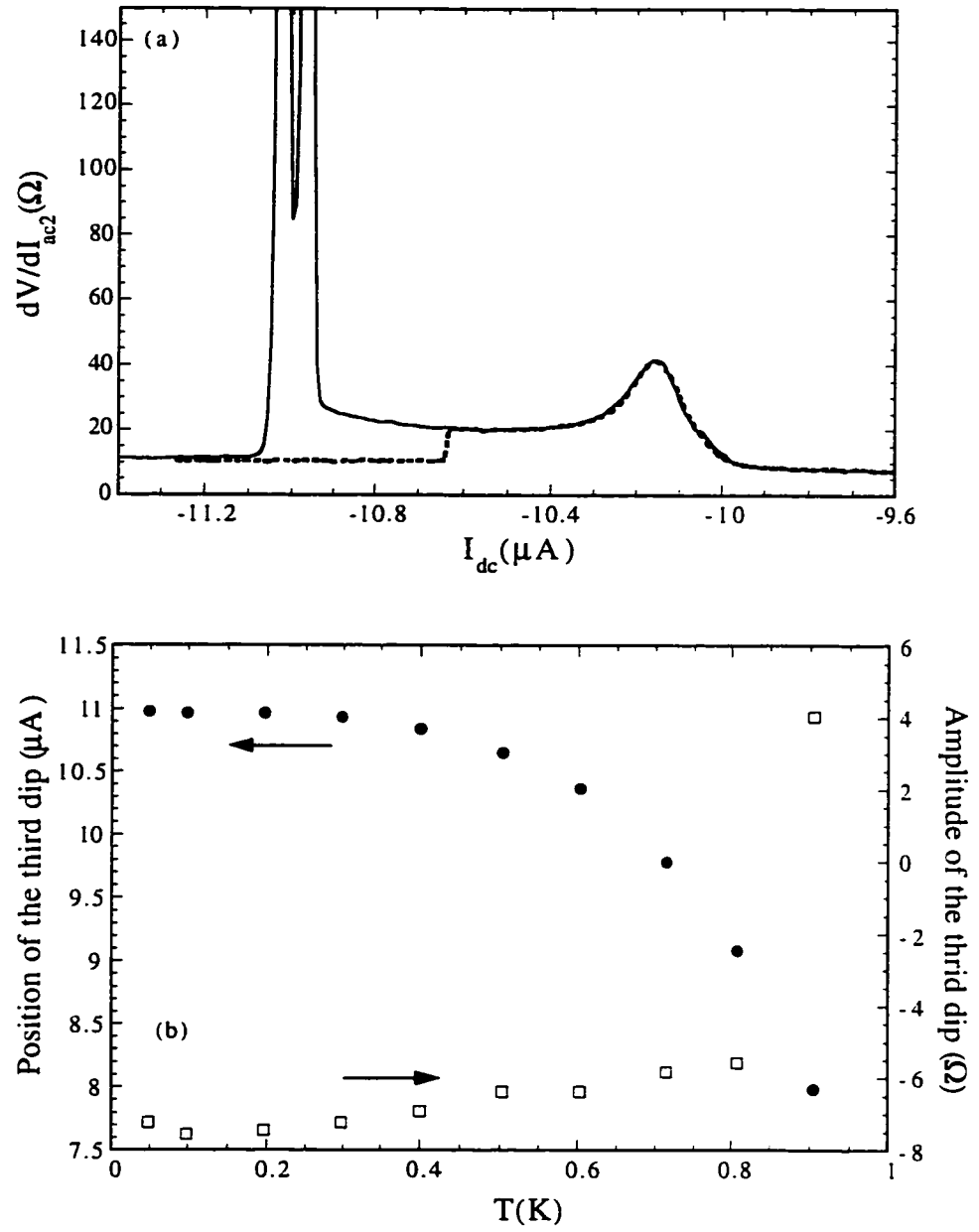


Fig. 4.5.2 (a) Shows the instability of the bottom curve of Fig. 4.5.1(a). Occasionally, while ramping the current, the curve traced dotted line rather than the solid curve. (b) Position (filled circle) and amplitude (open square) of the third dip in the top curve of Fig. 4.5.1(a) as a function of temperature.

the peaks and dips are strongly temperature dependent, showing behavior similar to the temperature dependence of either the superconducting energy gap  $\Delta(T)$ . Fig. 4.5.2(b) shows the position and the amplitude of the third dip as a function of temperature for the top curve of Fig. 4.5.1(a). Both the position and the absolute value of the amplitude show a slight decrease as the temperature is increased from the lowest temperature and decrease rapidly at temperatures close to  $T_c$  (1.15 K).

#### 4.5.2 Coherence effect in the NS hybrid loop

Although our interpretation of the negative  $dV/dI$  is somewhat hindered by the normal arm in the hybrid loop, the existence of this normal arm, on the other hand, provides information for examining the phase sensitivity of the negative differential resistance. When two NS interfaces are involved in the sample, an additional effect resulting from the phase of the superconductor becomes apparent. This can be observed by applying a magnetic field to modulate the phase difference between the two NS interfaces. Fig. 4.5.3(a) shows the plot for the amplitude and the position of the third negative  $dV/dI$  dip of Fig. 4.5.1 as a function of magnetic field  $H$  at  $T=30$  mK. Both curves show clear periodic oscillations as a function of the magnetic field. The period of oscillations is equal to one flux quantum corresponding to the area of the NS hybrid loop. Similar results are observed in other samples. Fig. 4.5.3(b) shows  $dV/dI$  for sample A of Fig. 5.1.1, along with the oscillations of the amplitude of one of the resistive peaks. This result implies an interesting effect: If the negative  $dV/dI$  observed in our sample is due to an excess voltage in the charge imbalance region, these oscillations then suggest that at least part of this excess voltage is phase coherent, which in turns suggest that part of the pair chemical potential is phase sensitive. To our knowledge, this property has not been observed in the

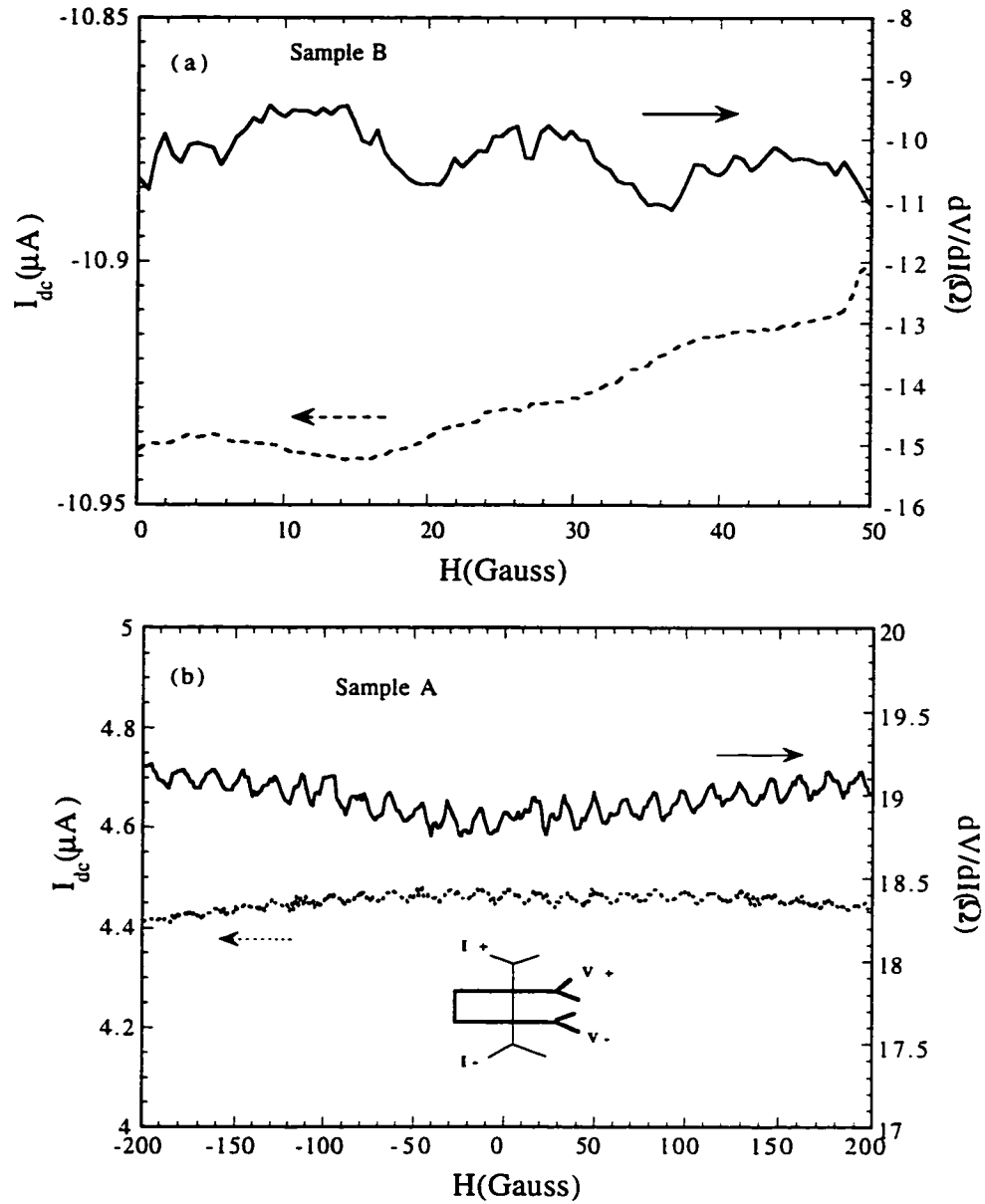


Fig. 4.5.3 Amplitude (solid curve) and position (dotted curve) as a function of magnetic field at  $T = 30$  mK for (a) for sample B of Fig. 5.1.1 with negative  $dV/dI$  (the third dip of Fig. 4.5.1(a)) (b) for sample A of Fig. 5.1.1 with the  $dV/dI$  measurement configuration shown in the inset. Both curves clearly show periodic oscillations with a period of a flux quantum corresponding to the area of the NS hybrid loop.



charge imbalance regime.

#### 4.5.3 Metastability of the differential resistance

We finally present data showing the metastability of the peaks and dips in the differential resistance. The negative differential resistance we observed, if it due to the charge imbalance, suggests the existence of PSCs in our sample. As described in the previous section, PSCs can be thermally activated at high temperatures. Furthermore, the second and third peaks (dips) show unstable behavior (see Fig. 4.5.2(a)). The rather strong temperature dependence of these negative  $dV/dI$ 's (both amplitude and position) and the metastability of the second and third negative dips motivated us to investigate the  $dV/dI$  metastability at different temperatures.

Fig. 4.5.4 shows five traces of the amplitude of the second  $dV/dI$  dip as a function of time at various temperatures. The traces of Fig. 4.5.4 were measured by biasing the dc current at the second dip of Fig. 4.5.1. For clarity, each curve is shifted up by  $5 \Omega$ . The resistance of the dip switches between two values. As one can see, at low temperatures, only few switching events take place. As the temperature is raised, more switching events are observed in the same period of time. Above 700 mK (the data are not shown here), the switching is so frequent that we could not bias at the dip any more. Each switching event seems to occur between two metastable states based on the fact that the amplitude of the switching is temperature independent. This suggests that there may exist an energy barrier similar to the condensate energy in the case of phase-slip event [18] for a switching event to occur. At present, the origin of this bistability is still not clear due to the difficulty in analyzing the complicated geometry of the sample.

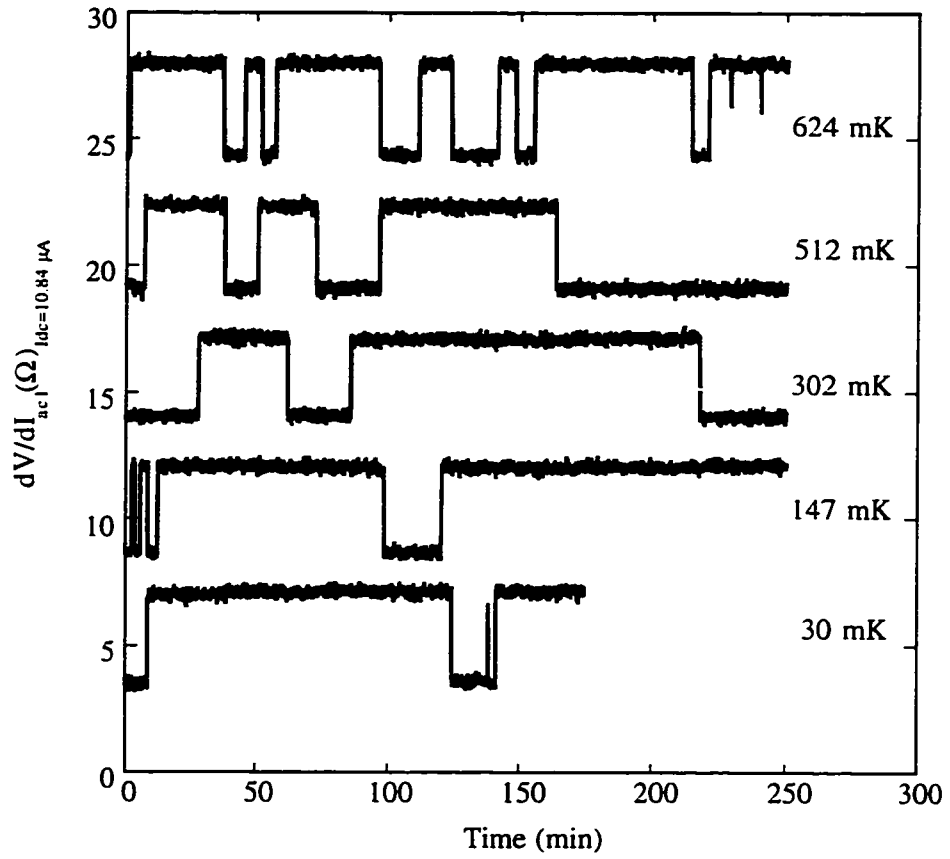


Fig. 4.5.4 Differential resistance of the second dip in  $dV/dI_{ac1}$  of Fig. 4.5.1 (at  $I_{dc} \sim 10.84 \mu A$ ) as a function of time for five different temperatures. Curves are offset by 5  $\Omega$  from each other for clarity.

In summary, we have successfully created a PSC in 1D Al samples with external parameters, a rf signal and a magnetic field, to induce a resistance anomaly in the sample. In the former, the location of the PSC is not well controlled by the rf signal while in the latter, the location of PSC is clearly determined by the local suppression of the order parameter ( $T_c$ ) in the sample via the aid of a magnetic field. We have also shown that the resistance anomaly can arise from the simple mixing of the measuring current and a “noise” signal, raising the possibility of an external origin of the resistance anomaly. The detailed comparison between the rf and noise induced resistance anomaly suggests that the rf induced resistance anomaly is due to an intrinsic property of a nonequilibrium superconductor. The microscopic mechanism responsible for the rf induced resistance anomaly needs to be investigated further.

In our investigations of charge imbalance in 1D NS systems, we have observed several interesting results including: a relatively short charge imbalance length in a 1D superconductor compared with previous results, multiple negative  $dV/dI$  dips in the system where only one pair of voltage probes exist, a reentrance of the resistance anomaly at high magnetic field, metastable negative dips in a NS system containing two NS interfaces, phase-sensitivity of the metastable negative dips, and two level switching behavior of the metastable negative dips.

## Chapter 5

### Anomalous Proximity Effect

In the last chapter, we discussed nonequilibrium superconductivity in pure superconductors and in superconducting wires near a NS boundary. In this chapter we turn to the normal-metal side of a NS boundary. The relevant physics is the so-called proximity effect [18, 33, 34], in which superconductivity can penetrate into the normal metal by inducing pair correlations across the NS boundary. The unique behavior of the proximity effect presented here is that the conductance enhancement is *suppressed* at temperatures far below  $T_c$ , which is in contrast to the conventional understanding of the proximity effect, in which the conductance enhancement increases monotonically as the temperature is lowered.

Conventionally, the proximity effect was observed in a normal metal layer of few thousand angstroms sandwiched between two superconductors [29-32]. Behavior such as a finite supercurrent across the sandwich and zero resistance have been observed in such SNS structures, confirming the existence of superconductivity induced in the normal metal. It is generally accepted that the microscopic mechanism responsible for the proximity effect is Andreev reflection [36]. Recently, the effect has been observed in 1D normal metal wires which are several microns long. A finite supercurrent can still be sustained in such a long 1D N wire [12-14, 40]. A striking result was observed which showed the resistance of the normal metal *increases* at very low temperatures, the so-called *reentrance effect* [12-17].

These strange results have motivated the study of the proximity effect at

temperatures far below  $T_c$ . That the resistance of a diffusive normal metal adjacent to one or more superconductors regains its normal state resistance at zero electron energy and temperature, the so-called reentrance effect, was first predicted by S. N. Artemenko, A. F. Volkov, and A. V. Zaitsev [46]. Based on the impurity-averaged quasiclassical Green functions technique [46-53], theoretical analysis shows that electrical transport in a normal metal connected to a superconductor can be described by an effective diffusion coefficient  $D(\epsilon, \mathbf{r})$ , which is energy and position dependent [50, 52-53]. This is one manifestation of the change in electron states of the normal metal induced by proximity to a superconductor. The surprising feature of the prediction is that the conductance enhancement nominally vanishes at zero temperature and zero energy despite the presence of superconducting correlations.

We present here the results of the measurement on the transport properties of two mesoscopic hybrid loops composed of a normal-metal arm and a superconducting arm. The samples differed in the transmittance of the normal/superconducting interfaces. While the low transmittance sample showed monotonic behavior in the low temperature resistance, magnetoresistance and differential resistance, the high transmittance sample showed so-called reentrant behavior in all three measurements. A simulation based on quasiclassical Green functions theory is performed to compare with the experimental results.

## 5.1 Reentrance Effect

Consider the case of a normal-metal wire of length  $L$ , connected to a normal reservoir at

one end and a superconducting reservoir at the other. Based on the theory of quasiclassical Green functions, under the limit  $k_B T, eV \ll \Delta$ , the Thouless energy  $E_c = \hbar D/L^2$  becomes the characteristic energy of the system, where  $D$  is the electron diffusion coefficient. The manifestation of the reentrance effect in experimental measurements of transport phenomena includes : (1) The zero-bias resistance of the normal metal as a function of temperature decreases from its normal state resistance  $R_N$  at  $T = 0$  as  $T$  is increased, reaches a minimum at  $k_B T \sim E_c$ , and returns to  $R_N$  at a higher temperature. (2) The zero-temperature resistance of the normal metal as a function of the voltage  $V$  biased between the normal and superconducting reservoirs shows the same behavior as (1) except  $k_B T$  is replaced by  $eV$ . (3) The amplitude of both zero-bias magnetoresistance oscillations and the zero-temperature magnetoresistance oscillations of an Andreev interferometer shows an *increase* from zero at  $T=0$  and  $V=0$  respectively, reaches its *maximum* at  $k_B T, eV \sim E_c$ , and vanishes at higher  $T$  and  $V$  respectively.

#### 5.1.1 Sample properties and measurement setup

We have observed the reentrance effect in hybrid loops containing a N arm and a S arm (NS loop) as well as a structure composes of a 1D N wire connected to a 1D S wire (NS wire). Here we present primarily the results of experiments on two NS loops (sample A and sample B). The primary difference between the two samples is in the NS interfaces. Sample B contains interfaces of much higher transmittance than sample A. An electron beam micrograph of the sample studied (sample A) is shown in Fig. 5.1.1(a), and schematics of the two samples are shown in Fig. 5.1.1(b). The samples were fabricated by

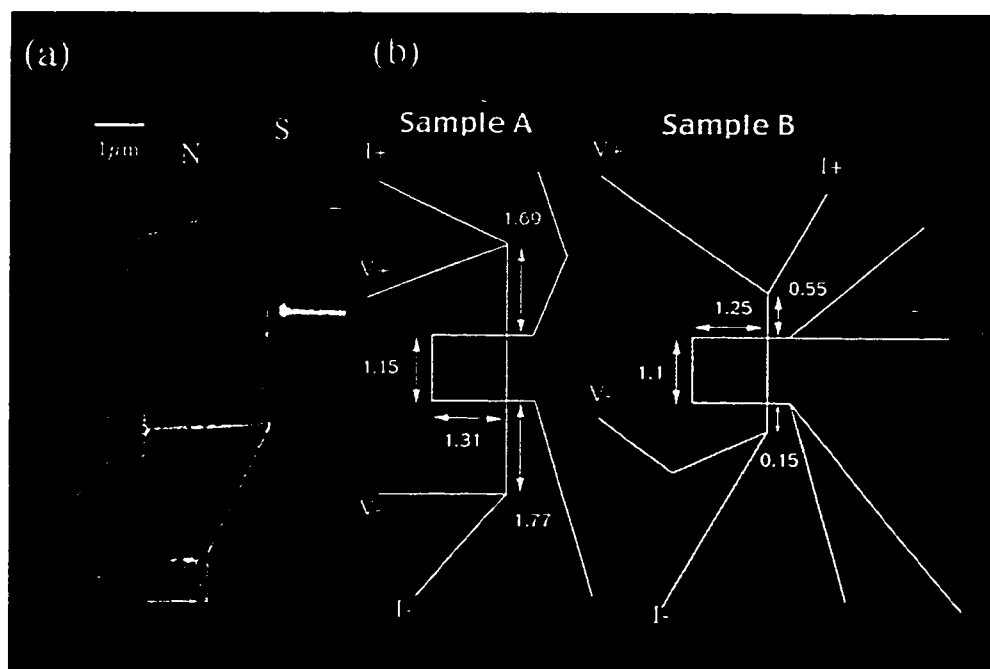


Fig. 5.1.1 (a) Scanning electron micrograph of sample A. The additional gate electrode was kept grounded and not used in these measurements. (b) Sample schematics for the two samples. The dimensions are indicated in  $\mu\text{m}$ . The leads used to apply ac currents and measure the voltages are also shown in the schematics. For the  $dV/dI$  measurements, an additional dc current is applied through  $I_{+/-}$ .

conventional multilevel electron-beam lithography described in detail in Chapter 3. Controlled Ag and Al wires were coevaporated with sample B in order to calibrate film properties. The relevant film parameters are as follows: Au/Ag thickness  $\sim 28$  nm, Al thickness  $\sim 37$  nm, wire linewidth  $\sim 0.1 - 0.14$   $\mu\text{m}$ , normal metal (Ag) coherence length  $\xi_N(T) \sim 0.23 \mu\text{m}/T^{1/2}$ , superconducting coherence length  $\xi_{Al}(T=0) = 0.31 \mu\text{m}$ , and electron phase coherence length  $L_\phi = 0.9 \mu\text{m}$  at  $T=30$  mK [107]. The measurements were performed in a dilution fridge between 30 mK and 1.5 K using a four-terminal ac resistance bridge, with ac excitations in the range of 10-100 nA to prevent heating (see Chapter 3). The four terminal measurement configuration is shown in Fig 5.1.1(b). For the  $dV/dI$  measurements, the dc current was applied through the same leads as the ac current before the total current was sent into the resistance bridge circuit. An EG&G PAR 124A lock-in amplifier was used to detect the ac response (see Chapter 3 for details). The highest frequency used was 103 Hz and no difference was observed for different frequencies.

### 5.1.2 Reentrance effect in $R(T)$

Fig. 5.1.2 shows the normalized resistance ( $R/R_N$ ) as a function of temperature  $T$  for the two samples. Sample A has a small drop in  $R$ , followed by a gradual decrease down to 30 mK. Sample B, in contrast, has a sharp decrease at  $T_c$ , reaches a minimum at  $T \sim 520$  mK, and eventually *increases* as the temperature is lowered still further. The sharp drop in resistance of sample B near  $T_c$  results from the fact that its NS interfaces are highly transparent and therefore the superconducting arm shorts out the normal arm of the loop. Sample A, on the other hand, possesses lower NS interface transparencies and therefore



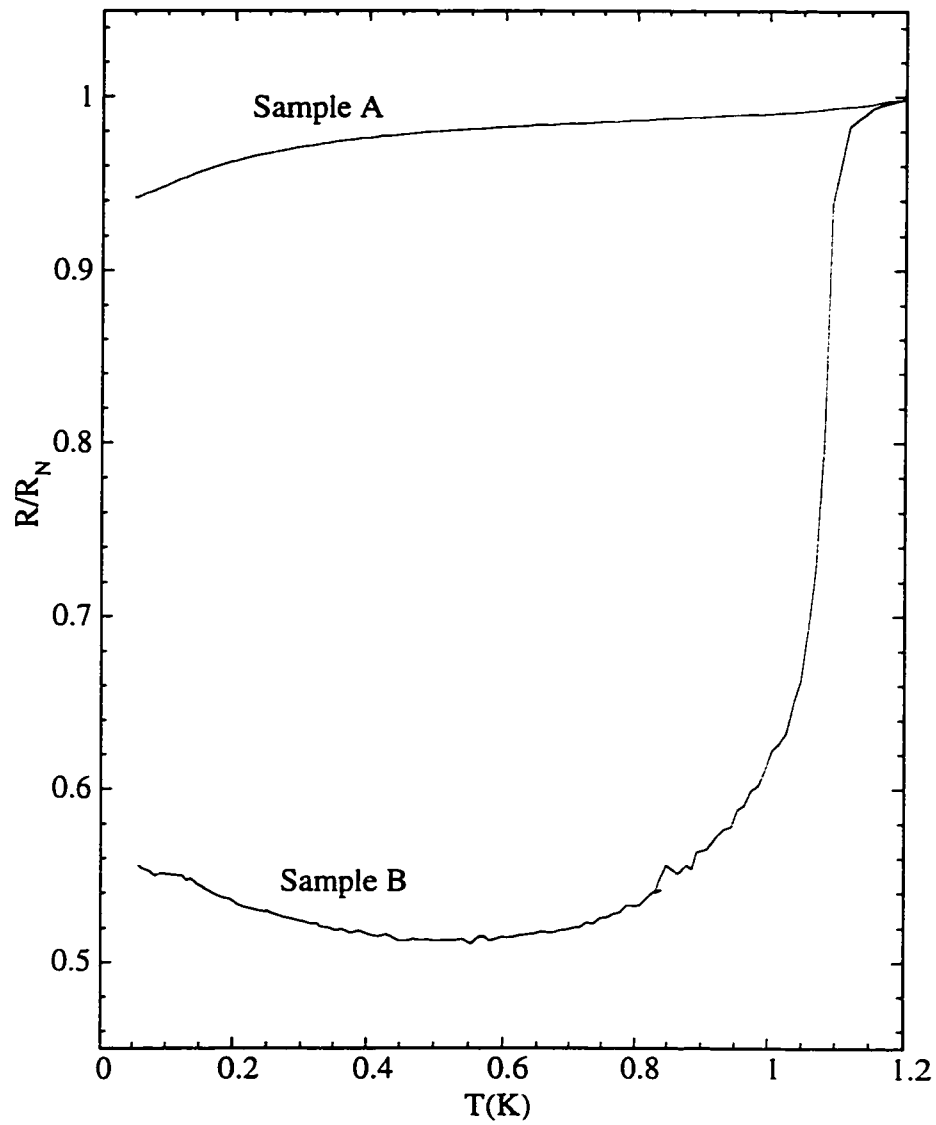


Fig. 5.1.2 The normalized resistance  $R/R_N$  as a function of temperature  $T$ .  $R_N = 67.5 \, \Omega$  and  $10.3 \, \Omega$  for samples A and B respectively.

only shows a small decrease near  $T_c$ . The resistance at the lowest temperature is  $5.95 \Omega$ .

Using the resistivity of the coevaporated Ag wire we obtain the resistance of the side branches to be  $\sim 7 \Omega$  at 4.2 K, close to  $5.95 \Omega$ . Therefore, the resistance almost reaches its normal state value.

Before introducing a detailed numerical calculation based on the theory predicted in Chapter 2, we can make some rough qualitative comparisons to the experiment. We rewrite Eq. 2.4.18 in the form,

$$\sin[\theta_{s0} - \theta_{N0}] \sim \frac{R_b}{R_N} \partial_x \theta(x, \epsilon) \quad (5.1.1)$$

where  $\theta_{s0}$  and  $\theta_{N0}$  denote the value of  $\theta$  at the superconducting and normal sides of the NS interface ( $x=0$ ) respectively. If we assume  $\epsilon \ll \Delta$ , and that the superconducting reservoir is not affected by the normal wire significantly, then  $\theta_{s0} = \theta_s = \pi/2$  according to Eq. 2.4.19(b), where  $\theta_s$  is the value of  $\theta$  far inside the superconducting reservoir. For the very high transmittance case,  $R_b/R_N \sim 0$ , and  $\theta_{N0} = \theta_{s0} = \pi/2$ .  $\theta$  in the normal metal has its maximum value at the NS boundary. In contrast, if  $R_b/R_N > 1$ , then the argument of  $\sin\theta$  reaches its limiting value and  $\theta_{N0} = \theta_{s0} - \pi/2 = 0$ . Therefore  $\theta$  becomes zero at the NS boundary. Consequently, the proximity effect in the normal metal is minimized. This is

consistent with what we observe in our samples. The resistance of each NS interface is  $\sim 25 \Omega$  for sample A and  $< 0.5 \Omega$  for sample B. Consequently,  $R_b/R_N > 1$  for sample A and  $R_b/R_N \ll 1$  for sample B. Hence, one expects the proximity effect to be smaller in sample A, which is consistent with the data shown in Fig. 5.2.2.

We can roughly estimate the temperature  $T_{\min}$  at which the maximum proximity effect occurs in sample B. Since  $\theta$  decays over a characteristic length  $\sim (\hbar D/\epsilon)^{1/2}$  and the reentrance shows up when the normal-metal coherence length  $\xi_N$  is comparable to the length of the sample  $L$ , on substituting  $\epsilon$  with  $k_B T$ , one obtains  $T_{\min} \sim \hbar D/k_B L^2$ . Furthermore, the longer N side branch dominates the reentrant behavior since it contributes the larger resistance. Inserting the length of longer side branch for  $L$ , one obtains  $T_{\min} \sim 176$  mK, which is a factor of 3 lower than the temperature at which we observed the minimum in resistance in Sample B.

In order to compare this result with the theory in detail, we now apply the quasiclassical Green functions theory to simulate our sample geometry. The parameterized Usadel equation described in Chapter 2 is further simplified if the gap  $\Delta$  in the normal metal is assumed to be zero, and inelastic scattering mechanisms are neglected:

$$\frac{\partial^2 \theta(\epsilon, x)}{\partial x^2} + 2i\epsilon \sin \theta(\epsilon, x) = 0 \quad (5.1.2)$$

This equation is solved with the boundary conditions provided in Chapter 2, i.e.,  $\theta(\epsilon, x) = 0$  in the N reservoir. In the S reservoir,

$$\theta(\epsilon, x) = \frac{\pi}{2} + i \frac{1}{2} \ln \frac{\Delta + \epsilon}{\Delta - \epsilon} \quad \text{for } \epsilon < \Delta, \quad (2.4.19b)$$

$$\theta(\epsilon, x) = i \frac{1}{2} \ln \frac{\epsilon + \Delta}{\epsilon - \Delta} \quad \text{for } \epsilon > \Delta. \quad (2.4.19b)$$

Since the voltage leads are one dimensional with respect to the coherence length ( $w \ll \xi_N$ ), the boundary condition at a node where two normal wires intersect is determined by a Kirchoff-like equation resulted from the conservation of spectral current [52]:

$$\sum_i S_i \frac{d\theta_i(\epsilon, x)}{dx} = 0 \quad (5.1.3)$$

where  $S_i$  is the cross section of the  $i$ th wire.

To solve the transport problem, we need to solve the equation of motion for the Keldysh Green function  $\check{G}^K$  (see Eq. 2.4.7(a) of Chapter 2). Here we follow the procedures elaborated in Refs. 48, 50, 52 and use the simple geometry of a N reservoir connected to a S reservoir by a normal wire of length  $L$ . In the absence of supercurrent and pair potential,  $f_0$  and  $f_3$  are decoupled and we obtain a simplified equation for an effective

diffusion coefficient  $D(\epsilon, x)$ :

$$\frac{d}{dx} \left[ D(\epsilon, x) \frac{df_3(x, \epsilon, V, T)}{dx} \right] = 0 \quad (5.1.4)$$

where we have written  $f_3$  explicitly in terms of position  $x$ , electron energy  $\epsilon$ , bias voltage  $V$  and temperature  $T$ .  $D(\epsilon, x)$  has the following form [48]:

$$D(\epsilon, x) = D \cosh^2 [\text{Im}\theta(\epsilon, x)] \quad (5.1.5)$$

with  $D = v_F \ell / 3$ , the normal state diffusion coefficient. Assuming the normal reservoir N is biased at a voltage  $V$  and the superconducting reservoir is biased at zero voltage. Eq. 5.1.4 is then solved with the boundary conditions for the even distribution function  $f_3$  (see Sec. 2.4.2):

$$f_3 = 0 \quad \text{in the S reservoir} \quad (2.4.15a)$$

$$f_3 = \frac{1}{2} \left( \tanh \frac{\epsilon + eV}{2k_B T} - \tanh \frac{\epsilon - eV}{2k_B T} \right) \quad \text{in the N reservoir} \quad (2.4.15b)$$

The solution for  $f_3(x)$  is straightforward:

$$f_3(x, \epsilon, V, T) = \frac{1}{2} \left( \tanh \frac{\epsilon + eV}{2k_B T} - \tanh \frac{\epsilon - eV}{2k_B T} \right) \frac{\int_0^x \cosh^{-2} [\text{Im}\theta(\epsilon, x)] dx}{\int_0^L \cosh^{-2} [\text{Im}\theta(\epsilon, x)] dx} \quad (5.1.6)$$

The current flowing out of the N reservoir is proportional to  $f_3'(L, \epsilon, V, T)$  [50].

Summing the contribution from all electron energies we finally obtain a formula for the total current  $I(V, T)$  flowing out of the normal reservoir biased at a voltage  $V$  relative to the superconducting reservoir at temperature  $T$  [48, 52, 53]:

$$I(V, T) = \frac{1}{2R_N} \int_0^\infty d\epsilon \left[ \tanh\left(\frac{\epsilon + eV}{2k_B T}\right) - \tanh\left(\frac{\epsilon - eV}{2k_B T}\right) \right] D(\epsilon) \quad (5.1.7)$$

where

$$D(\epsilon) = \frac{1}{L \int_0^L dx \text{sech}^2 [\text{Im}\theta(\epsilon, x)]} \quad (5.1.8)$$

The first term of Eq.5.1.7 takes into account thermal smearing at finite temperature while the second term describes the correction from the proximity effect.

We now apply these equations to the geometry of Sample B. Fig. 5.1.3(a) shows a

schematic of Sample B. We assume that the NS interfaces are perfect, so that the loop resistance is zero, being shorted by the superconducting arm. The measured normal-metal resistance  $R$  is then simply the sum of the two N side branches,  $R_1$  and  $R_2$ , with length  $L_1$  and  $L_2$ , where  $L_i$  is the length of the arm from the superconductor to the point at which the voltage probe joins the wire. To determine the proximity effect resistance, we need to solve the Usadel equation in the 1D wires on either side of the loop. We make the following assumptions in the simulation: (i) Since the electron phase coherence length  $L_\phi$  places an upper cutoff to the pair correlation in the normal metal, we take the normal reservoirs to be at a distance  $L_\phi$  from the superconductor. (ii) The upper limit of the integral in Eq. 5.2.8 is  $L_i$  ( $i=1, 2$ ), but not  $L_\phi$  due to the following reason. Since the voltage leads are not placed at the N reservoir, the electrochemical potential measured is not equal to the voltage drop between the N and S reservoir. Fortunately, the variation of the potential with the position was shown not to deviate far from a linear form [50]. Therefore we can relate the voltages measured at each probe by a linear scaling of the form  $V_i = V(L_i/L_\phi)$ , where  $V$  is the corresponding normal reservoir, and the voltage at the superconducting loop is zero. (iii) We do not take into account the interference of the voltage probes on the boundary condition of Eq. 5.1.3. Taking the effect of the voltage leads into account provides only a minor correction to the results.

Figure 5.1.3(b) shows the final simplified NSN geometry that we simulated. The total temperature dependent resistance of the sample is the sum of the resistances  $R_1(T)$  and  $R_2(T)$ . To determine the temperature dependent resistance of each N side branch, we can take the derivative of  $I(V, T)$  with respect to voltage  $V$  and obtain  $G(V, T) = dI/dV$ . The

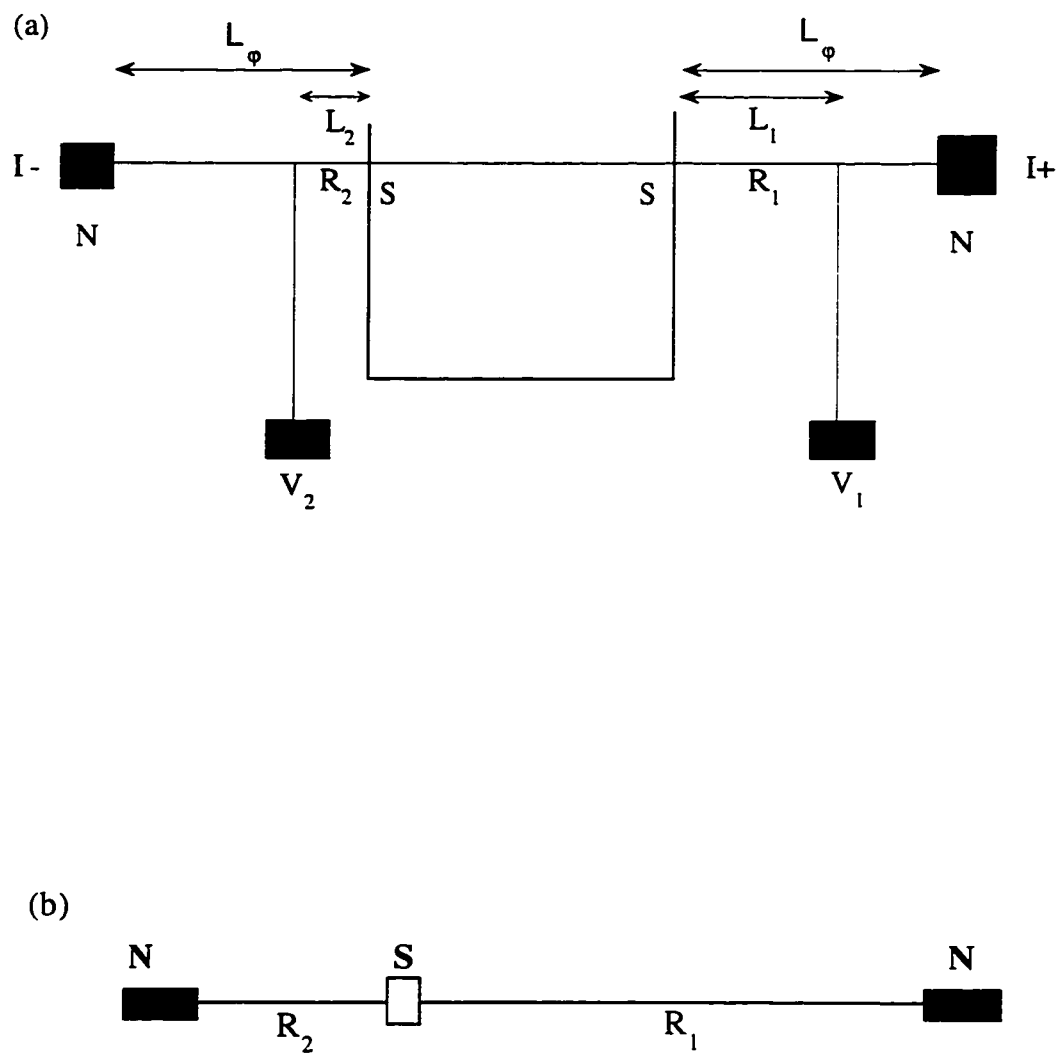


Fig. 5.1.3 (a) Schematic of the simulated model. The total current is assumed to flow into the superconducting part of the hybrid loop, so the simplified model is equivalent to a N-S-N geometry (b).



resistance is then obtained from:  $R(V, T) = G^{-1}(V, T)$ . At zero bias, the calculation is simplified. To first order in  $V$ , the following formula is obtained.

$$R(T) = R_N \left[ \int_0^\infty \frac{d\epsilon}{2k_B T \cosh^2 \frac{\epsilon}{2k_B T}} \frac{1}{\frac{L}{T} \int_0^L \cosh^{-2} [\text{Im}\theta(\epsilon, x)] dx} \right]^{-1} \quad (5.1.9)$$

Figure 5.1.4(a) shows  $R_1(T)$ ,  $R_2(T)$ , and the sum  $R_1(T) + R_2(T)$  calculated in the limit  $\Delta \gg E_c$  in the temperature regime below 1 K. As expected  $R_1$  dominates the contribution to the reentrance effect.  $R_2$ , on the other hand, decreases as temperature is raised from zero but never reaches the minimum within the whole temperature range. Its contribution to  $R$  is to lower the total minimal resistance and to *slow down* the tendency of returning to the total normal state resistance  $R_N$ . To calculate  $\theta(\epsilon, x)$  we have assumed  $\Delta$  is much larger than all the energies integrated in Eq. 5.1.9. For the temperature range of interest, it is good enough to integrate up to  $100 E_c$ . We now examine how the value of  $\Delta$  effects the calculation. Fig. 5.1.4(b) shows the result of the calculation for the total resistance using two different values of  $\Delta$ . In the case of  $\Delta \gg 100 E_c$  the curve recovers its normal state value *faster* than the curve obtained from the case where  $\Delta$  is close to  $100 E_c$  at high temperature. On the other hand, at temperatures less than  $5 E_c$ , where the theory is usually applied, the results do not show any significant difference. Therefore, we

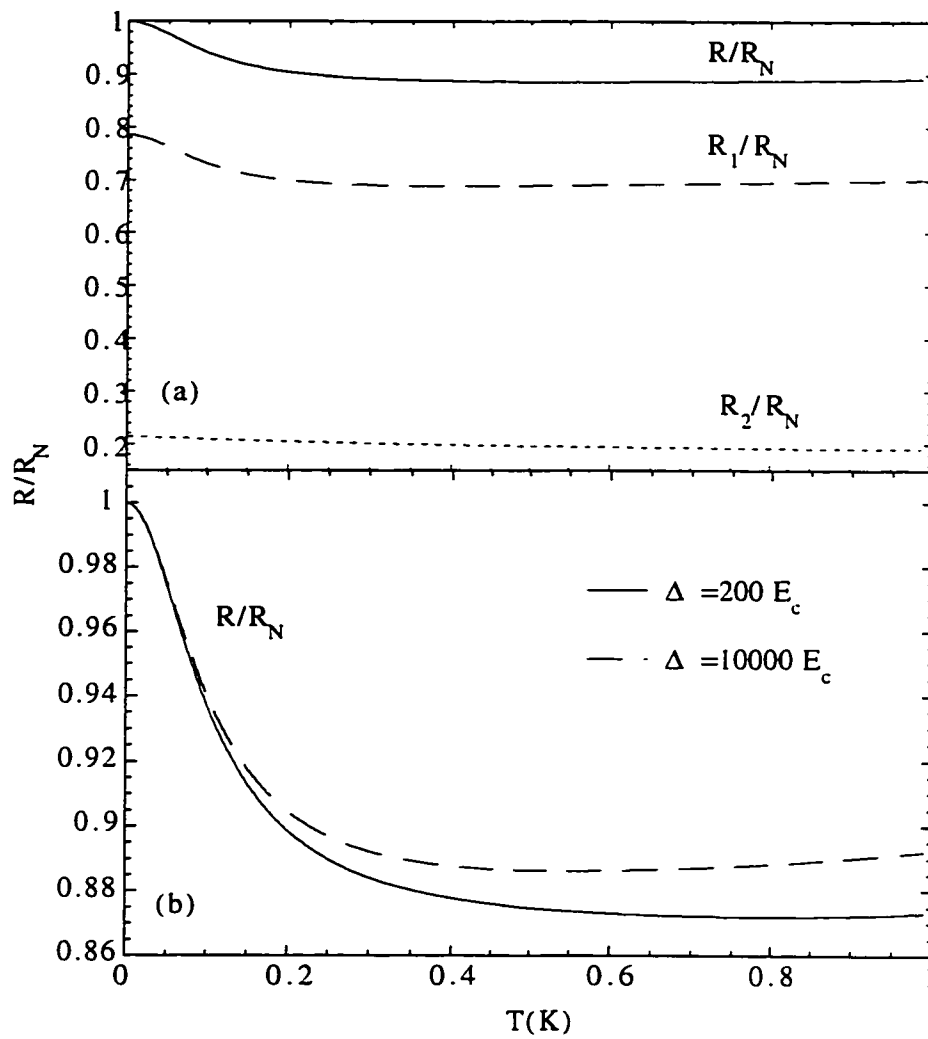


Fig. 5.1.4 Simulation of the resistance as a function of temperature based on model in Fig. 5.3.1. (a) Resistance as a function of temperature for  $R_1$ ,  $R_2$  and  $R=R_1+R_2$ . Assume  $\Delta \gg E_c$ . (b) Total resistance  $R$  as a function of  $T$  for different  $\Delta$ 's.  $\Delta = 200 E_c$ ,  $10000 E_c$  for solid curve and dashed curve respectively.

assume  $\Delta=10^4 E_c$  in the calculation since this retains the behavior at low temperature while giving a result closer to the measurement at high temperatures.

Comparing the result in Fig. 5.1.4(a) with  $R(T)/R_N$  in Fig. 5.1.2, one finds a large discrepancy at temperatures close to  $T_c$ . To resolve this problem, we note the total resistance measured in  $R(T)$  contains the contribution from the S part of the hybrid loop as well. At temperatures close to  $T_c$ , this contribution becomes important due to the broad superconducting transition of the sample. In pure superconducting samples, one mechanism that leads to finite resistance just below the superconducting transition is thermal activation of phase-slip centers. Phase-slip events are well known to be responsible for the transition in  $R(T)$  from the normal to the superconducting state. The resistance broadening due to these phase-slip centers is given by the Langer-Ambegaokar (LA) equation [18]:

$$R = \frac{\alpha}{T} \exp \left[ \beta \left( 1 - \frac{T}{T_c} \right)^{3/2} / T \right] \quad (5.1.10)$$

where  $\alpha$  is a parameter associated with the attempt frequency for a phase slip event, and  $\beta$  is a parameter related to the energy barrier for a phase slip event. For pure superconducting wires,  $\beta$  is typically very large ( $\sim 10^6$ ), which confines the broadening of the transition to a few millikelvin near  $T_c$ . For our N-S structures,  $\beta$  is expected to be much smaller, since the transition is much broader.

Fig. 5.1.5 shows the comparison of the experimental result with a combined theory of quasiclassical Green functions and the LA formula. Eq. 5.1.10 was fitted to the difference between data and the  $R(T)$  curve in Fig. 5.1.4(a) using  $\alpha$  and  $\beta$  as fitting parameters. For this fit,  $\alpha=0.17 \text{ } \Omega\text{K}$  and  $\beta=9.3 \text{ K}$ . One can see the phase-slip events (dashed curve) dominate at temperatures close to  $T_c$ , and vanish quickly at temperatures of the order of  $E_c$ . In contrast, the reentrance effect based on the Usadel Eq. (dotted curve) dominates at very low temperature. The solid line shows an excellent fit to data combining both the Usadel equation and the LA formula.

Even with this analysis, however, it is not clear that the drop in resistance near  $T_c$  is due to phase phase-slip centers in the superconductor, especially since this does not account for the bias dependence of the differential resistance discussed in the next section. It is clear, however, that the resistance drop is not associated with the proximity effect in the normal metal which is dominant at lower temperatures.

### 5.1.3 Reentrance effect in $dV/dI(V)$

The difference in the interface transmittances of the two samples also causes different behavior for sample A and B in the measurement of the differential resistance as a function of voltage. This can be seen in Fig. 5.1.6, which shows  $dV/dI$  as a function of  $V$  at  $T=30 \text{ mK}$  for the two samples. At low voltages, the curve for sample B clearly shows a reentrance effect which resembles the reentrance effect in the temperature dependent resistance  $R(T)$ . Sample A shows a monotonic decrease in  $dV/dI$  as the voltage is decreased from  $40 \text{ } \mu\text{V}$ . This decrease turns into an increase when a low magnetic field of

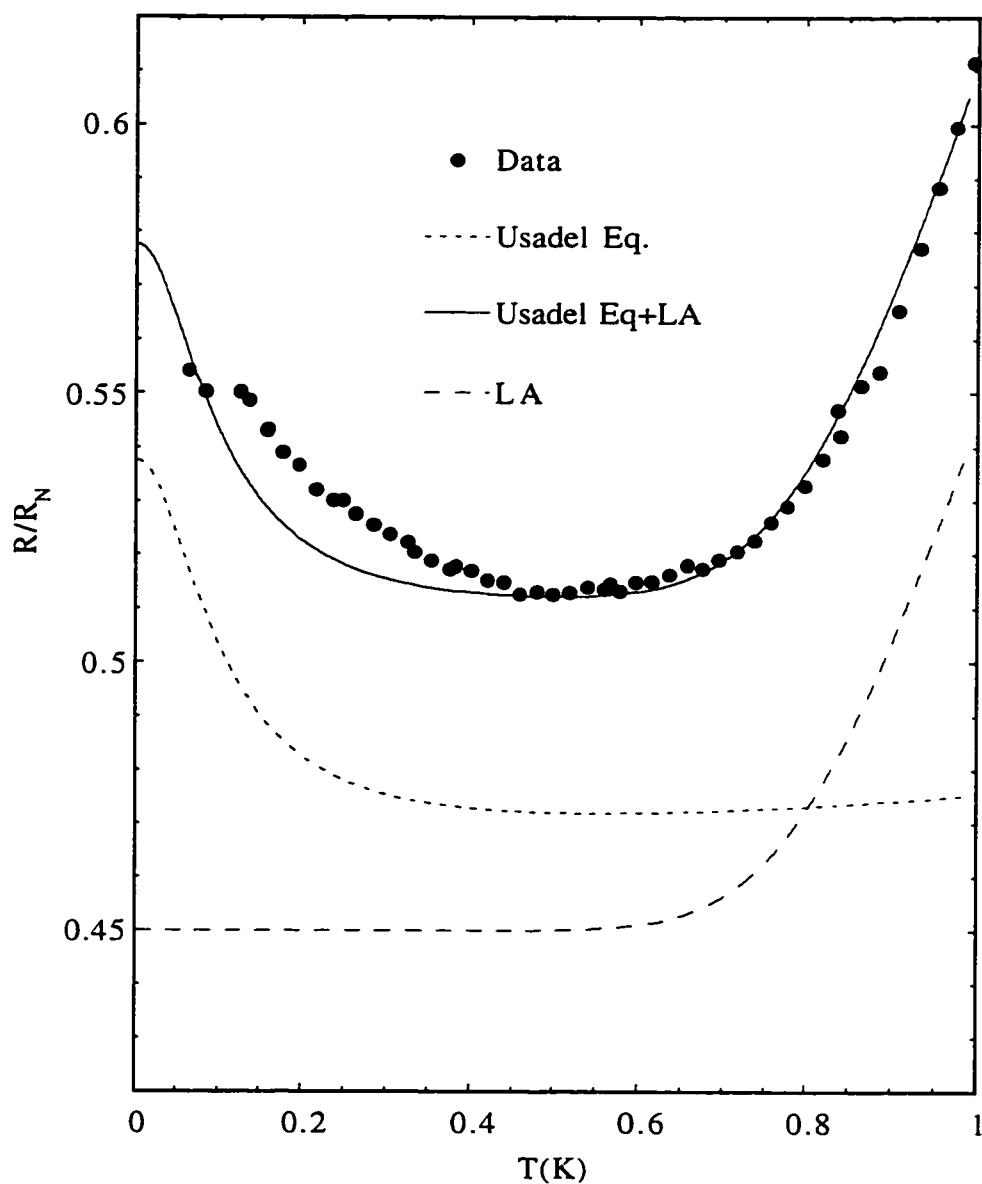


Fig. 5.1.5 Comparison of the experimental data with the theoretical simulation. (a) shows the fit to  $R(T)$  combining the Usadel equation with the formula  $\propto \exp[\beta (1-T/T_c)^{3/2}/T]/T$  based on the LA theory,  $\alpha = 0.1765 \, \Omega K$ ,  $\beta = 9.9284 \, K$ ,  $T_c = 1.2 \, K$ . The dotted curve (Usadel Eq.) is shifted down by 0.04 and the dashed curve (LA) is shifted up by 0.45 for clarity.

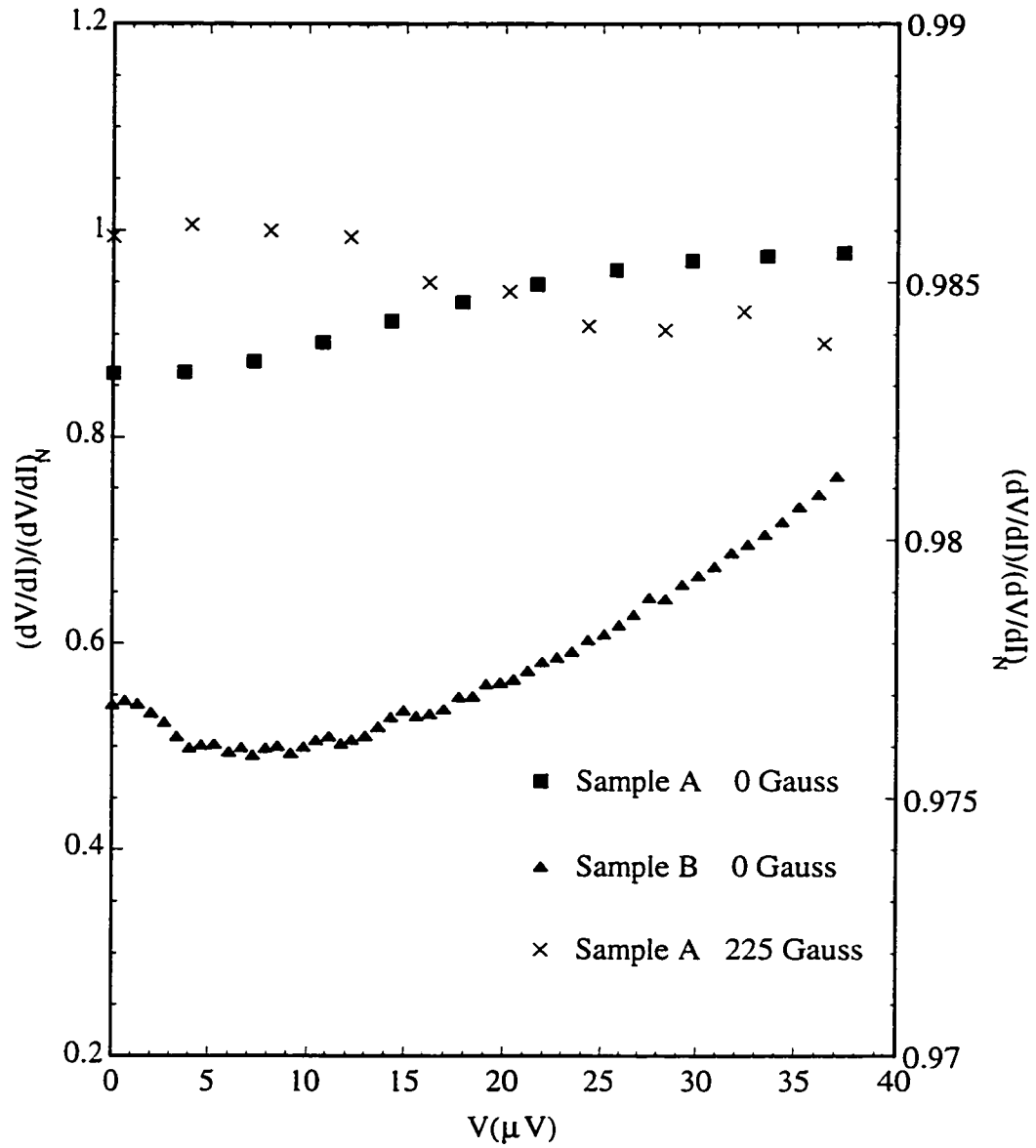


Fig. 5.1.6 Normalized  $dV/dI$  as a function of dc voltage  $V$  at  $T = 30$  mK for sample A and B. The voltage is obtained by integrating  $dV/dI$  vs.  $I_{dc}$ . ac and dc currents are applied through  $I_{\pm}$  shown in Fig. 5.1.1(b).  $(dV/dI)_N$  is  $67.5 \Omega$  and  $10.3 \Omega$  for samples A and B respectively. Also shown is the  $dV/dI$  curve measured at  $H=225$  Gauss for sample A.

225 gauss is applied to the sample. However, this peak is not due to reentrance as can be seen by close examination of  $R(T)$  in a magnetic field. Fig. 5.1.7 shows  $R(T)$  for sample A measured at different values of magnetic field corresponding to different values of the flux threading the hybrid loop. Although there are differences between integral and half-integral values of the flux quanta  $\phi_0 = h/2e$ , the data clearly show no reentrance effect whatsoever. We believe that the peak in  $dV/dI$  at zero bias is similar to the zero bias anomaly observed by Kastalsky *et al.* [72], which was explained by van Wees *et al.* [108] as arising from suppression of coherent multiple Andreev reflections by a magnetic field.

We now focus on the reentrance effect observed in sample B. The minimum resistance occurs at  $\sim 7.25 \mu\text{V}$ . Using the same estimate of the Thouless energy  $E_c$  used in evaluating the minimum in  $R(T)$ ,  $T_{\min}$ , we obtain  $V_{\min} \sim E_c/e = 15 \mu\text{V}$ , where  $V_{\min}$  denotes the voltage at which the minimal differential resistance occurs. This is in disagreement with the result shown in the case of  $R(T)$ , where the calculated  $T_{\min}$  is lower than the observed value by a factor of 3. We shall come back to this problem after we obtain the simulation of  $dV/dI(V)$  based on the theory of quasiclassical Green functions.

To calculate  $dV/dI(V)$ , one notes the temperature kernel in the integrand of Eq. 5.1.9 becomes a step function at  $T = 0$  with the discontinuity centered at  $\varepsilon = eV$ , i.e., the contribution to the total current  $I$  comes only from  $|\varepsilon| < eV$  [48]. The conductance  $dI/dV$  thus contains a  $\delta$ -function centered at  $|\varepsilon| = eV$ . This results in a simple formula at  $T=0$  similar to that given in Ref.[48].

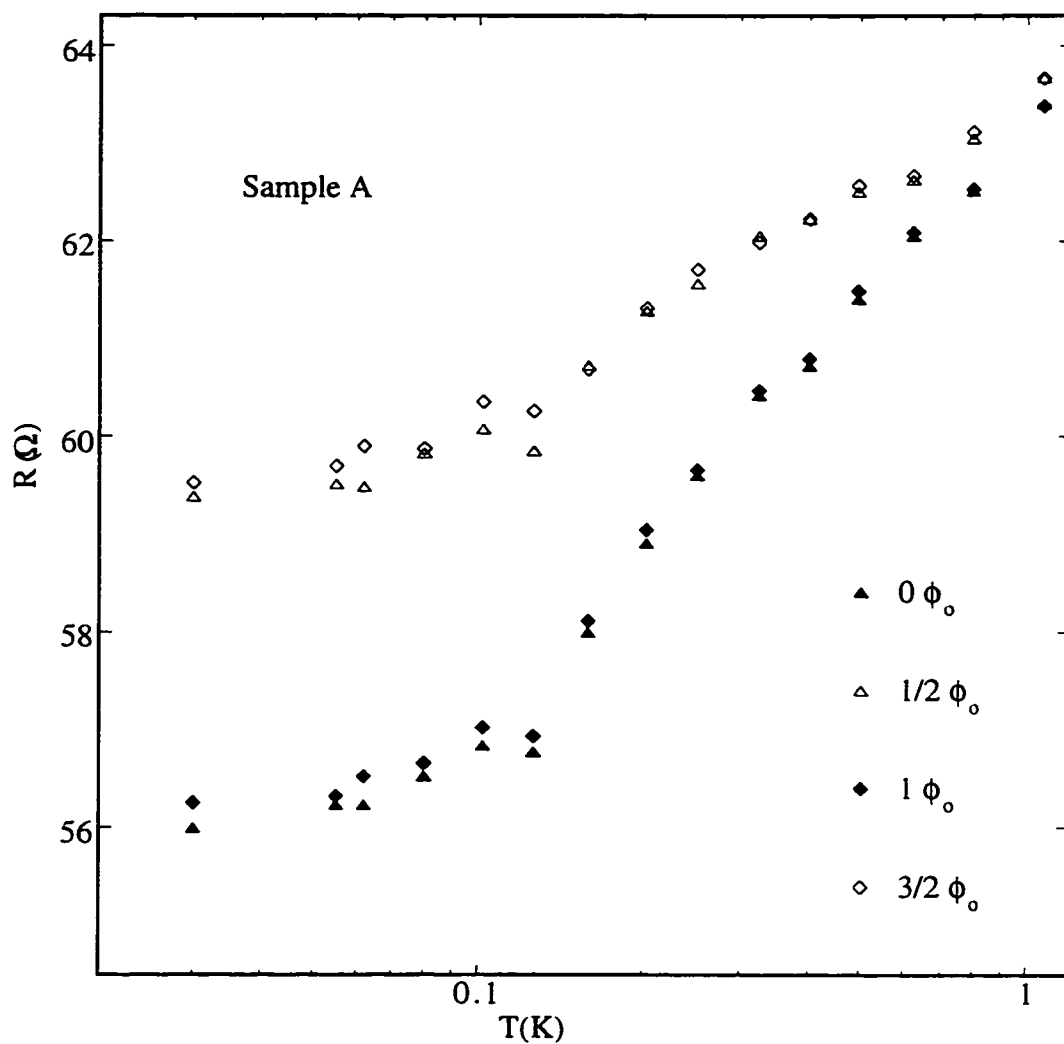


Fig. 5.1.7 Resistance of Sample A as a function of temperature with a magnetic field applied perpendicular to the loop corresponding to different multiples of the flux quantum  $h/2e$  through the loop.



$$R(V) = R_N \left\{ \frac{1}{L} \int_0^L \text{sech}^2 [\text{Im}\theta(\epsilon, x)] dx \right\}_{\epsilon = eV} \quad (5.1.11)$$

However, the calculations of  $R_1(V)$  and  $R_2(V)$  cannot be separated since  $V$  is the sum of  $V_1$  and  $V_2$  measured for each branch subject to the same current  $I$ . The procedure we adopt is as follows.  $R_1(V_1)$  and  $R_2(V_2)$  are calculated first based on Eq. 5.1.11, where  $V_1$  and  $V_2$  are the bias for the long and short branches respectively.  $R_1(V)$  and  $R_2(V)$  are then calculated self-consistently using the following equations.

$$V_1 + V_2 = V \quad (5.1.12a)$$

$$\frac{V_1}{R_1(V_1)} = \frac{V_2}{R_2(V_2)} \quad (5.1.12b)$$

Fig. 5.1.8 shows the experimental data and the calculated curve based on quasiclassical Green functions theory. The theoretical calculation gives a  $V_{\min}$  at  $\sim 20 \mu\text{V}$ . This is partly due to the effect coming from the short N branch similar to the case of  $R(T)$ . Within this voltage range the resistance of the short branch decreases monotonically from  $V=0$  and never reaches its  $V_{\min}$ . Therefore its contribution *flattens* the curvature of the curve obtained from the long branch. Quite clearly, the experiment and the theory do not agree with each other. Using the same arguments as for  $R(T)$ , one may think of adding the contribution due to current induced phase-slip centers. However, this contribution depends exponentially on the dc current, and gives a resistance much larger than the observed differential resistance if we use the same parameters as were used for  $R(T)$ .

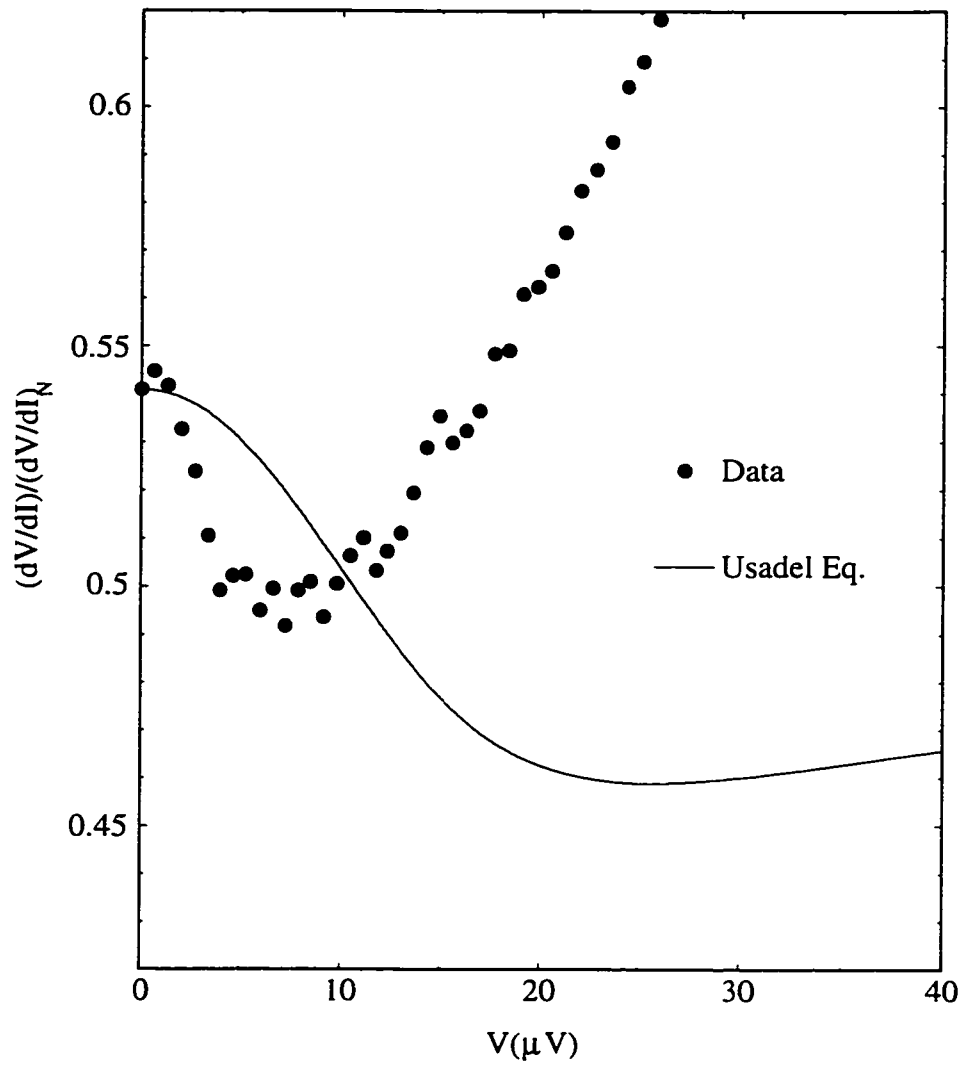


Fig. 5.1.8 Comparison of the theoretical calculation (solid curve) based on the Usadel Eq. with  $dV/dI(V)$ .

#### 5.1.4 Reentrance effect in $R(H)$

We finally present the data for the magnetoresistance measured at various temperatures for both samples. Figure 5.1.9(a) shows the magnetoresistance of sample A at a few temperatures below 1 K. Oscillations of a period corresponding to a flux  $h/2e$  through the loop are observed which persist up to the critical temperature  $T_c$  of the superconductor, and whose amplitude at the lowest temperatures is much larger than  $e^2/h$  (in terms of conductance). Two properties coming from proximity effect are addressed here. First, the large amplitude of these oscillations ( $\gg e^2/h$ ) rules out the possibility of their being due to a normal metal quantum interference effect such as weak localization or conductance fluctuations. Second, the oscillations still have significant amplitudes at temperatures close to  $T_c$ , and disappear at temperatures above  $T_c$ .

Figure 5.1.9(c) shows the amplitude of the magnetoresistance oscillations for the two samples as a function of temperature. The amplitude is determined by calculating the power in the Fourier transform in the inverse field range corresponding to the area of the loop,  $\pm 25$  mT for sample A and  $\pm 20$  mT for sample B. While the oscillation amplitude in sample A shows a monotonic increase as the temperature is decreased, the amplitude of the oscillations for sample B displays a reentrant behavior with a maximum at a temperature of  $\sim 200$  mK. Since the oscillations arise from interference effects around the loop, one might expect that the amplitude of the oscillations would be determined by the ratio of normal metal coherence length  $\xi_N(T)$  to half the length  $L$  of the normal arm, which is  $\sim 1.1$   $\mu\text{m}$ . At  $T \sim 170$  mK,  $2\xi_N(T) = L$ . This is in good agreement with the temperature at which we observe the amplitude maximum. For sample A, no such maximum is observed, even

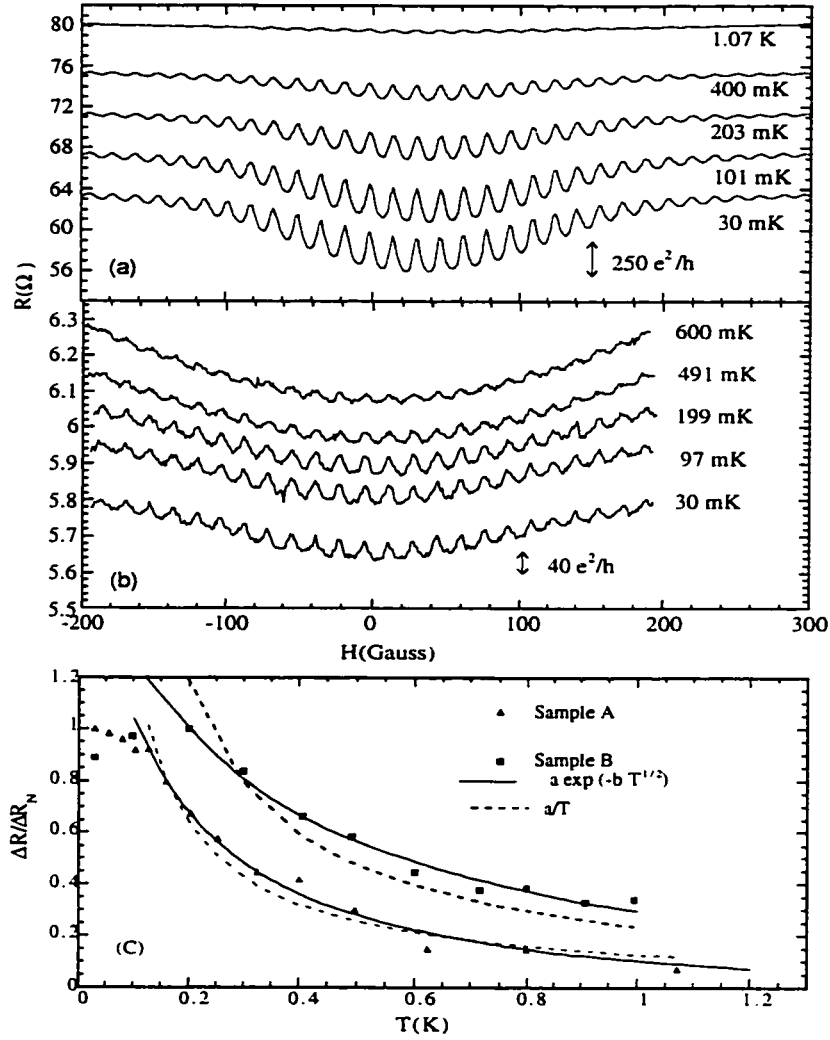


Fig. 5.1.9 (a), (b) are the magnetoresistance curves  $R(H)$  for sample A and B respectively. The small offset of  $H$  in (a) is due to the residual flux trapped in the magnet. In (a) the curves for  $T = 101$  mK, 203 mK, 400 mK and 1.07 K are shifted up by 4  $\Omega$ , 8  $\Omega$ , 12  $\Omega$ , and 16  $\Omega$  respectively. In (b) the curves for  $T = 7$  mK, 199 mK, 491 mK and 600 mK are shifted up by 0.2  $\Omega$ , 0.4  $\Omega$ , 0.7  $\Omega$  and 0.8  $\Omega$  respectively. (c) Normalized amplitude of the Fourier transform of (a) and (b) as a function of temperature. The field range is  $\pm 25$  mT and  $\pm 20$  mT and the normalization amplitude is 0.982  $\Omega$  and 0.019  $\Omega$  for samples A and B respectively. The solid lines represent fits to the form  $a \exp(-b T^{1/2})$  at higher temperatures, with  $a = 3.1, 2.7$  and  $b = 3.4 \text{ K}^{-1/2}, 2.2 \text{ K}^{-1/2}$  for samples A and B respectively. For comparison, we also show a best fit to a power law of the form  $a/T$  as used by Courtois *et al.* [12], with the values  $a = 0.128 \text{ K}, 0.238 \text{ K}$  for samples A and B respectively.

though the film parameters for the two samples are similar. This again is a consequence of the low NS interface transparencies in this sample. At higher temperatures, both samples show a temperature dependence which is well described by a function of the form  $a \exp[-b T^{1/2}]$ , as can be seen in Fig. 5.1.9(c). This is in contrast to the results of Courtois *et al.* [12], where the magnetoresistance oscillations were seen to decay as a power law in temperature. For comparison, we also show the power law dependence found in Ref. 12, which does not describe the data well. This difference may arise from the difference in the specific geometry of the samples in the two experiments.

The oscillations of the magnetoresistance in our samples are obviously related to the presence of the hybrid loop. In a simple picture, the hybrid loop provides periodic oscillating boundary conditions for the correlations induced in both N side branches when a magnetic field is applied. The boundary conditions, of course, are governed by the normal arm of the hybrid loop since one would never expect any oscillation in a structure similar to a NSN geometry if the hybrid loop is broken by disconnecting its normal arm. Therefore, the properties of these magnetoresistance oscillations are not only due to the interface resistances but also the length  $L$  of the normal arm in the loop. Due the complexity of the geometry, we have not attempted to solve the quasiclassical Green functions equations in the presence of a magnetic field. However, a qualitative understanding can be made by comparing with other quantum mechanical interference phenomena such as weak localization [109] in a pure normal-metal loop structure, where the amplitude of the magnetoresistance oscillations decays exponentially over the phase breaking length  $L_\phi$ ,  $\Delta R/R_N \sim \exp(-L/L_\phi)$ ,  $L$  being the perimeter of the loop. In the normal arm of our hybrid

loop, the oscillating amplitude is determined by the normal metal coherence length  $\xi_N$ . Consequently, one expects the oscillating amplitudes outside the loop are also determined by  $\xi_N$ . This is indeed what we observed in Fig. 5.1.9(c). The reentrance observed in magnetoresistance oscillations in sample B is an indication that these oscillations are dependent on the proximity effect in the normal arm of the hybrid loop.

## 5.2 Conclusion

In conclusion, we have investigated the reentrance effect in two mesoscopic NS hybrid loops with different interface transmittances. This reentrance effect was due to the long range coherence of the electron-hole pairs Andreev reflected from the NS interfaces in the sample. The effect of the transmittance on the reentrant behavior was qualitatively demonstrated by these two samples. The sample with high interface transmittances showed the reentrance effect in  $R(T)$ ,  $dV/dI(V)$  and amplitude of magnetoresistance oscillations. The reentrance effect was not observed in the sample with low interface transmittances. The observed reentrance effect is qualitatively well explained by the theory of quasiclassical Green functions. However, based on our theoretical simulation of the measurements, there exists a quantitative discrepancy between the theory and the experimental results. The discrepancies include: (i) At low temperatures or voltages, the locations of the temperature  $T_{\min}$  or voltage  $V_{\min}$  where the minimal resistance, differential resistance, or amplitude of magnetoresistance oscillations occur do not agree with the theoretical predictions. (ii) At high temperatures or voltages close to  $T_c$  or  $\Delta$ , the theoretical prediction shows a much

slower recovery of the normal metal resistance than the experimental results at high temperatures or bias voltages.

These two discrepancies have been seen in other experiments as well. In the experiments by Courtois *et al.* [13],  $T_{\min}$  and  $V_{\min}$  are measured on a short N wire with a S stripe in the middle. Both  $T_{\min}$  and  $V_{\min}$  are not located at the theoretical prediction of  $5E_c$ . In the experiments on 2DEG connected to a superconductors [15-17], the reentrance effect on the amplitude of magnetoresistance oscillations is not easy to compare with the theoretical prediction due to the difficulty in identifying the geometry of the sample. Nonetheless, rough estimates of  $T_{\min}$  and  $V_{\min}$  in these 2DEG systems, although are about the order of  $5E_c$ , also show some discrepancies. At higher temperatures, experimental results from both systems show the same behavior as our observation, i.e., the normal state resistance is recovered much more slowly than the theory predicts.

These previous disagreements along with our results raise the question about the applicability of the theory to our samples, or, the suitability of the experimental geometry to the theory. We discuss below the possible reasons for this discrepancy.

In our numerical calculation and in all other numerical calculations, the following assumptions are made: (i) The energy gap of the superconductor is much larger than the energies and temperatures involved in the measurement. However, this assumption is not valid for the superconductor (Al) used in our experiment. An improved experiment may be done in a system where the superconductor possesses a larger energy gap such as niobium. (ii) Phase breaking is neglected in our simulation under the assumption that the sample size

is much shorter than  $L_\phi$ . This may cause an intrinsic difference in the measurement of  $R(T)$  and  $dV/dI(V)$ .  $L_\phi$  is temperature dependent in our range of measurement and it is not clear how to take this temperature dependence into account in the theory. (iii) We have assumed perfect NS interfaces in Sample B. The influence of the NS interface transmittance on reentrance effect needs further investigation. (iv) The superconducting reservoir in our system is a mesoscopic 1D wire. It is quite likely that the superconductivity in this wire is suppressed due to its proximity to the normal metal, or by the presence of a transport current. Lastly, there is no quantitative comparison between the theory and the experimental results on the reentrance effect in the amplitude of magnetoresistance oscillations. Due to the complexity of our sample geometry, it is difficult to perform this comparison. We hope to investigate this problem in a system of different geometry in the future.

To illustrate some of the discrepancies, we present a transport measurement on a 1D N-S wire, showing some interesting features regarding the problems discussed above. Fig. 5.2.1 is the resistance measured across a 1D N-S wire, with the geometry and the dimensions shown in the inset. At  $T_c$ , it shows a sharp drop in resistance similar to that observed in  $R(T)$  of Sample B. This sharp drop corresponds to the decrease in resistance of the S part of the wire at the superconducting transition. At  $T \sim 1K$ , the resistance of the N-S wire reaches its minimum and increases at lower temperatures. This behavior is very similar to what we observed in  $R(T)$  of Sample B. However, a rough estimate of the Thouless temperature  $T_{ec}$  ( $k_B T_{ec} = E_c$ ) of the N wire gives a value (10 mK) much lower than 1K, which is a consequence of the long length of the N wire. On the other hand, the resistance saturates at very low temperatures, implying a reentrant behavior. The increase



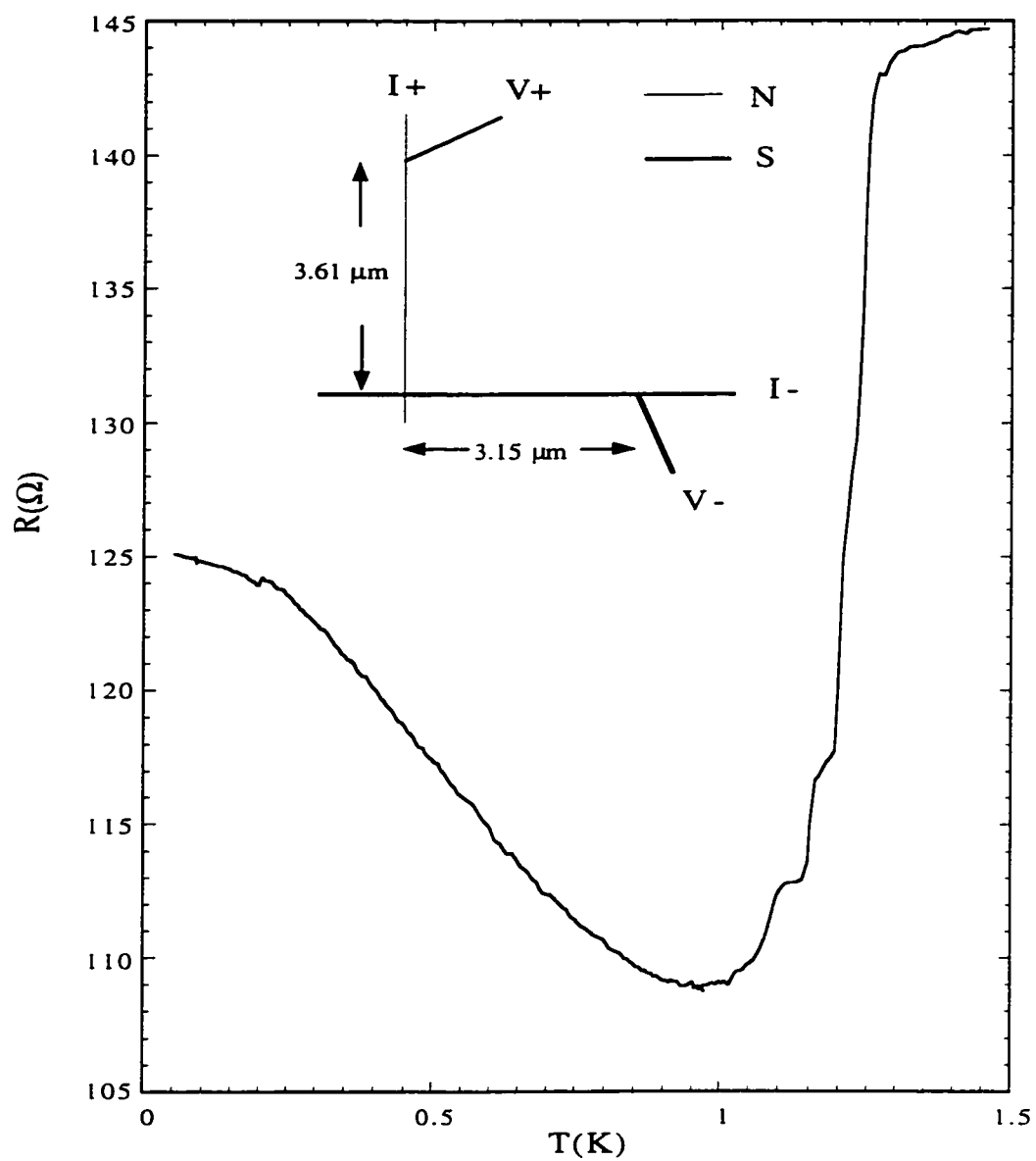


Fig. 5.2.1 Resistance as a function of temperature for a simple 1D normal-metal superconducting wire.

of resistance near  $T_c$  is different from the observation of Petrashov *et al.* [10-11], where the resistance was enhanced to a value above the normal state resistance similar to the resistance anomaly described in Chapter 4.

The large discrepancy between the experiment and the theory in this sample points to the need for further experiments. We have extended the investigation of reentrance effect to a single 1D normal wire connected to a normal reservoir in one end and superconducting reservoir in the other. By varying the length of the normal wire, we hope to acquire more understanding of the reentrance effect.

## Chapter 6

### Conclusions

We have studied charge imbalance and the proximity effect through charge transport in mesoscopic samples containing pure superconductors or normal-metal/superconducting interfaces at temperatures below the critical temperature of the superconductor involved. In the experiments related to charge imbalance, the previously observed resistance anomaly in 1D pure superconductors was investigated by applying rf radiation, magnetic field, and noise signals to the pure superconductor. Through detailed analysis and comparison between different measurements, we have found again that phase-slip centers in these pure superconductors play an important role in explaining the observed resistance anomaly. A further investigation of this resistance anomaly is extended to 1D NS systems. In these 1D NS systems, there already exist nonequilibrium regions about the NS interfaces. Therefore, one does not need to apply any external factors to observe the resistance anomaly mentioned above. However, some of our results suggest there may exist additional phase-slip centers in the samples. Furthermore, we observed some interesting results related to the resistance anomaly when small magnetic fields are applied to these NS samples. These results may be related to the coherent nature of quasiparticles in the non-equilibrium superconductors.

In experiments related to the proximity effect, the reentrant behavior of the normal metal resistance was observed in the diffusive regime through three transport measurements, i.e.,  $R(T)$ ,  $dV/dI(V)$  and  $R(H)$  at different temperatures. While this reentrance effect can be qualitatively explained by the theory of quasiclassical Green

functions, the comparison of our theoretical calculation with the experimental results shows discrepancies. We have discussed some possible reasons for these discrepancies and suggested the direction of further investigation.

The conclusion and further development of our current understanding of charge imbalance and proximity effect are summarized in the following sections.

## 6.1 Resistance anomaly

### *Pure superconductors*

In our study of the resistance anomaly in 1D superconducting wires or loops, we found that the resistance anomaly could be induced by radio-frequency (rf) radiation, magnetic field, or noise current. However, the origins of these resistance anomalies are different. The rf and magnetic field induced resistance anomalies are a result of charge imbalance in the sample. This charge imbalance is due to the formation of a PSC in the sample when the rf signal or magnetic field is applied. While the magnetic field induced PSC is clearly due to the suppression of the order parameter in the sample, the microscopic mechanism responsible for the rf induced PSC is still not clear. The noise induced resistance anomaly, on the other hand, is due to the mixing of different frequency ac signals existing in the measurement. The manifestation of the noise induced resistive anomaly is similar to that produced by a rf signal or magnetic fields except that one does not observe negative differential resistance in the noise induced anomaly. Therefore, in and of itself, it does not provide a complete explanation for the resistance anomaly observed in the pure mesoscopic superconducting wires.

### *Normal-metal/superconducting wires and loops*

Resistance anomalies observed in the 1D normal-metal (N)/superconducting (S) systems show several properties in addition to those observed in pure superconductors. These properties are : (i) The amplitude of the resistance anomaly shows a nonmonotonic behavior as a function of magnetic field in the N-S wire. The magnetic field dependence of the charge imbalance length may explain this nonmonotonic behavior. (ii) Magnetic field dependent negative differential resistance dips are observed in the N-S loop structures. Based on the charge imbalance model, this implies that the pair chemical potential in the charge imbalance region is sensitive to the phase of the superconductor. If one can modulate the phase, it may be possible to detect this property through existing measurements of charge imbalance, i.e., resistance anomaly or excess voltage. (iii) The negative differential resistances observed in the N-S loops shows a two-level switching behavior, whose switching rate increases as a function of temperature, suggesting the presence of an energy barrier. This behavior may be the threshold energy required for nucleating a PSC in the system.

## **6.2 Reentrance effect**

We have observed the proximity regime reentrance effect in three transport measurements,  $R(T)$ ,  $dV/dI(V)$  and the temperature dependence of the magnetoresistance oscillation amplitude in a single N-S hybrid loop. This effect is due to an anomalous proximity effect in the normal metal of our devices and is qualitatively well explained by the theory of quasiclassical Green functions. However, a detailed quantitative comparison of the theoretical calculation with the experimental results shows several discrepancies. For better

agreement between theory and experiment, we believe it is necessary to extend the range of the theory and calculations to take into account effects such as a finite temperature-dependent phase coherence length, the temperature dependence of the gap in the superconductor, and suppression of superconductivity in the superconducting elements.

### 6.3 Future work

Excluding possible measuring defects stemming from signal mixing, present investigations on the resistance anomalies observed in mesoscopic pure superconductors point to one explanation: a PSC induced charge imbalance. However, the current understanding of the properties of PSC in such systems still leaves much to be discussed. In the mesoscopic systems containing NS interfaces, we observed negative differential resistances similar to the observations by Park *et al.* In a WS system [5]. These negative differential resistances were further shown to be metastable and phase sensitive. If the negative differential resistances are due to PSCs in the sample, this 1D NS system may provide another way of studying the properties and origin of PSCs and help us acquire more knowledge in the superconductor through its nonequilibrium properties.

In the study of proximity effect, our investigation on the reentrance effect in a diffusive NS loop motivates further study in the following direction. To provide a concrete test of the theory, the system studied should be simplified to a 1D normal wire connected to a superconducting reservoir on one end and a normal reservoir on the other. In terms of theory, effects present in real samples, such as inelastic scattering and electron-electron interaction need to be incorporated in the simulation using quasiclassical Green functions.

The influence of boundary conditions on the quasiclassical Green functions induced in the normal metal can be studied through the roles of the normal reservoir, the superconducting reservoir, the NS interface, and the phase gradient induced by external factors such as magnetic field and supercurrent.

At the moment, there is no theoretical bridge between the low temperature, low energy regime of the proximity effect description and the higher temperature, higher energy regime of the theory of non-equilibrium superconductivity. In the proximity effect regime, phase coherence plays an important role, but the effect of spatially varying potentials has not been investigated thoroughly. In the non-equilibrium regime, phase coherence of the carriers is usually ignored, but the spatial variation of the pair and quasiparticle potential is critical. Our experiments show that both factors are important in both regimes, and a theory which smoothly connects both regimes is needed.

## References

- [1] P. Santhanam, C. C. Chi, S. J. Wind, M. J. Brady, and J. J. Bucchignano, *Phys. Rev. Lett.* **66**, 2254 (1991).
- [2] Y. K. Kwong, K. Lin, P. J. Hakonen, M. S. Isaacson, and J. M. Parpia, *Phys. Rev.* **B44**, 462 (1991).
- [3] H. Vloeberghs, V. V. Moshchalkov, C. V. Haesendonck, R. Jonckheere, and Y. Bruynseraede, *Phys. Rev. Lett.* **69**, 1268 (1992).
- [4] J.-J. Kim, et al., *J. Phys. Condens. Matter* **6**, 7055 (1994).
- [5] M. Park, M. S. Isaacson, and J. M. Parpia, *Phys. Rev. Lett.* **75**, 3740 (1995); *Phys. Rev.* **B55**, 9067 (1997).
- [6] C. Strunk, V. Bruyndoncx, C. Van Haesendonck, V.V. Moshchalkov, Y. Bruynseraede, B. Burk, C.-J. Chien, and V. Chandrasekhar, *Phys. Rev. B* **53**, 11332 (1996).
- [7] B. Burk, C.-J. Chien, and V. Chandrasekhar, C. Strunk, V. Bruyndoncx, C. Van Haesendonck, V.V. Moshchalkov, and Y. Bruynseraede, *Superlattices Microstruct.* **20**, 575 (1996).
- [8] B. Burk, C.-J. Chien, V. Chandrasekhar, C. Strunk, V. Bruyndoncx, C. Van Haesendonck, V. V. Moshchalkov and Y. Bruynseraede, *J. Appl. Phys.* **83**(3), 1549 (1998).
- [9] C. Strunk, V. Bruyndoncx, C. Van Haesendonck, V. V. Moshchalkov, Y. Bruynseraede, B. Burk, C.-J. Chien and V. Chandrasekhar, *Phys. Rev.* **B57**, 10854 (1998).
- [10] V. T. Petrashov and V. N. Antonov, *JETP Lett.* **54**, 241 (1991).
- [11] V. T. Petrashov, V. N. Antonov and S. V. Maksimov, *JETP Lett.* **58**, 49 (1993).
- [12] H. Courtois, Ph. Gandit, D. Mailly, and G. Pannetier, *Phys. Rev. Lett.* **76**, 130 (1996).
- [13] P. Charlat, H. Courtois, Ph. Gandit, D. Mailly, A. F. Volkov, and B. Pannetier, *Phys. Rev. Lett.* **77**, 4950 (1996); *Czech J. Physics*, **V 46**, 3107 (1996).
- [14] Petrashov, R. Sh. Shaikhaidarov, and I. A. Sosnin. XXXIst Rencontres de Moriond, Condensed Matter Physics Meeting "Correlated Fermions & Transport in Mesoscopic Systems", Les Arcs, Savoie, France, January 20-27 (1996).
- [15] S. G. Den Hartog, C. M. A Kapteyn, B. J. Van Wees, T. M. Klapwijk and G. Borghs, *Phys. Rev. Lett.* **77**, 4954 (1996).



- [16] S. G. den Hartog, B. J. Van Wees, Y. V. Nazarov, T. M. Klapwijk, and G. Borghs, preprint (1997).
- [17] E. Toyoda and H. Takayanagi, The 12th International Conference on the Electronic Properties of Two-Dimensional Systems, EP2DS-12 (Tokyo September 1997).
- [18] M. Tinkham, *Introduction to Superconductivity*, 2nd edition. (McGraw-Hill, New York, 1996).
- [19] J. Clarke in *Nonequilibrium Superconductivity*, edited by D. N. Langenberg and A. I. Larkin, ( North-Holland, Amsterdam, 1986 ).
- [20] R. Tidecks, *Current-Induced Nonequilibrium Phenomena in Quasi-One-Dimensional Superconductors*, (Springer-Verlag, 1990).
- [21] A. B. Pippard, J. G. Shepherd and D. A. Tindall, Proc. Roy. Soc. (London) **A324**, 17 (1971).
- [22] J. Clarke, Phys. Rev. Lett. **28**, 1363 (1972).
- [23] M. Tinkham and J. Clarke, Phys. Rev. Lett. **28**, 1366 (1972).
- [24] M. Tinkham, Phys. Rev. **B6**, 1747 (1972).
- [25] A. Schmid and G. Schön, J. Low Temp. Phys. **20**, 207 (1975).
- [26] C. J. Pethick and H. Smith, Ann. Phys. **119**, 133 (1979).
- [27] G. J. Dolan and L. D. Jackel, Phys. Rev. Lett. **39**, 1628 (1977).
- [28] W. A. Little and R. D. Parks, Phys. Rev. Lett. **9**, 9 (1962).
- [29] R. Holm and W. Meissner, Z. Phys. **74**, 715 (1932).
- [30] H. Meissner, Phys. Rev. **117**, 672 (1960).
- [31] P. H. Smith, S. Shapiro, J. L. Miles, J. Nicole, Phys. Rev. Lett. **6**, 686 (1961).
- [32] J. Clarke, Proc. Roy. Soc. **A308**, 447 (1969).
- [33] G. Deutscher and P. G. De Gennes, in *Superconductivity* edited by R. D. Parks ( Marcel Dekker, New York, 1969 ).
- [34] E. L. Wolf, *Principles of Electron Tunneling Spectroscopy*, (Oxford University Press, New York, 1985).
- [35] P. G. De Gennes, *Superconductivity of Metals and Alloys*, (Addison-Wesley Co., Inc. 1989).

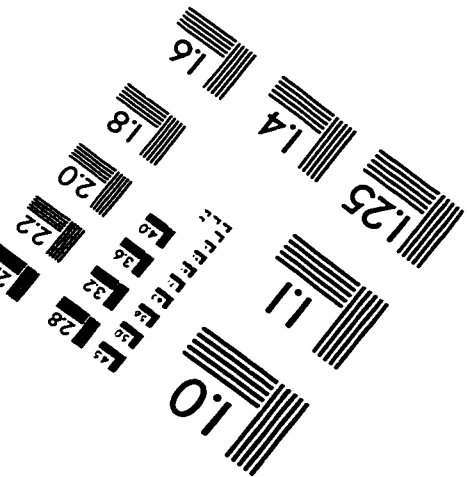
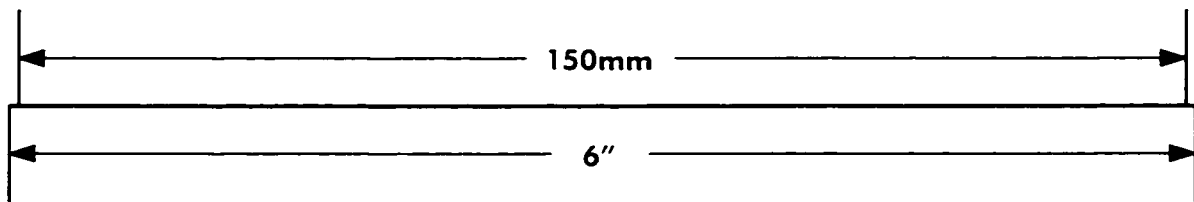
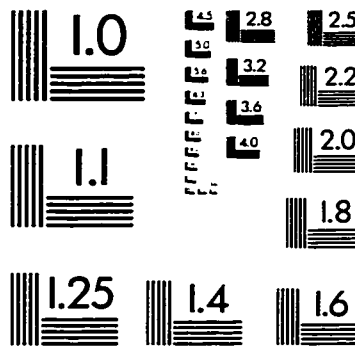
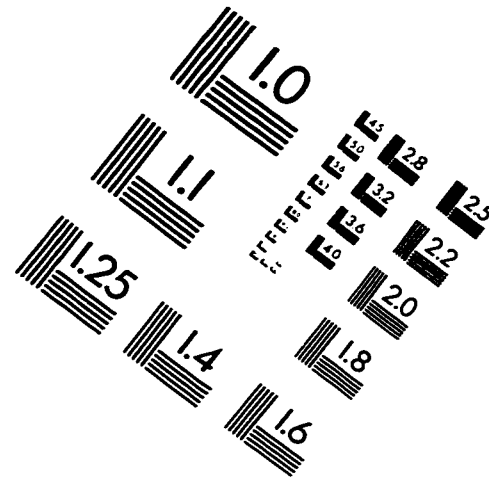
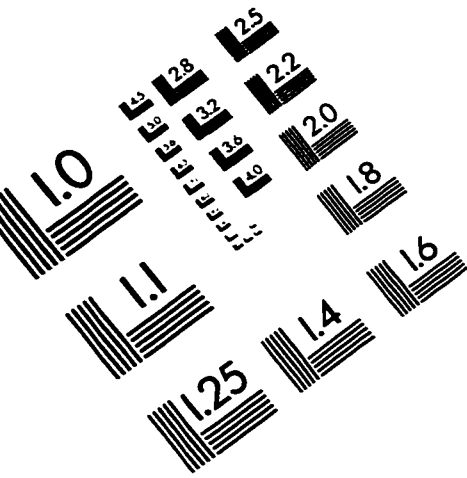
- [36] A. F. Andreev, Sov. Phys. JETP **19**, 1228 (1964).
- [37] N. N. Bogoliubov, Nuovo Cimento **7**, 794 (1958); Zh. Eksperim. Teor. Fiz. **34**, 58 (1958) [Soviet Phys. - JETP **7**, 41 (1958)].
- [38] P. G. de Gennes and D. Saint-James, Phys. Lett. **4**, 151 (1963).
- [39] For a review, see Proc. Of the NATO Adv. Res. Workshop on Mesoscopic Superconductivity, Physica **203B**, 201 (1993).
- [40] H. Courtois, Ph. Gandit, and G. Pannetier, Phys. Rev. **B51**, 9360 (1995); **B52**, 1162 (1995).
- [41] V. T. Petrashov, V. N. Antonov, P. Delsing, and T. Claeson, Phys. Rev. Lett. **70**, 347 (1993).
- [42] P. G. N. De Vegvar, T. A. Fulton, W. H. Mallison, and R. E. Miller, Phys. Rev. Lett. **73**, 1416 (1994).
- [43] H. Pothier, S. Gueron, D. Esteve, and M. H. Devoret, Phys. Rev. Lett. **73**, 2488 (1994).
- [44] V. T. Petrashov, V. N. Antonov, P. Delsing, and T. Claeson, Phys. Rev. Lett. **74**, 5268 (1995).
- [45] See, for example, S. Washburn and R.A. Webb, Adv. Phys. **35**, 375 (1986).
- [46] S. N. Artemenko, A. F. Volkov, and A. V. Zaitsev, Solid State Comm. **30**, 771 (1979).
- [47] Y. V. Nazarov, Phys. Rev. Lett. **73**, 1420 (1994).
- [48] S. Yip, Phys. Rev. B **52**, 15504 (1995).
- [49] F. Zhou, B. Spivak, and A. Zyuzin, Phys. Rev. **B52**, 4467 (1995).
- [50] Y. V. Nazarov and T. H. Stoof, Phys. Rev. Lett. **76**, 823 (1996); T. H. Stoof and Yu. V. Nazarov, Phys. Rev. **B53**, 14496 (1996).
- [51] A. F. Volkov, N. Allsopp, C. J. Lambert, J. Phys.:Cond. Matt. **8**, L45 (1996).
- [52] A. A. Golubov, F. K. Wilhelm, and A. D. Zaikin, Phys. Rev. B **55**, 1123 (1997).
- [53] S. Guéron, Ph.D. Thesis. (1997).
- [54] K. D. Usadel, Phys. Rev. Lett. **25**, 507 (1970).
- [55] For review, see V. T. Petrashov, Czech. J. Phys. **46**, Suppl. S6, 3303 (1996).

- [56] V. N. Antonov, A. F. Volkov and Hideaki Takayanagi, *Europhys. Lett.*, **38**(6), 453 (1997).
- [57] V. N. Antonov and Hideaki Takayanagi, *Phys. Rev.* **B56**, Rapid Comm. R8515 (1997).
- [58] J. Bardeen, L. N. Cooper, and J. R. Schrieffer, *Phys. Rev.* **108**, 1175 (1957).
- [59] L. N. Cooper, *Phys. Rev.* **104**, 1189 (1956).
- [60] H. Fröhlich, *Proc. Roy. Soc. (London)* **A215**, 291 (1952).
- [61] J. Bardeen and D. Pines, *Phys. Rev.* **99**, 1140 (1955).
- [62] D. Pines, *Phys. Rev.* **109**, 280 (1958).
- [63] J. B. Ketterson and S. N. Song, *Superconductivity*, (Cambridge Press, 1998).
- [64] M. Tinkham, 1979, *Festkörperprobleme (Advanced in Solid State Physics)*, Vol. 19, ed. J. Treusch (Vieweg Braunschweig) p. 363.
- [65] T. J. Rieger, D. J. Scalapino, and J. E. Mercereau, *Phys. Rev.* **B6**, 1734 (1972).
- [66] W. J. Skocpol, M. R. Beasley, and M. Tinkham, *J. Low. Temp. Phys.* **16**, 145 (1974).
- [67] A. M. Kadin, L. N. Smith, and W. J. Skocpol, *J. Low. Temp. Phys.* **38**, 497 (1980).
- [68] J. S. Langer and V. Ambegaokar, *Phys. Rev.* **164**, 498 (1967).
- [69] D. E. McCumber and B. I. Halperin, *Phys. Rev.* **B1**, 1054 (1970).
- [70] M. L. Yu and J. E. Mercereau, *Phys. Rev. Lett.* **28**, 1117 (1972).
- [71] G. E. Blonder, M. Tinkham, and T. M. Klapwijk, *Phys. Rev.* **B25**, 4515 (1982).
- [72] A. Kastalsky, A. W. Kleinsasser, L. H. Greene, R. Bhat, F. P. Milliken and J. P. Harbison, *Phys. Rev. Lett.* **67**, 3026 (1991).
- [73] C. J. Lambert, *J. Phys. Cond. Matter* **3**, 6579 (1991).
- [74] Y. Takane and H. Ebisawa, *J. Phys. Soc. Jpn.* **61**, 2858 (1992); *J. Phys. Soc. Jpn.* **62**, 1844 (1993).
- [75] I. K. Marmorkos, C. W. J. Beenakker and R. A. Jalabert, *Phys. Rev.* **B48**, 2811 (1993).
- [76] A. V. Zaitsev, *JETP Lett.* **51**, 41 (1990).

- [77] A. F. Volkov, JETP Lett. **55**, 747 (1992).
- [78] A. F. Volkov and T. M. Klapwijk, Phys. Lett. **A168**, 217 (1992).
- [79] A. F. Volkov, A. V. Zaitsev and T. M. Klapwijk, Physica C **210**, 21 (1993) ;
- [80] A. F. Volkov, Physica B **203**, 267 (1994).
- [81] L. V. Keldysh, Sov. Phys. JETP **20**, 1018 (1964).
- [82] A. I. Larkin and Yu. N. Ovchinnikov, Sov. Phys. JETP **41**, 960 (1975); JETP **46**, 155 (1977).
- [83] J. Rammer and H. Smith, Rev. Mod. Phys. **58**, 323 (1986).
- [84] A. I. Larkin and Yu. N. Ovchinnikov, in *Nonequilibrium Superconductivity*, edited by D. N. Langenberg and A. I. Larkin, ( North-Holland, Amsterdam, 1986 ).
- [85] M. Yu. Kuprianov and V. F. Lukichev, Sov. Phys. JETP **67**, 1163 (1988).
- [86] S. Guéron, H. Pothier, Norman O. Birge, D. Esteve, and M. H. Devoret, Phys. Rev. Lett. **77**, 3025 (1996).
- [87] A. Dimoulas, J. P. Heida, B. J. v. Wees, T. M. Klapwijk, W. v. d. Graaf, and G. Borghs, Phys. Rev. Lett. **74**, 602 (1995).
- [88] S. G. den Hartog, C. M. A. Kapteyn, B. J. v. Wees, T. M. Klapwijk, W. v. d. Graaf, and G. Borghs, Phys. Rev. Lett. **76**, 4592 (1996).
- [89] S. Mackie and S. P. Beaumont, Solid State Technol. **28**, No. 8, 117 (1985).
- [90] M. Rooks, Ph.D. Thesis, Yale University (1987).
- [91] M. Rooks, C. C. Eugster, J. A. Del Alamo, G. L. Snider and E. L. Hu, J. Vac. Sci. Technol. B9 (6), 2856 (1991).
- [92] See, for example, *Lithography*, in VLSI Technology edited by S. M. Sze, 2nd edition. (McGraw-Hill, 1988).
- [93] For example, see *Electron-beam process* by J. S. Greeneich in Electron-Beam Technology in Microelectronic Fabrication, edited by R. B. George. (Academic Press, New York, 1980).
- [94] B. Chapman, *Glow Discharge Processes* (John Wiley & Sons, 1980).
- [95] See, for example, *Oxidation* by L. E. Katz in VLSI Technology edited by S. M. Sze, 2nd edition. (McGraw-Hill, 1988).

- [96] H. Z. Massoud et al, J. Electrochem. Soc., **132**, 2685 (1985).
- [97] O. V. Lounasmaa, *Experimental Principles and Methods Below 1 K*. (Academic, London 1974).
- [98] G. K. White, *Experimental Techniques in Low Temperature Physics*, 3rd edition. (Clarendon, Oxford 1979).
- [99] R. C. Richardson and E. N. Smith, *Experimental Techniques in Condensed Matter Physics at Low Temperatures*. (Addison-Wesley, Redwood City, CA 1988).
- [100] F. Pobell, *Matter and Methods at Low Temperatures*, 2nd edition. (Springer-Verlag, New York, 1992).
- [101] V. Chandrasekhar, Ph.D. Thesis, Yale University (1989).
- [102] J. G. Adler and J. E. Jackson, Rev. Sci. Instrum. **37**, 1049 (1966).
- [103] W. A. Little and R. D. Parks, Phys. Rev. Lett. **9**, 9 (1962).
- [104] J. Romijn, T. M. Klapwijk, M. J. Renne, and J. E. Mooij, Phys. Rev. B **26**, 3648 (1982).
- [105] R. P. Groff and R. D. Parks, Phys. Rev. **176**, 567 (1968).
- [106] N. E. Israeloff, F. Yu, A. M. Goldman and R. Bojko, Physica **B203**, 454 (1994).
- [107] We believe  $L_\phi$  for the Ag wire is very short due to the bake required for the second layer of the lithography.
- [108] B. J. van Wees, P. de Vries, P. Magnee and T. M. Klapwijk, Phys. Rev. Lett. **69**, 510 (1992).
- [109] V. Chandrasekhar, M. J. Rooks, S. Wind, and D. E. Prober, Phys. Rev. Lett. **55**, 1610 (1985).
- [110] J. Eom, Ph.D. Thesis, Northwestern University (1998).

# IMAGE EVALUATION TEST TARGET (QA-3)



APPLIED IMAGE, Inc  
1653 East Main Street  
Rochester, NY 14609 USA  
Phone: 716/482-0300  
Fax: 716/288-5989

© 1993, Applied Image, Inc., All Rights Reserved

